Chemical Modification of graphene

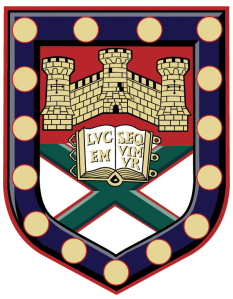

Freddie Withers

School of Physics

University of Exeter

A thesis submitted for the degree of

Doctor of Philosophy

September 2012

Chemical Modification of graphene.

Submitted by Freddie Withers to the University of Exeter as a thesis for the degree of Doctor of Philosophy in Physics
2012

I certify that all material in this thesis which is not my own work has been identified and that no material has previously been submitted and approved for the award of a degree by this or any other University.

Freddie Withers
2012

Acknowledgements

I would like to acknowledge the late Prof. Alexander Savchenko for attracting me to the world of condensed matter physics. He got my respect instantly the first time I noticed that he was hands on and working in the lab, seeing himself as an equal to others, truly one of the best people I have ever had the pleasure to work with. After Alex's unexpected death Dr Monica Craciun and Dr Saverio Russo took over my supervision and I thank them for all there help and direction they have given me. Thank you to the collaborators who without samples this work would not be possible : Dr Marc Dubois, Dr Chris Howard and Dr. Mark Dean. Thanks to All the fellow Phd students and post docs I have worked and have successfully collaborated with : Dr. Adam Price, Tim Khodkov, Ivan Khrapach, Alexey Kaverzin, Tom Bointon, David Hudson, Dimitry polyushkin. Also to other fellow Phd students who have offered help and support : Pete Hale, Sam Hornett, Alexy Kozikov. A massive thanks to Adam Woodgate, Dave Gregeory for continuous and diligent supply of helium without there work none of the presented data would of been possible. Thanks to Paul Wilkins who had to deal with our constant stream of demands, including feed through, Intercalation tubes, baffles etc etc, Chapter 6 and Chapter 8 would not of happened without his expertise. Also thanks to Prof Bill Barnes for mentoring me over the past 3 years. Thank you to my family, Richard Withers for allowing me work with him during my undergraduate period, I would like to thank Matt Ingram for also supplying me with work over one summer, without this help I would of been forced to quit higher education. Thank you also to Rob Lock for support over the years. Thank you to My friends, Rob Allen, Jack Hollington, Matt Ingram, Matt Donovon, Ryan Thompson and Dom Beverly who supplied me with some much needed escapism over the past few years, these times have been priceless. Finally a Massive thank you to Tanya Cistova for invaluable support over the past year.

Abstract

In this thesis investigations into chemically modified graphene structures are presented. Chemical functionalization of graphene is the chemical attachment of molecules or atoms to the graphene surface via covalent or Van der Waals bonds, this process offers a unique way to tailor the properties of graphene to make it useful for a wide range of device applications. One type of chemical functionalization presented in this thesis is fluorination of graphene which is the covalent attachment of fluorine to the carbon atoms of graphene and the resultant material is fluorographene which is a wide band-gap semiconductor. For low fluorine coverage the low temperature electron transport is through localized states due to the presence of disorder induced sub-gap states. For high fluorine coverage the electron transport can be explained by a lightly doped semiconductor model where transport is through thermal activation across an energy gap between an impurity and conduction bands. On the other hand, at low temperatures the disorder induced sub-gap density of states dominates the electrical properties, and the conduction takes place via hopping through these localized states. In this thesis it is also shown that electron beam irradiation can be used to tune the coverage of fluorine adatoms and therefore control energy gap between the impurity and conduction bands. Futhermore, electron beam irradiation also offers a valuable way to pattern conductive structures in fluorinated graphene *via* the irradiation-induced dissociation of fluorine from the fluorinated graphene. This technique can be extended to the patterning of semiconducting nano-ribbons in fluorinated graphene where the spatial localization of electrons is just a few nm. The second type of chemical functionalization presented in this thesis is the intercalation of few layer graphene with ferric chloride which greatly enhances the electrical conductivity of few layer graphene materials making them the best known transparent conductors.

Publications

- **(10)** All Graphene Photodetectors. **Freddie Withers**, Thomas H. Bointon, Saverio Russo, and Monica F. Craciun. (In Preparation).
- **(9)** Level spacing statistics of a graphene quantum dot enclosed within fluorinated graphene. **Freddie Withers**, Marc Dubois, Saverio Russo, and Monica F. Craciun. (In Preparation).
- **(8)** Tuning the transport gap of fluorinated graphene via electron beam irradiation. Steven Martins, **Freddie Withers**, Marc Dubois, Saverio Russo, and Monica F. Craciun (Submitted to Nano Letters).
- **(7)** Novel highly conductive and transparent graphene based conductors. Ivan Khrapach, **Freddie Withers**, Thomas Bointon, Dmitry Polyushkin, William Barnes, Saverio Russo, and Monica F. Craciun *Advanced Materials.* 24, 2844 (2012)
- **(6)** Electrical transport in suspended and double gated trilayer graphene. Tymofiy Khodkov, **Freddie Withers**, David Christopher Hudson, Monica Felicia Craciun, and Saverio Russo *Appl. Phys. Lett.* 100, 013114 (2012).
- **(5)** Nanopatterning of Fluorinated Graphene by Electron Beam Irradiation. **Freddie Withers**, Thomas H. Bointon, Marc Dubois, Saverio Russo, and Monica F. Craciun *Nano. Lett.* 11 (9), 3912 (2011).
- **(4)** Phonons in potassium-doped graphene: The effects of electron-phonon interactions, dimensionality, and adatom ordering. C. A. Howard, M. P. M. Dean and **F. Withers** *Phys. Rev. B.* 84, 241404(R) (2011).
- **(3)** Tuning the electronic transport properties of graphene through functionalisation with fluorine. **Freddie Withers**, Saverio Russo, Marc Dubois and Monica F Craciun *Nanoscale Research Letters.* 6, 526 (2011).
- **(2)** Electrochemical doping of graphene with toluene. A.A. Kaverzin, , S.M. Strawbridge, A.S. Price, **F. Withers**, A.K. Savchenko, D.W. Horsell *Carbon.* 49, 12 3829 (2011).
- **(1)** Electron properties of fluorinated single-layer graphene transistors. **F. Withers**, M. Dubois, and A. K. Savchenko *Phys. Rev. B* 82, 073403 (2010).

Contents

List of Figures

Chapter 1

Introduction

Since the advent of the first silicon transistor in the late 1940's [1] (see, Figure 1.1(a)) the size of the individual transistor has reduced dramatically resulting in an exponential increase of the number of devices per chip with time [2](Moore's law). This means that the electronics industry has been able to grow rapidly with time (see, 1.1(b)) leading to many world changing innovations, such as the personal computer, mobile communications and digital display technologies [3].

Although major advances in semiconductor materials have led to world changing innovations, conventional semiconductor technologies are incompatible with a number of applications. For example, conventional semiconductor materials (such as, Si and Ge) which are currently used in many solid state devices are not compatible with future transparent and flexible technologies since they are brittle and opaque. Therefore, in recent years a change in emphasis on the materials used in devices has ensued, and new materials must be chosen based on their mechanical flexibility, high optical transparency and high electrical conductivity. Atomically thin materials are an emerging new class of systems which offer the right combination of unique properties able to overcome the aforementioned limitations of conventional semiconductors.

The most promising of these newly realized materials is graphene, a monolayer of carbon atoms. Graphene and few layer graphene were isolated in 2004 by researchers at the University of Manchester by exfoliation from a graphite crystal [4]. As opposed to other carbon materials (i.e. diamond and graphite which have a 3 dimensional structure, carbon nanotubes in which electrons are confined in 1 dimension and C60 molecule which is the 0D allotrope) graphene is a perfect 2 dimensional crystal, see Figure 1.2(a)-(d).

Since its discovery, graphene research has truly expanded at an unprecedented pace

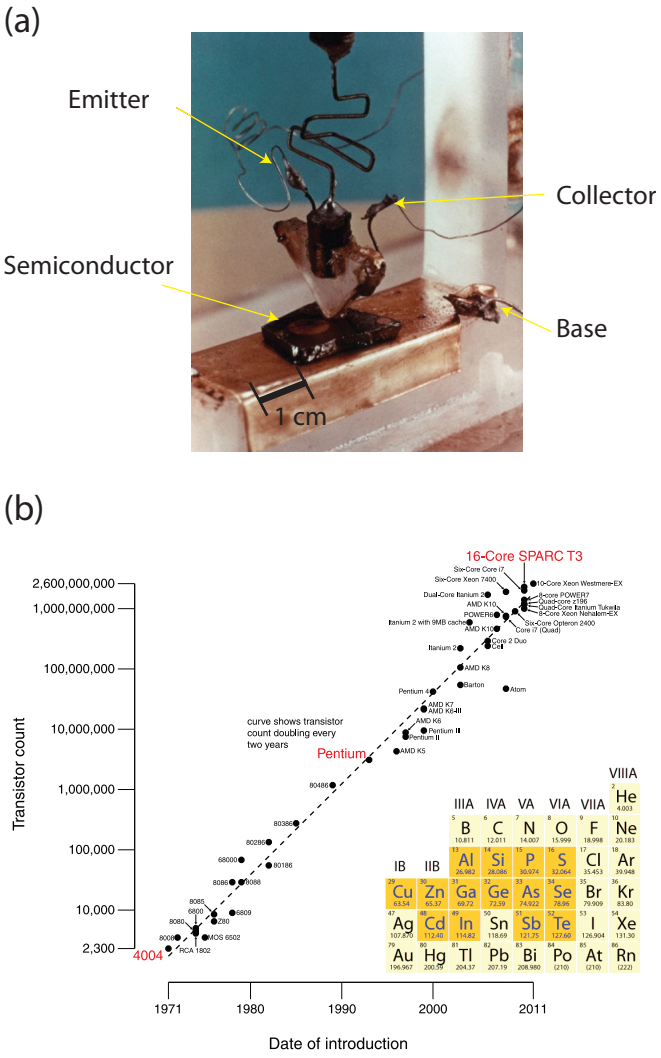

Figure 1.1: (a) An image of the first bipolar transistor device studied in 1948. Here a small current flowing between the base and the emitter can modulate a much larger current between the collector and emitter. (b) The evolution of Moor's law with key processors highlighted in red. (inset) conventional semiconductor elements.

due to the ease with which graphene devices can be manufactured and due to the seemingly endless list of superior properties which enable this material to be of tremendous importance to future technology. The charge carriers in graphene traverse macroscopic distances without scattering and have high mobilities, making graphene of interest for high frequency applications such as analogue transistor [5].This atomically thin mate-

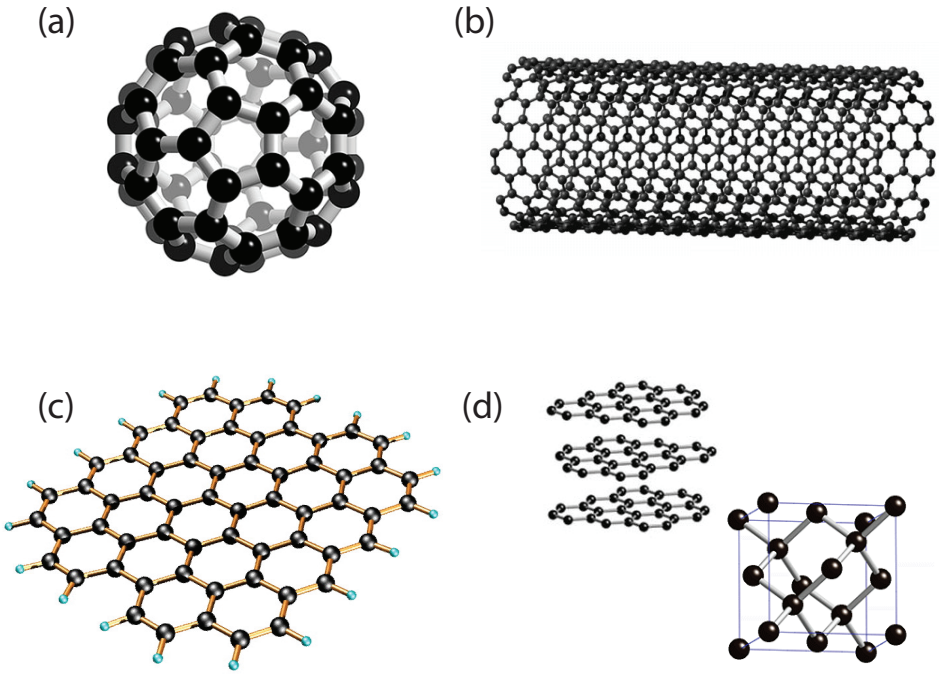

Figure 1.2: Allotrope's of carbon (a) 0-Dimensional buckyballs (b) 1-Dimensional carbon nanotubes (c) 2-Dimensional graphene and (d) 3-Dimensional graphite and diamond.

rial has high mechanical strength [6] which means it can exist as an isolated membrane without breaking and it can be used in high frequency resonators [7]. It is highly transparent, but at the same time it absorbs radiation over a broad band of energies and is flexible [8]. These properties make graphene a stand out material for flexible transparent conductors [9] and also for energy harvesting applications, which are of tremendous importance for social-economic stability due to finite energy and material resources [10].

Although graphene displays some remarkable properties, it still lacks in a few key areas which limit its functionality in device applications. Unlike silicon, graphene has no band-gap with the conduction and valence bands touching each other [11]. A

consequence of this is that current cannot be switched off by a gate voltage in a graphene field effect transistor (FET). A potential route in which a band gap may be opened is via chemical functionalization where atoms may be covalently bonded to graphene [12].

Furthermore, since graphene is a good electrical conductor - better than copper - and transparent over a wide wavelength range it is expected to become important in displays, smart phones and solar cells to name a few. To date, Indium Tin Oxide (ITO) is the most widely used transparent electrical conductor by display industries. ITO still has a much lower resistivity than pristine graphene or graphene grown by chemical vapor deposition (CVD). To make graphene a competitive candidate its resistivity needs to be reduced to values lower than the resistivity of ITO which has an optical tranparency of $T \approx 85\%$ and $R_{sq} \approx 15\Omega$ [13]. This thesis demonstrates that a possible route to achieve this is by chemical doping of graphene or few layer graphene materials [14]. This process transfers electrons from or to the graphene ultimately leading to an enhancement of the conductivity due to an increase in carrier density. The strongest electron transfer mechanism can be achieved by intercalation, where chemical species can diffuse through the planes of graphene and heavily dope the graphene sheets [15].

The main theme of this thesis is the study of how chemical treatment of graphene can change its properties and make graphene useful for a wider range of applications.

1.0.1 Fluorinated Graphene

The chemical functionalization of graphene with fluorine ad-atoms is extensively studied in chapters 4 to 7 [16–18]. The electrical properties of fluorinated graphene are vastly different compared to the properties of pristine graphene with the material becoming an insulator for high fluorine contents. Figure 1.3(a) and (b) show the crystal structure of graphene and of fluorinated graphene respectively. Upon fluorination, the crystal structure of fluorinated graphene changes from a purely 2-dimensional material to a 3-dimensional material with the carbon atoms being pulled out of the graphene plane. Because the delocalized electrons are now tightly bound in a covalent bond between the carbon atom and the fluorine atom the material is transformed into an insulator.

Before commencing this work, only electrical transport experiments have been conducted on hydrogenated graphene and it has not been possible to measure the value of the intrinsic band-gap [19]. This is due to the presence of disorder induced sub-gap states which assist the flow of electrical current, therefore masking the direct observation of a band gap [19]. A possible explanation of the origin of the disorder in this system is that the random attachment of hydrogen atoms to the graphene and bond

saturation was not achieved. In this scenario charge transport takes place via localized states discussed further in Section 2.4. This fact prevents the use of hydrogenated graphene as an insulating barrier material or as a practical transistor device which will operate at room temperature. For this reason in this work fluorine is chosen. This element is expected to saturate graphene with covalent bonds [20] and therefore a band gap should be realized.

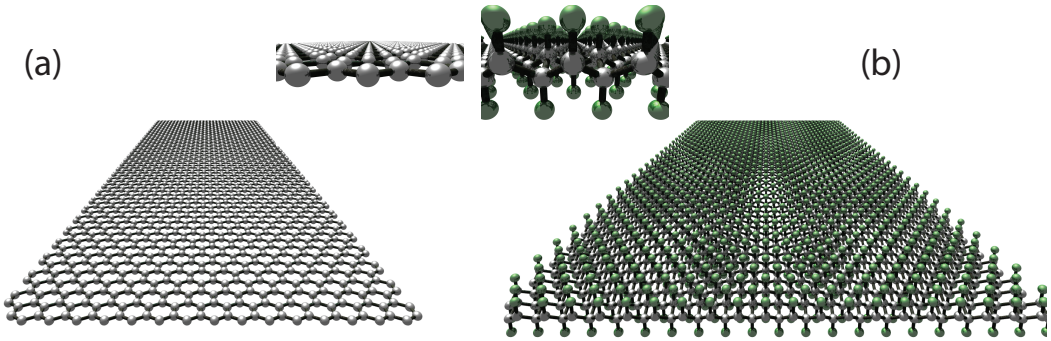

Figure 1.3: (a) Pristine graphene crystal structure (b) crystal structure of fluorinated graphene.

1.0.2 Doped graphene and Intercalated few layer Graphene

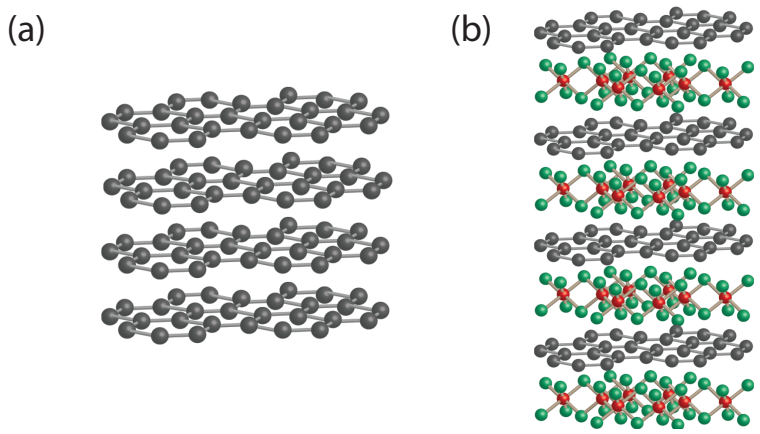

Figure 1.4: Crystal structure of a FeCl3 intercalated few layer graphene flake, with Fe (red), Cl (green) and C (black).

The research field of graphite intercalation compounds dates back to the early 20 th century [15, 21], with more than 100 known intercalation compounds [15] exhibiting a large variety of properties including magnetism and intrinsic superconductivity [15] . To date, there are many known intercalant species and a detailed review of the various compounds is available [15]. Many of these intercalation molecules are highly reactive and therefore the resultant graphite intercalation compound will not be stable in ambient conditions. We found an ideal acceptor molecule -i.e. $FeCl_3$- which gives an air stable intercalated compound [15]. Figure 1.4(a) and (b) shows pristine few layer graphene and $FeCl_3$ intercalated few layer graphene. It is found that there is a large electron charge transfer from the graphene to the $FeCl_3$ layer. This renders the graphene layers heavily hole doped, with an extremely low $R_{sq} \approx 8\Omega$. At the same time the high optical transparency of graphene is preserved at $T \approx 85\%$ for 5 layer graphene. This $FeCl_3$ -intercalated few-layer graphene material is air stable on a time scale of 1 year [14]. Detailed studies on this novel few-layer graphene intercalated compound are presented in Chapter 8 [14].

Chapter 2

Theoretical Concepts.

2.1 Band Structure of Graphene.

Although graphene was isolated experimentally only in 2004, theoretically its band structure was first studied in 1947 [11]. The band spectrum for graphene is well captured by the tight binding approximation as described below [22]. Carbon contains 6 electrons $1s^2 2s^2 2p^2$. The core $1s^2$ electrons are tightly bound to the nucleus and do not interact while the valence electrons $2s^2 2p^2$ interact with neighbouring carbon atoms. The electronic properties of graphene can be determined by the valence electrons. Specifically, the valence electrons of carbon form 2s, $2p_x$, $2p_y$ and $2p_z$ orbitals. These electronic orbitals give rise to covalent bonds between neighbouring atoms in molecules or crystals, in order to create the covalent bonds the 2s orbital hybridizes with the 2p orbitals to form sp^n where n = (1,2,3). These three hybridizations can be seen in the different forms of carbon. The materials of main interest to this thesis are graphene and fluorographene which have sp^2 and sp^3 hybridizations respectively [12, 23, 24].

Figure 2.1 shows the positions of the carbon atoms in the graphene crystal. The graphene structure is composite and it consists of two sub-lattices of carbon atoms, indicated by Γ_A (red) and Γ_B (blue), see Figure 2.1(a). The energy spectrum has been calculated in [11, 22], here the derivation is followed from [25]. The primitive translation vectors for the crystal are,

$$\mathbf{a_1} = a\left(\frac{3}{2}, \frac{\sqrt{3}}{2}\right), \quad \mathbf{a_2} = a\left(\frac{3}{2}, -\frac{\sqrt{3}}{2}\right) \tag{2.1}$$

where a is the inter-atomic separation (C-C = 1.42Å) which we set to unity for

further derivation. Any atom of the Γ_A sub-lattice at position $\mathbf{r} = \mathbf{a_1}n_1 + \mathbf{a_2}n_2$ where n_1,n_2, integers are connected to its nearest neighbours on sub-lattice Γ_B by the vectors δ_i,

$$\delta_\mathbf{1} = \frac{2}{3}\mathbf{a_1} - \frac{1}{3}\mathbf{a_2}, \quad \delta_\mathbf{2} = \frac{2}{3}\mathbf{a_2} - \frac{1}{3}\mathbf{a_1}, \quad \delta_\mathbf{3} = -\delta_\mathbf{1} - \delta_\mathbf{2} = -\frac{1}{3}\mathbf{a_1} - \frac{1}{3}\mathbf{a_2}. \tag{2.2}$$

A second set of vectors $\delta_i^{'}$ define the nearest neighbour lattice sites from sub-lattice Γ_B such that $\delta_\mathbf{i}^{'} = -\delta_\mathbf{i} + \mathbf{d}$, where $\mathbf{d}$ is a vector from the Γ_A sub-lattice to the Γ_B sub-lattice. The reciprocal lattice vectors can be found from $\mathbf{a_i} \cdot \mathbf{b_j} = 2\pi\delta_{ij}$ and are,

$$\mathbf{b_1} = \frac{2\pi}{3}\left(1, \sqrt{3}\right), \quad \mathbf{b_2} = \frac{2\pi}{3}\left(1, -\sqrt{3}\right), \tag{2.3}$$

Figure 2.1(b) shows the first Brillouin zone which has hexagonal shape. This gives rise to the high symmetry points $\Gamma, K^{'}, K$ and M with coordinates $(0,0)$, $(\frac{2\pi}{3}, -\frac{2\pi}{3\sqrt{3}})$, $(\frac{2\pi}{3}, \frac{2\pi}{3\sqrt{3}})$ and $(\frac{2\pi}{3}, 0)$ respectively.

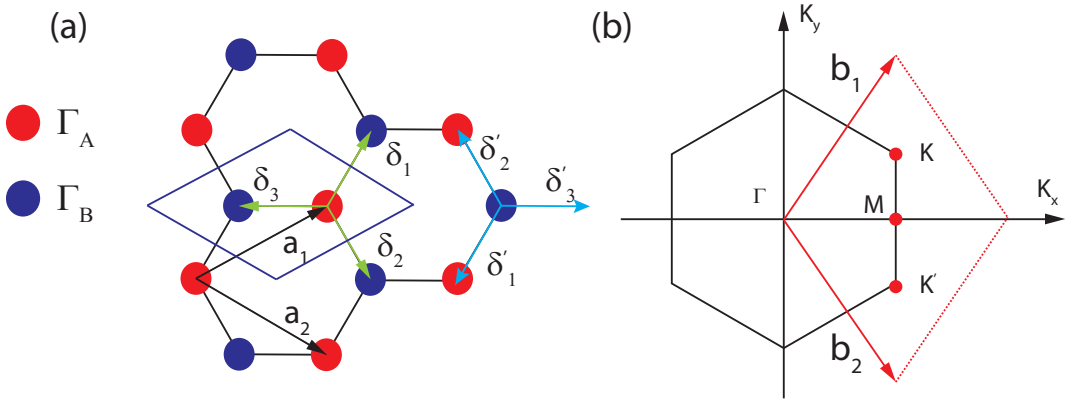

Figure 2.1: (a) Honeycomb structure consisting of two triangular sub-lattices Γ_A and Γ_B. The highlighted blue box contains the unit cell. (b) Corresponding Brillouin zone, the Dirac cones are located at K and $K^{'}$

.

The eigenstates for a periodic crystal can be written as Wannier functions where,

$$\Psi_{nk} = \frac{1}{\sqrt{N}} \sum_i exp(i\mathbf{k} \cdot \mathbf{r_i}) \xi_n(\mathbf{r} - \mathbf{r_i}) \tag{2.4}$$

and the sum runs over all the lattice points i, $\mathbf{r_i} = \mathbf{a_1}n_i + \mathbf{a_2}n_i$ with n the band label and k the states in that band.

The energy levels may be computed via the variational method,

$$E_k = \frac{\int d\tau \Psi^* H \Psi}{\int d\tau \Psi^* \Psi} = \frac{\sum_i exp(i\mathbf{k}\cdot\mathbf{r_i}) \int d\tau \xi^*(\mathbf{r}) H \xi(\mathbf{r}-\mathbf{r_i})}{\sum_i exp(i\mathbf{k}\cdot\mathbf{r_i}) \int d\tau \xi^*(\mathbf{r}) \xi(\mathbf{r}-\mathbf{r_i})}. \tag{2.5}$$

Taking the normalization of the Wannier functions to be unity, we obtain,

$$E_k = \int d\tau \xi^*(\mathbf{r}) H \xi(\mathbf{r}) + \sum_{NN} exp(i\mathbf{k}\cdot\mathbf{r_i}) \int d\tau \xi^*(\mathbf{r}) H \xi(\mathbf{r}-\mathbf{r_i}), \tag{2.6}$$

where NN corresponds to the sum over nearest neighbours only. We can write a wavefunction composed of a linear combination of identical orbitals ξ_{Γ_A} and ξ_{Γ_B} localized around each of the before mentioned points of the primitive cell as follows,

$$\xi(\mathbf{r}) = h_{\Gamma_A} \xi_{\Gamma_A}(\mathbf{r}) + h_{\Gamma_B} exp(i\mathbf{k}\cdot\mathbf{d}) \xi_{\Gamma_B}(\mathbf{r}-\mathbf{d}). \tag{2.7}$$

By substituting eq. 2.7 into the energy functional eq. 2.6 we obtain,

$$\begin{aligned} E_k = {} & h^*_{\Gamma_A} h_{\Gamma_A} \int d\tau \xi^*_{\Gamma_A}(\mathbf{r}) H \xi_{\Gamma_A}(\mathbf{r}) \\ & + h^*_{\Gamma_B} h_{\Gamma_B} \int d\tau \xi^*_{\Gamma_A}(\mathbf{r}-\mathbf{d}) H \xi_{\Gamma_A}(\mathbf{r}-\mathbf{d}) \\ & + h^*_{\Gamma_A} h_{\Gamma_B} \sum_j exp(i\mathbf{k}\cdot\delta_\mathbf{j}) \int d\tau \xi^*_{\Gamma_A}(\mathbf{r}) H \xi_{\Gamma_B}(\mathbf{r}-\delta_\mathbf{j}) \\ & + h^*_{\Gamma_B} h_{\Gamma_A} \sum_j exp(i\mathbf{k}\cdot\delta'_\mathbf{j}) \int d\tau \xi^*_{\Gamma_B}(\mathbf{r}-\mathbf{d}) H \xi_{\Gamma_A}(\mathbf{r}-\mathbf{d}-\delta'_\mathbf{j}), \end{aligned} \tag{2.8}$$

which can further be simplified by symmetry considerations as follows,

$$\begin{aligned} \int d\tau \xi^*_{\Gamma_A}(\mathbf{r}) H \xi_{\Gamma_A}(\mathbf{r}) = \int d\tau \xi^*_{\Gamma_B}(\mathbf{r}-\mathbf{d}) H \xi_{\Gamma_B}(\mathbf{r}-\mathbf{d}) = \beta \\ \int d\tau \xi^*_{\Gamma_A}(\mathbf{r}) H \xi_{\Gamma_B}(\mathbf{r}-\delta_\mathbf{i}) = \int d\tau \xi^*_{\Gamma_B}(\mathbf{r}-\mathbf{d}) H \xi_{\Gamma_A}(\mathbf{r}-\mathbf{d}-\delta'_\mathbf{i}) = \gamma \end{aligned} \tag{2.9}$$

where β is the on-site energy and is defined as zero while γ is the nearest neighbour hopping parameter $\approx$ 2.8 eV. Substituting eq. 2.9 into eq. 2.8, it can be shown that

the energy momentum dispersion can be rewritten as,

$$E_k = \begin{pmatrix} h^*_{\Gamma_A} & h_{\Gamma_B} \end{pmatrix} \begin{pmatrix} 0 & \gamma \sum_j exp(i\mathbf{k}\cdot\delta_\mathbf{j}) \\ \gamma \sum_j exp(i\mathbf{k}\cdot\delta'_\mathbf{j}) & 0 \end{pmatrix} \begin{pmatrix} h_{\Gamma_A} \\ h_{\Gamma_B} \end{pmatrix}. \tag{2.10}$$

The dispersion relation E_k can be calculated for the time independent case, $H\Psi = E\Psi$, eigenvalues for this Hamiltonian can be expressed using the relation $|\mathbf{HI} - E_k\mathbf{I}| = 0$

$$\begin{vmatrix} -E_k & \gamma \sum_j exp(i\mathbf{k}\cdot\delta_\mathbf{j}) \\ \gamma \sum_j exp(i\mathbf{k}\cdot\delta'_\mathbf{j}) & -E_k \end{vmatrix} = 0. \tag{2.11}$$

Upon solving the determinant we finally arrive at the energy-momentum dispersion relation,

$$E_k = \pm\gamma \sqrt{\sum_{j=1}^{3} exp(i\mathbf{k}\cdot\delta_\mathbf{j}) \sum_{j=1}^{3} exp(-i\mathbf{k}\cdot\delta_\mathbf{j})}. \tag{2.12}$$

Which can be expanded into the form,

$$E_k = \pm\gamma \sqrt{(1 + 4cos^2(\frac{\sqrt{3}k_x}{2}) + 4cos(\frac{\sqrt{3}k_x}{2})cos(\frac{3k_y}{2}))}. \tag{2.13}$$

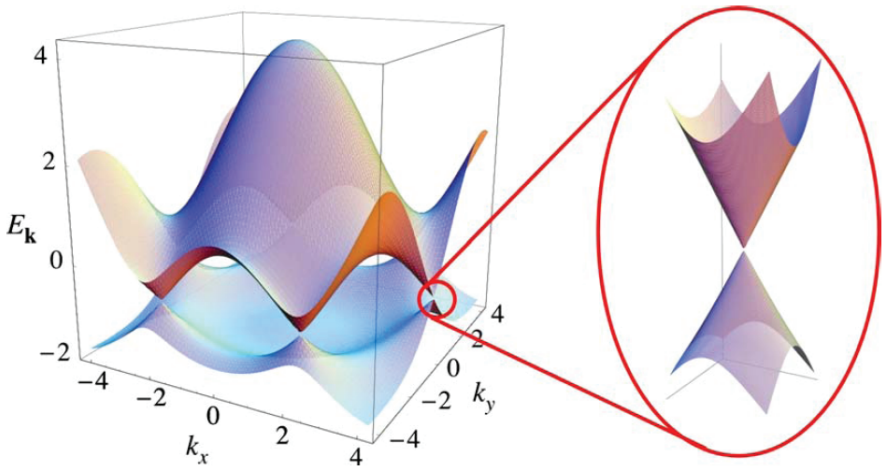

Figure 2.2: Adapted from [22] Color map of the band spectrum of graphene, showing the valence and conduction band for $-2 \leq E < 4eV$.

Figure 2.2 shows the energy dispersion for graphene described by eq. 2.13 and plotted for the first Brillouin zone. The positive solution of 2.13 corresponds to the conduction band while the negative solution corresponds to the valence band. It can be seen that the positive and negative solutions of eq. 2.13 meet at specific points corresponding to $E_k = 0$. Figure 2.3 shows a 2D colour map for the first Brillouin zone, it can be seen that there exist 6 points in k-space where the energy becomes zero (highlighted in red). These zero energy points can be found by setting eq. 2.13 to zero and solving for k_x and k_y which exist within the first Brillouin zone.

$$\mathbf{K_D^{\pm}} = \pm\frac{2\pi}{3\sqrt{3}}\left(\sqrt{3}, 1\right). \tag{2.14}$$

Where the $+$ corresponds to points in k and $-$ corresponds to k'. These regions where the conduction and valence bands touch are called Dirac points k_D. If we expand the Hamiltonian eq. 2.11 around the two neighboring Dirac points along the k_y axis by substituting $\mathbf{k} = \mathbf{k_D} + \mathbf{\Delta k}$. We arrive at the expression,

$$\begin{vmatrix} -E_k & \frac{-3i\gamma}{2} exp(\pm i\frac{2\pi}{3})(\Delta k_x \mp i\Delta k_y) \\ \frac{3i\gamma}{2} exp(\mp i\frac{2\pi}{3})(\Delta k_x \pm i\Delta k_y) & -E_k \end{vmatrix} = 0. \tag{2.15}$$

Solving 2.15 gives,

$$E_k = \pm\frac{3\gamma}{2}|\mathbf{k}| = \pm v_F|\mathbf{k}| \tag{2.16}$$

where $v_F = \frac{3\gamma}{2}$ is the Fermi velocity. Therefore the dispersion relation is linear and as a consequence the effective mass of the charge carriers is zero [26].

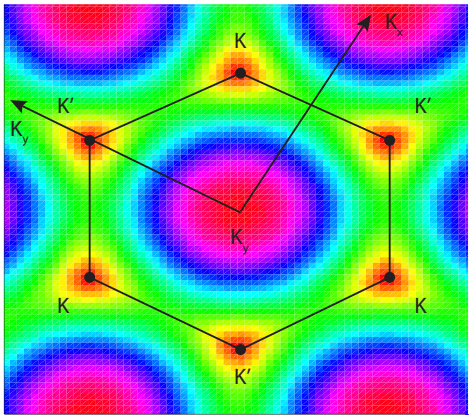

Figure 2.3: A cut through the (K_x, K_y) plane, regions of same colour correspond to the same energy.

This means that graphene differs dramatically from conventional parabolic band materials. This difference in band structure and the realization of Dirac Fermions in an easily fabricated mesoscopic sample is at the heart of why graphene has received such great interest over the past 8 years.

2.2 Band gap opening through Chemical functionalisation with fluorine and Hydrogen.

As discussed in Section 2.1 graphene has one free electron per carbon site, this allows for the transformation of graphene through functionalization. Functionalization is the attachment of atoms or molecules through covalent bonding or Van der Waals forces. For covalent attachment fluorine and hydrogen are key contenders since they open a large energy gap in the otherwise gap-less dispersion relation of graphene [20, 21]. Predictions based on *ab initio* calculations for different crystal configurations show that graphene fluoride, also known as fluorographene, is expected to have a large band gap between 3.5 eV and 7.4 eV [12, 23].

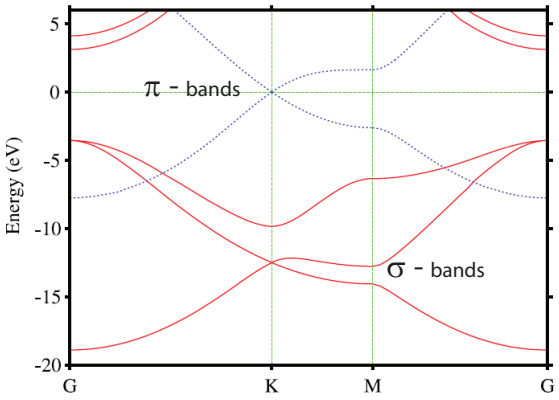

Figure 2.4: adapted from [23] shows the band structure of graphene along high symmetry points. The blue lines correspond to the π bands described above while the red lines correspond to bands arising from the sigma bonds.

Figure 2.4 shows the band structure of pristine graphene along the high symmetry points of the Brillouin zone. The blue linear bands called the π bands arise from the delocalized $2p_z$ electrons whereas the red σ bands arise from the remaining σ electrons.

If the graphene sheet is saturated with hydrogen or fluorine atoms and all available free electrons are localized, the π bands disappear. Figure 2.5(a) and (b) show the resultant band structures for hydrogenated and fluorinated graphene respectively. Note the absence of the π bands and the opening of a large band gap in the case of fully hydrogenated and fully fluorinated graphene.

Due to the large electro-negativity of the fluorine atom the charge which is localized in the $C-F$ bond resides mainly on the fluorine atom, and calculations show that charge

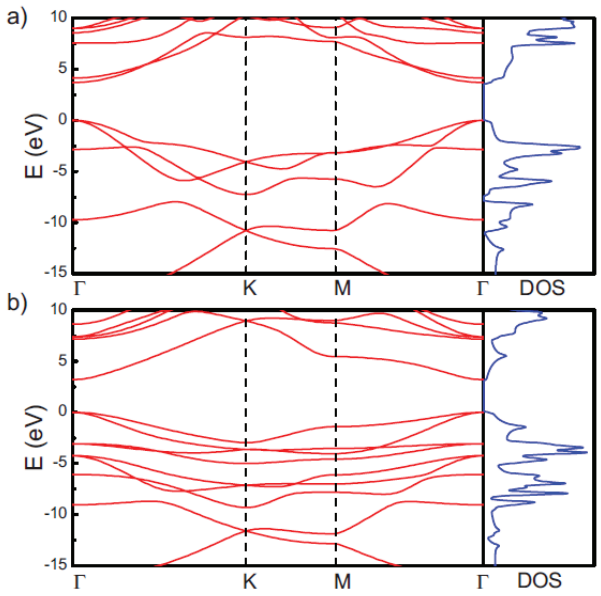

Figure 2.5: adapted from [23] shows the resultant band structures for a) fully hydrogenated and b) fully fluorinated graphene in the chair configuration.

transfered to the fluorine atom is 0.3e. This charge transfer results in a slight expansion of the lattice by 0.05Å [27]. At the same time, the hybridization changes from sp^2 to sp^3 hybridization and the crystal structure becomes 3-dimensional.

2.3 The lightly doped semiconductor model.

In the previous section it was shown that chemical functionalization of graphene with fluorine or hydrogen can open a band gap in the energy spectrum therefore creating a new class of 2-dimensional semiconductors. However, the disorder which originates from partial coverage of covalently bonded ad-atoms results in a non fully developed band gap. Electron transport measurements are sensitive to impurity states which come from missing covalent bonds therefore the fully developed band gap is not seen in transport measurements. The electrical transport of such materials is described by the lightly doped semiconductor model. In this model there exists within a larger band-gap an impurity band of states which come from disorder or impurities in the material. Figure 2.6 shows a schematic of the energy bands in the lightly doped semiconductor model. In this model electrons are thermally excited over an energy gap which is much smaller than the full band gap. Indeed, the important energy scale when considering

thermally activated transport is ϵ_1 which is the energy between the occupied band of states and the conduction band.

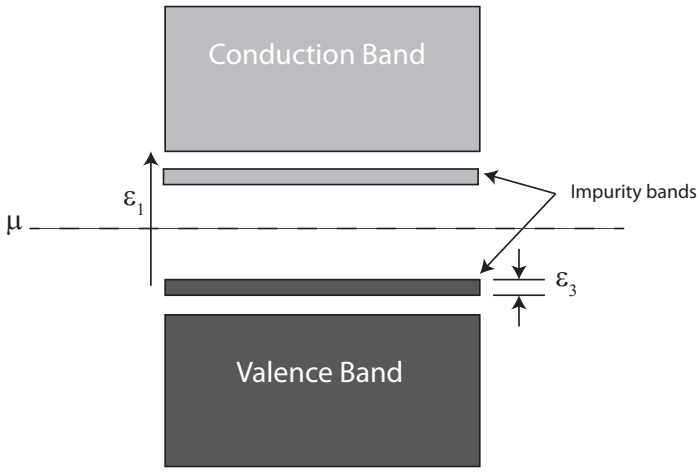

Figure 2.6: Energy band schematic for a lightly doped semiconductor. Dark grey corresponds to occupied states while light grey corresponds to un-occupied states.

At high temperatures semiconductors possess an intrinsic electrical conductivity due to carriers which are thermally excited over the intrinsic band gap.6 -i.e. energy gap between the top and bottom of valence and conduction band respectively. The concentration of carriers which contribute to the conductivity depends on temperature via the following relation [28],

$$n = p = \frac{(2\pi\sqrt{m_e m_h}k_B T)^{3/2}}{4\pi^3\hbar^3} exp(-E_g/k_B T). \tag{2.17}$$

Here n and p correspond to the electron and hole carrier concentration while m_e and m_h are the effective masses of the electrons and holes and E_g is the band gap. For a large value of E_g the carrier concentration can decrease extremely rapidly with temperature. At sufficiently low temperatures the concentration of thermally excited carriers can be less than the concentration contributed by impurities. In this region transport is totally governed by the the nature of the impurities and is known as the extrinsic region.

Figure 2.7 shows a schematic of the logarithm of the resistivity for a lightly doped semiconductor plotted against inverse temperature. Region A (High Temperature) is known as the intrinsic region. Here electron transport takes place through thermally activated carriers. Regions (B-D) correspond to extrinsic conduction, in these regions transport is governed by the specific nature of the impurities.

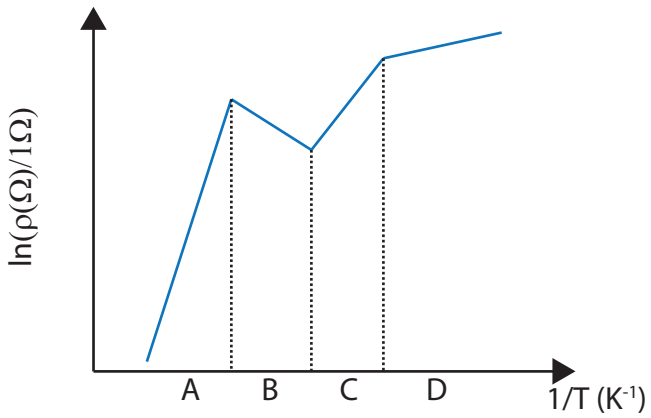

Figure 2.7: The inverse temperature dependence of the natural logarithm of the resistivity for a typical lightly doped semiconductor.

If the impurities have an ionization energy much smaller than the size of the gap then there exists a region B where the resistivity is entirely determined by the temperature dependence of the mobility. In this case a reduction of resistance with decreasing temperature is often observed and it is commonly attributed to a weaker electron-phonon scattering for instance.

A further decrease of the temperature leading to region C results in a gradual freezing out of the impurity electrons. The increase of resistance in this region is due to a rapid decrease of free electron concentration. In regions $(C - D)$ electron transport is through hopping conduction through localized states within the impurity band.

Figure 2.8 shows the inverse temperature dependence of a lightly doped sample of germanium. The temperature dependence of the resistivity can be well fit by the following expression,

$$\rho^{-1}(T) = \rho_1^{-1} exp(-\epsilon_1/k_B T) + \rho_3^{-1} exp(-\epsilon_3/k_B T). \tag{2.18}$$

The first term of eq. 2.18 corresponds to the extrinsic region A - i.e. band conduction - while the second term corresponds to the hopping conduction here $\epsilon_3 < \epsilon_1$. Chapter 7 shows that partially fluorinated graphene is a lightly doped semiconductor and that good agreement with the above model is found.

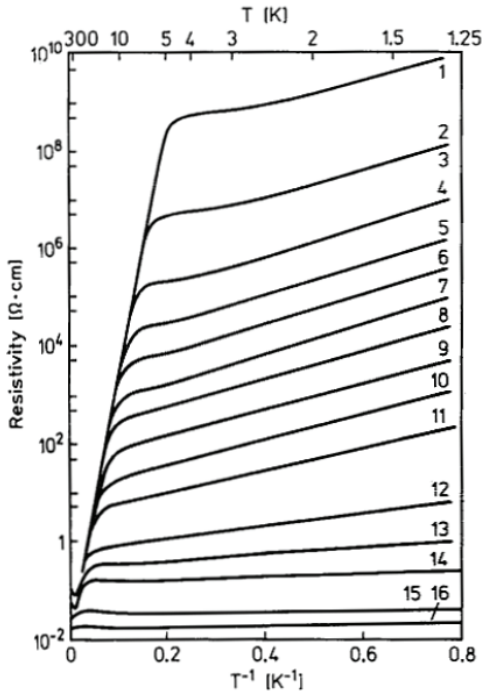

Figure 2.8: Resistivity data for lightly doped Germanium for various doping levels. Adapted from [28] and references therein.

2.4 Hopping Conduction.

2.4.1 System of independent electrons: Mott hopping

Electron transport in disordered crystals can be explained by Mott variable range hopping (MVRH). In particular partially fluorinated graphene can be considered a disordered crystal. The disorder originates from randomly bonded sp^3 fluorine atoms. At very low fluorine coverage level the scattering of electrons off fluorine ad-atoms leads to an mobility gap opening in the π bands. Within this gap exists localized states which can be approximated to a constant density of states $g(E_F)$ which exist within a larger mobility gap. Contrary to the intrinsic band gap, a mobility gap separates the localized states from the extended states. The electron transport in such a system can be described by Mott Variable Range Hopping (MVRH). For low temperatures, electrons have a higher probability of jumping to a site at a larger distance away. As at larger distances there are more sites and this means the activation energy may be smaller for distant sites [28, 29]. Considering a system with a constant density of localized states

$g(E_F)$ at the Fermi level, the probability for an electron to jump a distance R with an activation energy Γ and localization radius ξ is,

$$P \approx exp(-2R/\xi - \Gamma/k_BT). \tag{2.19}$$

Within a sphere of radius R the average spacing in energy Γ between the states near the Fermi level is $\Gamma = 3/(4\pi R^3 g(E_F))$ [28]. Maximizing P with respect to the hopping length R gives the equality $2/\xi = 9/(4\pi g(E_F)R^4 k_BT)$ and it follows that for the maximum jump frequency,

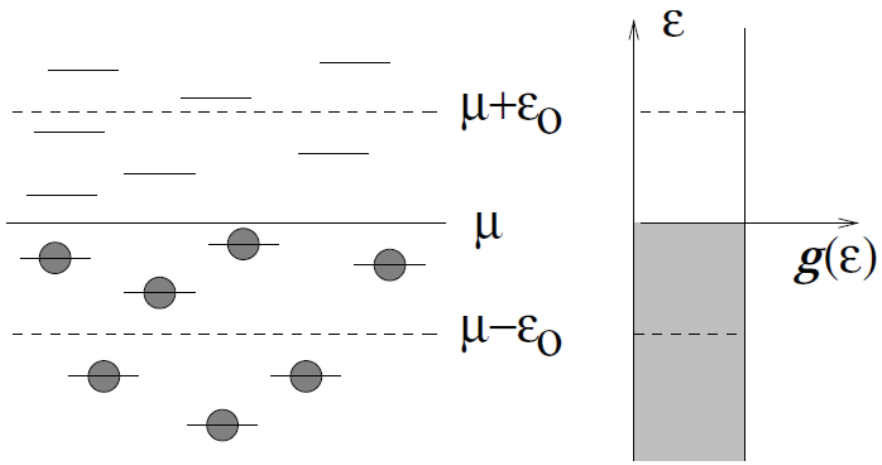

Figure 2.9: Left: Construction of a band containing states whose energies are separated from the Fermi level by less than ϵ_0.Right: showing the Density of states occupied states are highlighted in gray.

$$P \approx \sigma \approx exp(-T_0/T)^{1/4} \tag{2.20}$$

with

$$T_0 = \beta/k_B\xi^3 g(E_F). \tag{2.21}$$

Using percolation methods the value of β has been found to be 21.2 [28].
The optimum hopping length R_M grows as the temperature is lowered according

to,

$$R_M(T) = \xi \left(\frac{T_0}{T}\right)^{1/4}. \tag{2.22}$$

This mechanism of conduction is known as 'variable range hopping' because of this behaviour. The band providing the maximum of conduction has width,

$$\Gamma(T) = k_B T (T_0/T)^{1/4}. \tag{2.23}$$

The conductivity is to a good approximation entirely determined by the contribution of this optimal band.

The Mott law may be generalized to the case of an arbitrary spatial dimensionality d. This gives,

$$\sigma = \sigma_0 exp(-T_0/T)^{\frac{1}{d+1}}. \tag{2.24}$$

In particular for 2-dimensions,

$$\sigma = \sigma_0 exp(-T_0/T)^{\frac{1}{3}} \tag{2.25}$$

with $T_0 = \beta/K_B\xi^2 g(E_F)$ where $\beta = 13.8$. This model assumes a constant density of localized states which exist within a larger mobility gap, in reality the picture is more complicated with the density of localized states being irregular throughout the transport gap. This model however works extremely well for a large variety of disordered crystals. We will adopt this model to describe the electrical conduction in partially fluorinated graphene presented in Chapter 4.

2.4.2 System of interacting electrons

When the coverage of fluorine ad-atoms increases in the partially fluorinated graphene, then electron - electron interactions must be taken into account. This enhancement of the electron - electron interaction is due to the increased localization of the electrons. In this scenario, the fluorinated regions will enclose conductive graphene regions and Coulomb interaction needs to be taken into account for an electron to hop from island to island. The Mott law is derived for a system which has a constant density of states at the Fermi surface. The Coulomb field generated by the charge carriers is not taken into account by the Mott theory of hopping conduction [28]. It was shown that the electrostatic interaction creates a Coulomb gap in the density of states near the Fermi

level [28].

In a system in its ground state at zero temperature, the Fermi level separates occupied and empty states. If the site i is occupied by an electron and site j is vacant, then moving an electron from site i to site j involves a change in the total energy E_i^j.

$$E_i^j = E_j - E_i - \frac{e^2}{4\pi\epsilon_0\epsilon_r r_{ij}}. \tag{2.26}$$

The electron can be thought of moving from infinity where the potential is set to zero. The change of the total energy is equal to $-E_i$. Then the electron moves from infinity to site j. This would contribute energy E_j provided that the system was in its ground state and the site i is occupied. However, this site is now empty and the last term in eq. 2.26 corresponds to the extra attraction of the electron-hole pair creation.

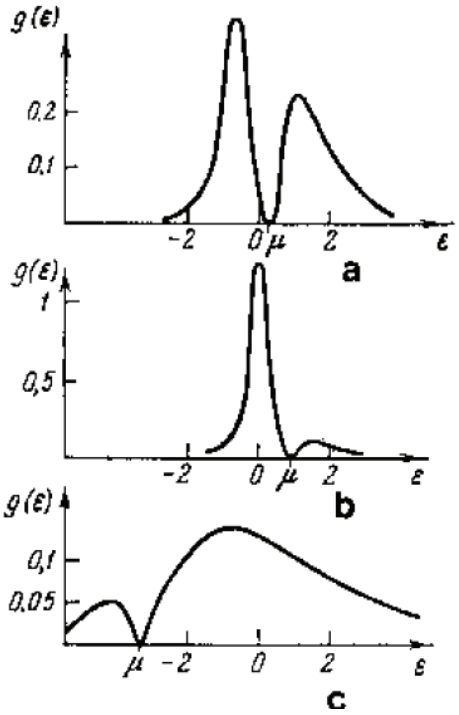

Figure 2.10: (a-c) Density of states in the presence of a Coulomb gap for various doping levels. Adapted from [28] and references therein.

Because the system is initially in the ground state a hopping event from site i to site j will result in an increase of the system energy $E_i^j \geq 0$. This has to be satisfied in eq. 2.26 given two sites which lie within the Coulomb gap of width E then $E_j - E_i < E$. The distance between two sites cannot be smaller than $e^2/4\pi\epsilon_0\epsilon_r E$ so the concentration

cannot be higher than $N(E) = (4\pi\epsilon_0\epsilon_r E/e^2)^3$. Therefore the density of states follows the inequality,

$$g = \frac{\partial[N(E)]}{\partial E} < 3(4\pi\epsilon_0\epsilon_r/e^2)^3 E^2 \tag{2.27}$$

and one arrives at,

$$g = \alpha_3(E-\mu)^2(4\pi\epsilon_0\epsilon_r/e^2)^3 \tag{2.28}$$

where E is now a single-particle energy and α_3 is a constant of order unity. eq. 2.28 is only valid if $g(E) < g_c$ (g_c is the density of states without interactions). The width of the Coulomb gap is defined by $g(\mu \pm \Delta) = g_c$ this gives,

$$\Delta = (g_c/\alpha_3)^{1/2}(e^2/4\pi\epsilon_0\epsilon_r)^{3/2}. \tag{2.29}$$

Figure 2.10 shows the density of states for a lightly doped semiconductor in the presence of a Coulomb gap at different degrees of compensation, the reduction in the density of states around the chemical potential is due to the Coulomb field generated by the carriers. In a graphene field effect device the chemical potential μ can be moved with the application of a gate voltage - see Chapter 4. The same analysis as for 3 dimensions can be repeated for two dimensions,

$$g_{DOS} = \alpha_2|E-\mu|(4\pi\epsilon_0\epsilon_r/e^2)^2 \tag{2.30}$$

and,

$$\Delta = (g_c/\alpha_2)(e^2/4\pi\epsilon_0\epsilon_r)^2. \tag{2.31}$$

Calculations give $\alpha_3 = 3/\pi$ and $\alpha_2 = 2/\pi$ for $E < \Delta$ irrespective of the model used. The Mott law is valid if $\Gamma > \Delta$, where Γ is the bandwidth given by eq. 2.23. In the opposite limit -i.e. $\Gamma < \Delta$ - the relation between Γ and the hopping distance R is given by $\Gamma \approx 1/R^3 D(\Gamma) \approx 1/R^3\Gamma^2$, from which,

$$\Gamma \approx 1/R \tag{2.32}$$

substituting eq. 2.32 into eq. 2.19 and maximizing in the same way as we did for the Mott formula we arrive at the formula,

$$\sigma = \sigma_0 exp(-(T_0/T)^{1/2}) \tag{2.33}$$

where,

$$T_0 = \beta_d e^2/4\pi\epsilon_0\epsilon_r\xi k_B. \tag{2.34}$$

The width of the band contributing to conduction being,

$$\Gamma(T) \approx k_B T(T_0/T)^{1/2} \tag{2.35}$$

and the optimum hopping length being,

$$R_M(T) \approx \xi(T_0/T)^{1/2}. \tag{2.36}$$

The equations for hopping conduction in the presence of Coulomb interactions are also valid in two dimensions, with $\beta_2 = 6.5$ while $\beta_3 = 2.8$ as calculated numerically [28].

The temperature smears out the Coulomb gap at energies $k_B T > \Gamma$ and therefore interaction effects are only observed when $\Gamma > k_B T$.

In disordered systems such as partially fluorinated graphene we see evidence for both Mott (MVRH) and Efros-Sklovskii (ES-VRH) for different fluorine coverage levels see chapter 4 and we use this theory to describe the temperature dependence of the resistivity.

2.5 Quantum Dots

A quantum dot is an artificially structured object which may be produced by electrostatic gates or physical size reduction of conductive structures such that the charge carriers are well localized. As a result discrete energy levels form within the dot. To observe such quantum effects, the size of the device must be reduced to sub micrometer and the temperature at which measurements are taken should be lower than the associated quantum level spacing [30, 31].

Quantum dots made from graphene are an attractive prospect for spin qubit applications as the electron spin-decoherence time in carbon materials is expected to be long [32].

Let us consider first a small metallic island surrounded by a dielectric environment. The potential ϕ follows a linear relation with the charge Q which resides on the island relative to infinity where the potential is set to zero. The factor of proportionality is known as the capacitance C of the body, $C = Q/\phi$. The associated electrostatic energy

is then simply $E = Q^2/2C$.

The associated energy scale for the transfer of a single electron to a metallic island is $E_c = e^2/C$. Therefore in order to be able to observe the addition of a single electron the charging energy E_c must be larger than the other associated energy scales, such as temperature or bias voltage for instance.

For a metallic sphere or disk the capacitance is linearly related to the diameter of the object $C \propto D$. To increase E_c we need to reduce C which can be achieved by shrinking the spatial dimension of the metallic island.

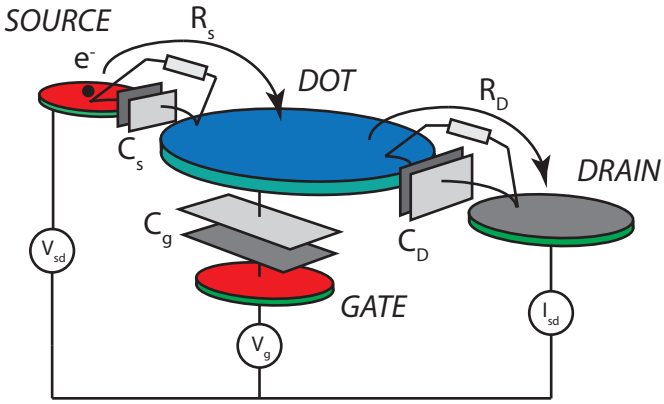

Figure 2.11: Diagram and equivalent circuit for a quantum dot, showing source and drain reservoirs connected to a conductive island by a parallel resistor and capacitor.

To probe the electron transport of the charging island one needs to contact the island with metallic leads, Figure 2.11 shows a schematic for a quantum dot system, the charging island is separated from reservoirs of electrons by capacitive and resistive links.

Due to the charging energy the tunneling of electrons can be easily suppressed at low temperatures, this phenomenon is known as Coulomb blockade. The charging energy is related to the total capacitance by the following relation,

$$E_c = e^2/C_\Sigma. \tag{2.37}$$

Where C_Σ is the sum of the capacitances $C_\Sigma = C_g + C_s + C_d$. Another important quantity is the tunnel resistance R_s, R_d which has to be large in order to observe Coulomb blockade and the minimum value for this tunnel resistance can be estimated using the uncertainty principle $\Delta E \Delta t > h$. We have $\Delta E = e^2/C_\Sigma$ and $\Delta t = R_t C_\Sigma$

which gives $R_t > h/e^2$ or ≈ 26 KΩ. In order to observe Coulomb blockade R_t must be significantly larger than h/e^2 .

Finally, if confinement effects are large enough in all three dimensions such that the electron dynamics are governed by quantum effects then the system can be called a quantum dot.

The model which describes the electron dynamics in these systems is known as the constant interaction model, which is based on three assumptions. Firstly the Coulomb interactions of the electrons on the dot and the environment are parameterized by a single capacitance C_Σ which is the sum of the capacitances in the system. The second assumption is that the single particle energy spectrum $\delta\epsilon$ is independent of the Coulomb interactions. The third assumption is that the tunnel barriers which connect the quantum dot to the source and drain reservoirs be large such that the conductance is less than $2e^2/h$, this ensures that the charge on the dot is quantized [30].

Using these assumptions the total energy of a single dot with N electrons in the ground state is given by [30],

$$U(N) = \frac{(-|e|(N - N_0) + C_S V_S + C_D V_D + C_G V_G)^2}{2C_\Sigma} + \sum_{n=1}^{N} \epsilon_n \tag{2.38}$$

here e is the electron charge, eN_0 is the charge on the quantum dot due to the positive background of the donors. V_S , V_D and V_G are the potentials applied to the source, drain and gate electrodes. The last term is the sum over single particle energy levels ϵ_n which depends on the characteristics of the confinement potential and nature of the carriers which is determined by the crystal's material properties.

The electrochemical potential of the dot $\mu(N)$ is defined as the energy required to add the Nth electron to the dot with $(N-1)$ electrons,

$$\mu(N) = U(N) - U(N-1) = (N - N_0 - 1/2)E_c - E_c/e(C_S V_S + C_D V_D + C_G V_G) + \epsilon_N \tag{2.39}$$

where $E_c = e^2/C_\Sigma$ is the charging energy. The addition energy i.e. the energy required to add an additional electron to the quantum dot is given by,

$$E_{add} = \mu(N+1) - \mu(N) = E_c + \delta\epsilon. \tag{2.40}$$

In this expression we have a classical term E_c and a quantum term $\delta\epsilon$. For instance in a system of massive carriers $\delta\epsilon \approx h^2/8mD^2$ where D is the diameter of the quantum dot and m is the effective mass of the carriers. In a graphene quantum dot (where the

carriers are massless) the quantum level spacing is $\delta\epsilon \approx v_F h/2D$ where v_F is the Fermi velocity of the charge carriers. Therefore, for a 200 nm island we have $\delta\epsilon \approx 10$ meV while a similar size GaAs island only gives $\delta\epsilon \approx 0.1$ meV at a realistic 2DES electron density. This makes graphene interesting for quantum applications where quantum behaviour exists at higher temperatures. The physics of graphene quantum dots is at the focus of chapter 5.

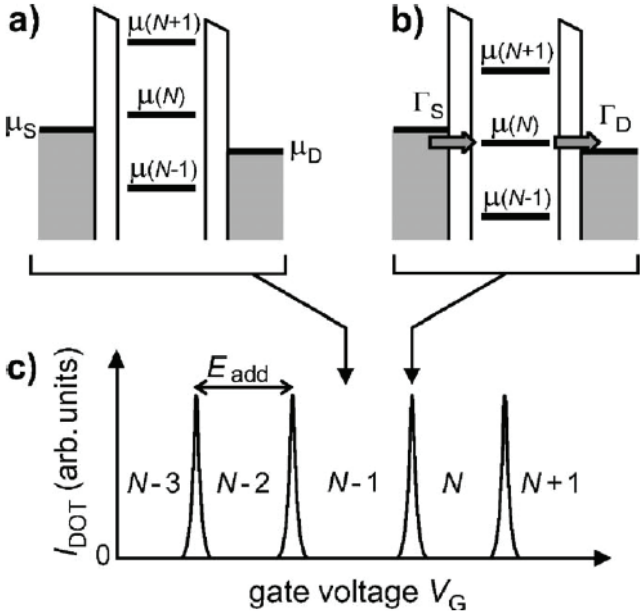

Figure 2.12: (a) Transport is blocked when no level lies between the chemical potentials of the source and drain electrodes (b) when a level is moved between the source and drain chemical potential by application of a gate voltage then current can flow through the dot. (c) Measured current through the quantum dot as a function of gate voltage. Adapted from [30]

Figure 2.12(a) shows the quantum dot energy level diagram with the source electrode at chemical potential μ_s, the drain electrode is at μ_D and the energy levels due to spatial confinement. In the zero bias regime (where the excitation voltage $eV_b < k_B T$) we require the $e(\mu_S - \mu_D) < k_B T$. The ladder of discrete levels which exists within the dot may be shifted by means of an external gate voltage. When a level exists between μ_S and μ_D, electrons can flow through the dot as shown in Figure 2.12(b). On the other hand, if the levels are outside this energy window $\mu_s - \mu_d$ the current is blocked

Figure 2.12(a). This process of conduction is known as Coulomb blockade. Figure 2.12(c) shows the current through the quantum dot as a function of gate voltage, the peaks in the current exist when a level is aligned and these conductance resonance's follow the line-shape [33],

$$G = G_0 cosh^{-2}(e\alpha_G \delta V_G / 2.5 k_B T_e) \tag{2.41}$$

where α_G is the back gate lever arm and is defined as $\alpha_G = C_g/C_\Sigma$. δV_G is the distance in V_G between successive conductance resonances and T_e is the electron temperature in the system.

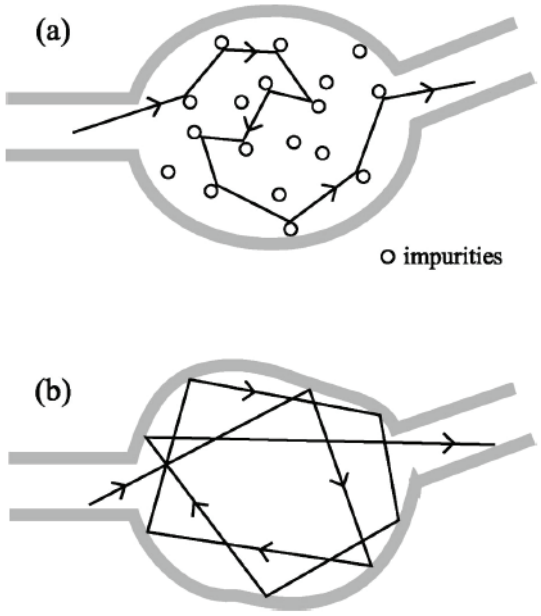

Figure 2.13: (a) A disordered quantum dot the transport here is diffusive and the electron scatters off impurities before passing to the drain electrode. (b) A ballistic quantum dot where the electron scatters off the walls of the dot and not from impurity's within the bulk of the dot. Adapted from [31].

For quantum dots consisting of just a few electrons the addition spectrum will exhibit maxima at $N = 2, 6$ and 12 corresponding to completely filled shells analogous to shells in atoms. The single-particle model plus constant charging energy as described above is in good agreement when compared to calculations of a few electron system

[31].

While calculations are feasible in small dots, they become impractical for dots with several hundred electrons as all inter-particle interactions must be taken into account. Dots with no particular geometric symmetry with large N lead to chaotic single-particle dynamics due to scattering from irregular edges or impurities. Therefore the conductance through dots of this type fluctuates randomly when various parameters are altered, this is known as the statistical regime.

Classical chaos is the exponential sensitivity of the time evolution of a dynamical system to its initial conditions and is well understood [31]. The link between classical and quantum chaos is known as the Bohigas - Giannoni - Schmit (BGS) conjecture, that the statistical quantal fluctuations of a classically chaotic system are described by random matrix theory (RMT) [34]. In RMT the only relevant information is the system's fundamental space-time symmetries. The only physical parameter is $\delta\epsilon$ the mean level spacing, and this leads to universal predictions.

Figure 2.13(a) shows a quantum dot in the diffusive regime - i.e. $l < L$ (l is the mean free path while L is quantum dots characteristic size) where the electron scatters off impurities inside the dot, the associated energy scale in this system is known as the Thouless energy, $E_t = \hbar/\tau_D$ where τ_D is the diffusion time. Figure 2.13(b) shows a ballistic dot where the electron passes from source to drain electrode without scattering. When the boundaries are irregular, the electron's dynamics are mostly chaotic. The relevant time scale in ballistic dots is the ergodic time τ_C which is roughly the time of flight across the dot. The related energy scale $E_T = \hbar/\tau_C$ which is termed the ballistic Thouless energy.

The chaotic nature of the classical motion can only be revealed if the electron scatters off the boundaries several times before escaping. For the predictions of RMT to hold we require that $\tau_{escape} > \tau_c$ - i.e. the time for the electron to escape must be longer than the ergodic time, this is only possible if the electron scatters from the boundaries. Equivalently the width of a level Γ in the dot must be small compared to E_T. For a diffusive dot a similar condition $\Gamma < E_C$ is required.

The level repulsion due to electrons inside the dot leads to statistical dynamics which are well described by (RMT) and the type of distribution describing the level fluctuations depend only on the symmetries of the system. If there is no repulsion the levels would move randomly relative to each other and so they will show a Poisson-distribution as the peak probability would occur for zero shift away from E_c [31]

$$P(S) = a \exp(-bS) \tag{2.42}$$

where S is the normalized level spacing $S = \frac{(\Delta E - E_c)}{<\delta\epsilon>}$, and the constants can be determined from the normalization conditions $< S >=< SP(S) >= 1$. For the Poisson distribution $a = b = 1$. If however we turn on repulsion in the system then the probability for zero energy shift would be small.

In fact the distributions which represent the level spacing fluctuations depend only on the symmetry of the system and they are represented by: Gaussian orthogonal (GOE), Gaussian unitary (GUE) and Gaussian symplectic (GSE) ensembles,

$$\begin{aligned} P^{GOE}(S) &= \frac{\pi}{2} S \exp\left(-\frac{\pi S^2}{4}\right), \\ P^{GUE}(S) &= \frac{32}{\pi^2} S^2 \exp\left(-\frac{4S^2}{\pi}\right), \\ P^{GSE}(S) &= \frac{2^{18}}{3^6 \pi^3} S^4 \exp\left(-\frac{64 S^2}{9\pi}\right). \end{aligned} \tag{2.43}$$

These distributions are observed when the following symmetry conditions are obeyed. For the (GOE) distribution the system must have time inversion + int. spin or time inversion + space rotation symmetry, while for the (GUE) has no time inversion symmetry and the (GSE) has only time inversion symmetry. Orthogonal, unitary and symplectic correspond to the allowed transformations [31].

Distribution function	Space time Symmetries
GOE	time inversion + int. spin **or** time inversion + space rotation
GUE	no time inversion
GSE	time inversion

The differences between the functions are not dramatic so a large ensemble is required to differentiate between the various statistics.

The quantum dot is composed of electrons - i.e. Fermions. We should therefore expect in our quantum dot a parity effect due to the number occupancy on the dot. If there is an even number of electrons then the energy cost to add an extra electron on the dot is $E_c + \delta\epsilon$ while if there is an odd number of electrons on the dot then the energy cost to add an electron onto the dot is E_c. Taking this into account the full distribution for level spacings on a quantum dot is,

$$P(S) = 1/2[\delta(S) + P^i(S)] \tag{2.44}$$

where the delta function is centred on E_C. This function is then convolved with a Gaussian function to take into account thermal broadening. Observations of this bi-modal distribution are rare and have been reported in CdSe and GaAs quantum dots with small gas parameter (The ratio of the Coulomb repulsion to the kinetic energy of an electron at the Fermi surface, $r_s = E_{e-e}/E_F$) [35, 36]. The reason that this bi-modal structure has not been observed is due to small statistical ensemble and secondly is thought to be due to large gas parameter where the electron-electron repulsion of the electrons on the dot 'scrambles' the neighbouring levels, so no bi-modal distribution will be observed. [37].

2.6 Electron transport in a perpendicular magnetic field.

2.6.1 Classical Hall effect

It may be important in some circumstances to have knowledge of the carrier concentration of the material. The Hall effect is a simple method which is used to estimate the carrier concentration. This method becomes important when characterizing heavily doped materials, for instance heavily doped graphene where the carrier concentration cannot be estimated by the gate dependence of the resistance.

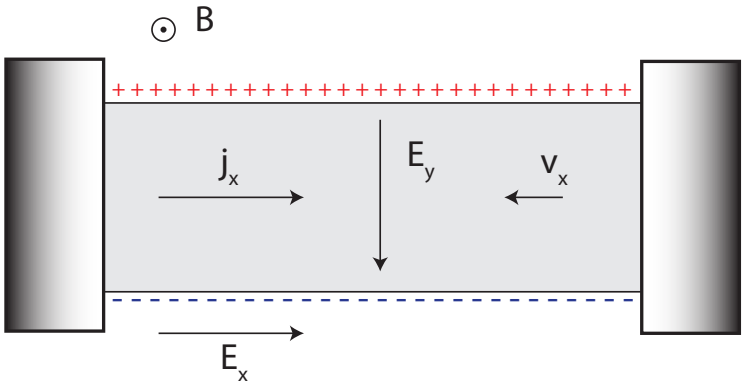

Figure 2.14: Schematic of the Hall effect.

Figure 2.14 shows a schematic for the classical Hall effect for a material which has a free electron gas with electrons traveling in the **x** direction with a current density j_x which are accelerated by an electric field E_x and have associated with them a drift velocity $-v_x$. If one applies a perpendicular magnetic field in the **z** direction, the trajec-

tory of the electrons will be bent due to the Lorentz force and electrons will accumulate on one side of the conductor while holes on the opposite side of the conductor. This charge accumulation creates an electric field E_y which will balance out the Lorentz force. The force acting on the electron is,

$$\mathbf{F} = q[\mathbf{E} + (\mathbf{v} \times \mathbf{B})]. \tag{2.45}$$

Charge will build up on opposite sides of the conductor until the forces will balance - i.e. $\mathbf{F} = 0$ then,

$$qE_y = qv_xB. \tag{2.46}$$

The Hall resistivity is defined as

$$\rho_{xy} = \frac{E_y}{j_x} = R_H B, \tag{2.47}$$

where R_H is the Hall coefficient. In eq 2.47 we have the current density in a material with a carrier concentration n with a unit electrical charge e which is expressed as,

$$j_x = -nev_x. \tag{2.48}$$

Substituting eq. 2.48 into $R_H = \frac{v_x}{j_x}$ we have an expression for the Hall coefficient in terms of the carrier concentration and charge of the electron,

$$R_H = -\frac{1}{en}. \tag{2.49}$$

This is a useful tool to determine the majority carrier concentration. Indeed the measurement of Hall resistivity should be $\rho_{xy} \propto B$ for a constant carrier concentration n.

Upon increasing the external magnetic field, charge carriers can finally traverse a cyclotron orbit without experiencing scattering. At this value of magnetic field, quantum effects play a central role as it will be apparent in the following section.

2.6.2 Shubnikov de Haas effect of the electrons in graphene.

In the previous section, it was concluded that the Hall resistivity $\rho_{xy} \propto B$. Figure 2.15 shows the longitudinal resistance and Hall resistance as a function of magnetic field for a mono-layer graphene sample. It can be seen that for low magnetic field the Hall resistance is indeed proportional to the magnetic field and the conclusions of section

2.6.1 hold.

However, experimentally it is apparent that at intermediate magnetic fields $1 < B < 2$ T oscillations occur in the longitudinal resistance. While for higher magnetic fields $B > 2$ T, plateaus develop in the Hall resistivity and these plateaus correspond to oscillations in the longitudinal resistance.

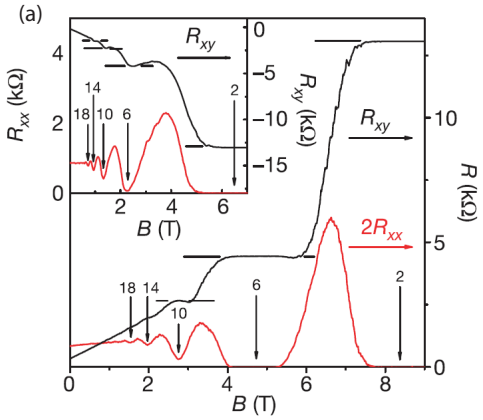

Figure 2.15: Observation of the quantum Hall effect in graphene, adapted from [38]. The red curve corresponds to the longitudinal resistance of the graphene sample as a function of magnetic field while the black curve corresponds to the Hall resistance measured using voltage probes at opposite sides of the graphene sheet.

To understand the high magnetic field behaviour of the magneto-conductance, we have to go beyond the classical Hall effect introduced in section 2.6.1 and consider the quantum nature of the charge carriers. The Lorentz force causes a bending of the trajectory of the charge carriers, which are now localized on cyclotron orbits. These orbits are quantized following the Bohr-Sommerfeld relation,

$$\oint \mathbf{p} \cdot d\mathbf{r} = (n + 1/2)2\pi h. \tag{2.50}$$

Where $\mathbf{p}$ is the momentum and n is an integer. From this assumption it can be shown that the flux Φ through the orbit is,

$$\Phi = (n + 1/2)(2\pi\hbar/e). \tag{2.51}$$

The area in real space A_n of the orbital is related to the area in k space S_n by, $A_n = (\hbar/eB^2)S_n$. The flux through one orbital $\Phi_n = BA = (\hbar/e)^2 S_n/B$ can then be

equated to eq. 2.51 to give,

$$S_n = (n + 1/2)(2\pi/\hbar)B. \tag{2.52}$$

If the magnetic field is then incremented by ΔB which is enough to give two successive orbits at levels n and $n+1$ then,

$$S_n \left(1/B_{n+1} - 1/B_n\right) = 2\pi e/\hbar. \tag{2.53}$$

This important result shows that the oscillations in longitudinal resistance with magnetic fields can be related to the area of the Fermi surface $S = \pi k_F^2$. If one has knowledge of the density of states of the material the frequency of the oscillations can then shed light on the carrier concentration of the material as discussed below for the case of graphene.

The low energy expansion of the Hamiltonian is shown in eq. 2.10, this equation can be rearranged in the presence of a magnetic field directed perpendicular to the flow of current such that the magnetic vector potential has coordinates $\mathbf{A} = (0, -B_x, 0)$,

$$\begin{pmatrix} -E_k & (-i\hbar\frac{\partial}{\partial y} - eBx + \hbar\frac{\partial}{\partial x})v_F \\ (-i\hbar\frac{\partial}{\partial y} - eBx - \hbar\frac{\partial}{\partial x})v_F & -E_k \end{pmatrix} \begin{pmatrix} h_{\Gamma_A}(x) \\ h_{\Gamma_B}(x) \end{pmatrix} exp(ik_y y) = 0 \tag{2.54}$$

substituting $\lambda = \frac{E_k l_B}{\hbar v_F}$ (where $l_B = \sqrt{\hbar/eB}$ is the magnetic length) into eq. 2.54 and writing it out as two separate linear equations,

$$\begin{aligned} \frac{\hbar v_F}{l_B}\left(-\lambda h_{\Gamma_A}(x) + \left(k_y l_B - \frac{x}{l_B}\right) h_{\Gamma_B}(x) + l_B \frac{dh_{\Gamma_B}(x)}{dx}\right) = 0 \\ \frac{\hbar v_F}{l_B}\left(-\lambda h_{\Gamma_B}(x) + \left(k_y l_B - \frac{x}{l_B}\right) h_{\Gamma_A}(x) - l_B \frac{dh_{\Gamma_A}(x)}{dx}\right) = 0 \end{aligned} \tag{2.55}$$

making the substitution $\psi = \frac{x}{l_B} - k_x l_B$ then eq. 2.55 can be simplified to,

$$\begin{aligned} -\lambda h_{\Gamma_A}(x) - \psi h_{\Gamma_B}(x) + \frac{dh_{\Gamma_B}(x)}{d\psi} = 0 \\ -\lambda h_{\Gamma_B}(x) - \psi h_{\Gamma_A}(x) - \frac{dh_{\Gamma_A}(x)}{d\psi} = 0 \end{aligned} \tag{2.56}$$

solving simultaneously eq 2.56 we arrive at the second order differential equation where we have eliminated h_{Γ_B},

$$-\frac{d^2 h_{\Gamma_A}}{d\psi^2} + \psi^2 h_{\Gamma_A} = (\lambda^2 + 1) h_{\Gamma_A} \tag{2.57}$$

The harmonic oscillator equation is,

$$-\frac{\hbar^2}{2m}\frac{d^2\xi}{dx^2} + \frac{kx^2}{2}\xi = E\xi \tag{2.58}$$

rearranging and substituting in $k = \omega^2 m$ where $\omega = eB/m$ then eq. 2.58 becomes,

$$-\frac{d^2\xi}{dx^2} + x^2\left(\frac{m^2\omega^2}{\hbar^2}\right)\xi = \frac{2mE}{\hbar^2}\xi. \tag{2.59}$$

Then making the substitution $x \to x/l_B$ and simplifying this equation becomes,

$$-\frac{d^2\xi}{d(x/l_B)^2} + (x/l_B)^2\xi = \frac{2E}{\hbar\omega}\xi \tag{2.60}$$

One can then directly compare equations 2.60 with equation 2.57 to produce the solutions for the quantized levels in graphene,

$$\lambda^2 + 1 = \frac{2E}{\hbar\omega} = 2N + 1, \tag{2.61}$$

where N = 0,1,2, ... so $\lambda = \pm\sqrt{2N}$ remembering we made the substitution $\lambda = \frac{E_k l_B}{\hbar v_F}$ so substituting back in for λ we get the quantized energy levels for graphene in a magnetic field which are known as Landau Levels,

$$E_N = \pm\frac{\hbar v_F}{l_B}\sqrt{2N} = \pm V_F\sqrt{2eB\hbar N}. \tag{2.62}$$

The Shubnikov de Haas effect is observed as the periodic oscillations of the longitudinal conductivity with inverse magnetic field, the frequency of this oscillation allows accurate determination of the carrier concentration. To obtain a expression relating the frequency in inverse magnetic field to the carrier concentration we consider two adjacent Landau levels at magnetic field B_N and B_{N+1} which coincide with the Fermi energy E_f, using eq. 2.62 this leads to two equations,

$$\begin{aligned} E_F &= v_F\sqrt{2eB_N\hbar N} \\ E_F &= v_F\sqrt{2eB_{N+1}\hbar(N+1)}. \end{aligned} \tag{2.63}$$

Rearranging both the above equations for N and solving simultaneously gives,

$$1 = \frac{\hbar k_F^2}{2e}\left(\frac{1}{1/B_{N+1} - 1/B_N}\right). \tag{2.64}$$

Finally we must consider the density of states of graphene in order to rearrange eq. 2.64 in terms of carrier concentration. The density of states is defined as the number of states per interval of energy at each energy level that are available to be occupied by electrons which is written down as simply $g(E) = dN/dE$, for graphene the density of states is therefore,

$$g(E) = \frac{2EA}{\pi(k_F)^2} \tag{2.65}$$

where A is the area and the factor 2 comes from the valley degeneracy. The density of states for graphene is linear with energy which is in contrast to conventional 2 dimensional semiconductors where the density of states is constant. Upon integrating up to the Fermi energy E_F it can be shown that the carrier concentration in graphene is related to the Fermi wavevector by $\pi n = k_F^2$, substituting this into eq. 2.64 then one arrives at,

$$n = \frac{4e}{h}\left(\frac{1}{1/B_{N+1} - 1/B_N}\right) = \frac{4e}{h} f_{SdHO} \tag{2.66}$$

where f_{SdHO} corresponds to the Shubnikov de Haas oscillation frequency. This is a very useful tool especially when characterizing an electron system with majority and minority carrier types. This characterization tool plays a crucial role in the structural determination of few layer graphene flakes intercalated with $FeCl_3$ shown in Chapter 8

Further information can be extracted from the amplitude decay of the Shubnikov de Haas oscillations with increasing temperature. Thermal activation of carriers at higher temperatures lead to a washing out of the oscillations at higher temperatures. The temperature dependence of the amplitude decay of the oscillations follows the expression,

$$A(T) = \frac{T}{sinh\left(2\pi^2 k_B T m_c/eB\right)} \tag{2.67}$$

where A is the amplitude of the oscillation, T is the temperature of the system and m_c is the cyclotron mass. This equation was derived for massive electrons by [39] and interestingly it is also found to be valid for electrons in graphene [38]. This expression

allows one to extract the cyclotron mass of the carriers in a material by fitting eq. 2.67 with the free variable m_c. It allows us to distinguish between massless carriers of mono-layer graphene and massive carriers of bi-layer graphene in intercalated 5-layer graphene, where electron transport takes place though parallel bi-layer and monolayer electron systems, see Chapter 8.

Chapter 3

Experimental Techniques.

3.1 Graphene Characterisation

3.1.1 Optical contrast

Interestingly graphene which is a single atomic layer of carbon atoms absorbs a striking amount of electromagnetic radiation and shows universal absorbance of $\pi\alpha \approx 2.293$ % (where α is the fine structure constant), or equivalently a universal optical conductance of $\sigma = \pi G_0/4$ (where $G_0 = 2e^2/h$ [40] is the quantum of conductance). This is illustrated in Figure 3.1 which shows that the measured absorbance and sheet conductivity do not depend on the photon energy due to the absence of a band gap in graphene [41].

Figure 3.2 shows the measured wavelength dependence of the optical contrast of graphene placed on a conventional Si^{++} (inf) / SiO_2 (275 nm) substrate for up to 5 layers. The peak in the optical contrast shown in in Figure 3.2 sits at ≈ 525 nm or green light. This maximum of the optical contrast occurs due to interference effects in the SiO_2 cavity and can be explained simply by the application of the Frenel equations [42]. Therefore selecting a green filter when identifying graphene flakes enhances the observed contrast. Optical contrast provides an accurate method for identifying graphene flakes up to 3L thick, for accurate identification of graphene flakes for more than 4L, we need to make use of Raman spectroscopy.

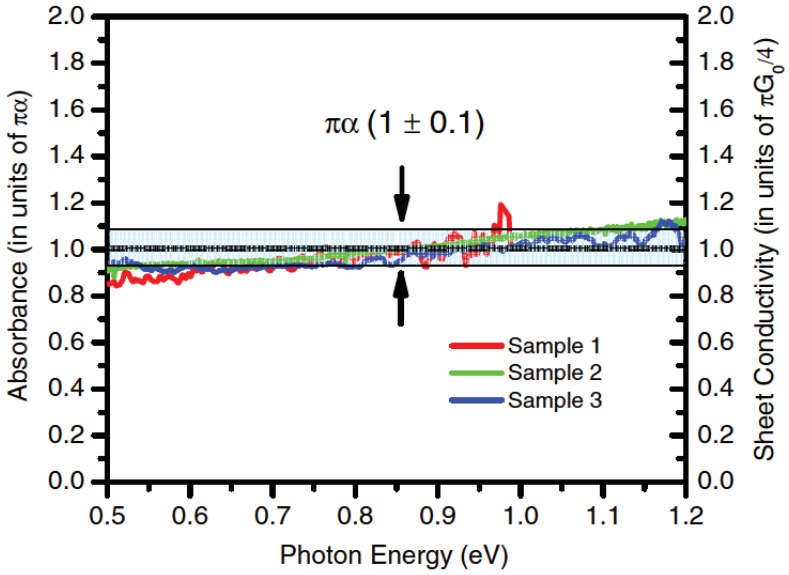

Figure 3.1: Universal optical conductivity of graphene for three separate mono layer graphene samples. Adapted from [40]

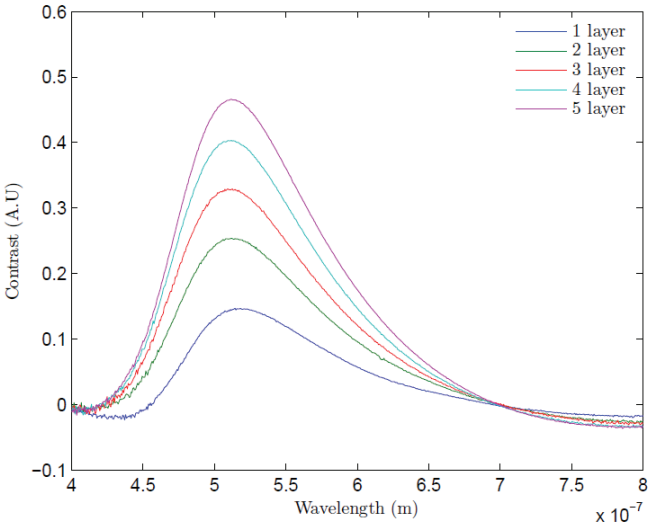

Figure 3.2: Measured optical contrast for graphene layers up to 5 on Si/SiO_2.

3.1.2 Raman Spectroscopy

Raman spectroscopy is a useful non invasive tool used to characterize graphene and can provide information such as layer number determination, doping level and disorder level. Below is a short introduction to the principles of Raman spectroscopy of graphene.

When light is irradiated onto graphene it excites electrons into the conduction band. The excited electron then scatters off a phonon before recombining to emit a photon of lower energy. The reduction in energy of the emitted photon from the incident photon is a measure of the particular phonon energy, expressed in units of wavenumber ν cm^{-1} which can be converted into phonon energy $hc\nu$ J .

Therefore, Raman spectroscopy grants easy access to the phonon spectrum of a material. For the case of graphene the unit cell of graphene consists of two atoms one of sub-lattice A and one of sub-lattice B as such there exists 6 phonon branches, in which three acoustic (A) and three optical (O). For one acoustic branch (A) and one optic (O) phonon branch, the atomic vibrations are perpendicular to the atomic plane and they correspond to the out of plane phonon modes (o). For the two acoustic and two optic phonon branches , the vibrations are in-plane (i). The directions of the phonon modes are considered relative to the nearest carbon-carbon atoms and are therefore classified as the longitudinal (L) transverse (T). Therefore, along the high symmetry directions ΓM and ΓK, the six phonon dispersion curves are assigned to LO, iTO, oTO, LA, iTA and oTA phonon modes, Figure 3.3(a).

Figure 3.3(b) shows the Raman processes responsible for the characteristic Raman spectrum shown in Figure 3.3(c).

The most prominent feature of the Raman spectrum are the G (1580 cm^{-1}) and G'(2D) (2700 cm^{-1}) bands and if the sample is defected - i.e. due to missing atoms or other short range impurities such as sp^3 bonded carbon - a D band is seen at (1350 $\mathrm{cm}^{-}1$).

The G - band is associated with doubly degenerate (iTO and LO) phonon mode at the Brillouin zone center. This is the only band originated by a normal first order Raman process, while the G'(2D) comes from either a doubly resonant Raman process with an iTO phonon or a triply resonant process.

The D and the D' bands do not exist in pristine graphene, instead to activate this band a defect is required. The band originates from a phonon at the K point of the BZ. In order to observe the D band, an interaction with a defect must occur, the excited electron can then be scattered off a defect elastically in order to recombine [43].

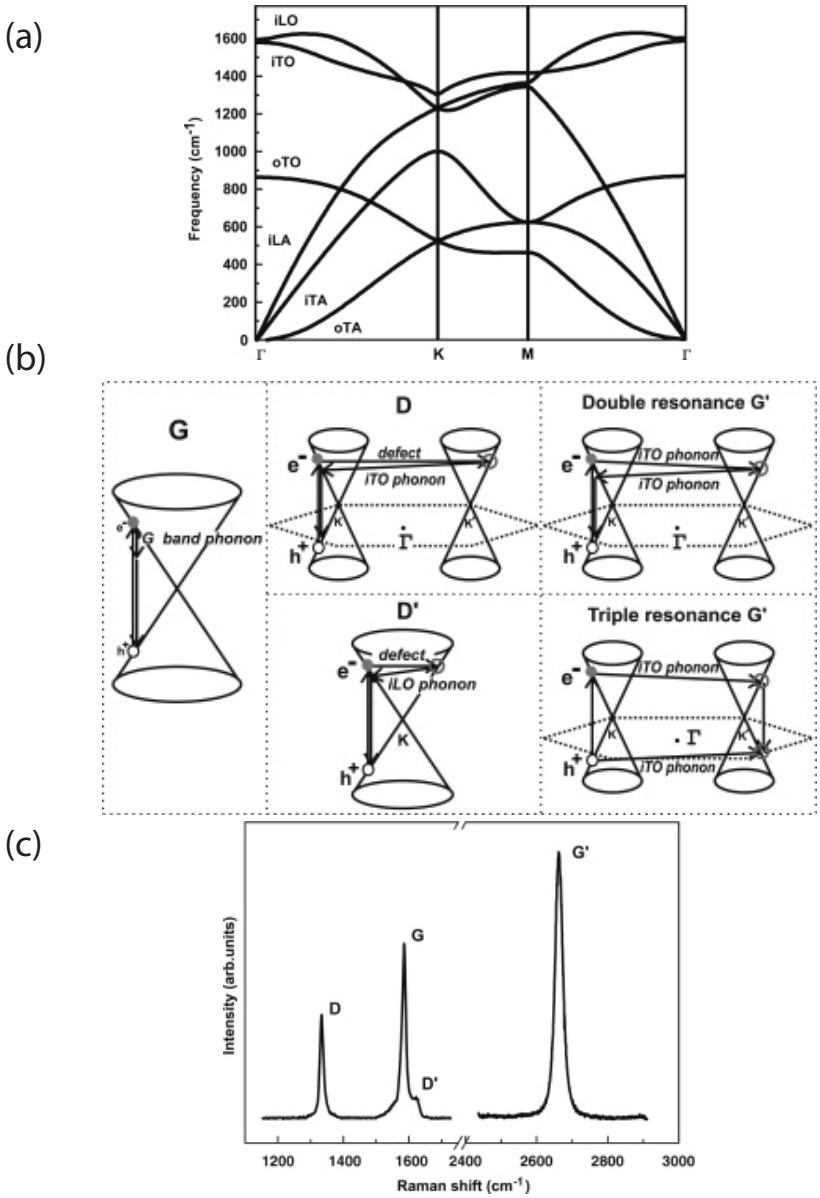

Figure 3.3: (a) Phonon spectrum of graphene. (b) (left) First order G - band process and (centre) one - phonon second order DR process for the D - band (Inter-valley) (top) and for the D' process (Intra-valley) (bottom). (Right) two-phonon second order resonance Raman spectral process (top) and for double resonance (G' or 2D), and (bottom) for the triple resonance (G' or 2D) band process (TR) for mono-layer graphene. (c) Typical Raman spectrum for a graphene sample with disorder such that the D - resonance is activated. Adapted from [43]

3.1.2.1 Layer number Determination

Interestingly one can use Raman spectroscopy to determine more accurately the number of layers present in a graphene sample by using the ratio of the integrated intensity of the G-band to the integrated intensity of the Si-band of the substrate. Intuitively this is obvious as the more graphene there is the more signal one gets from sp^2 bonded carbon atoms while the amount of light that gets to the silicon is reduced. Therefore with increasing the numbers of layers, a reduction of the intensity of the silicon peak and an increase of the intensity of G peak are observed [44] see Figure 3.4.

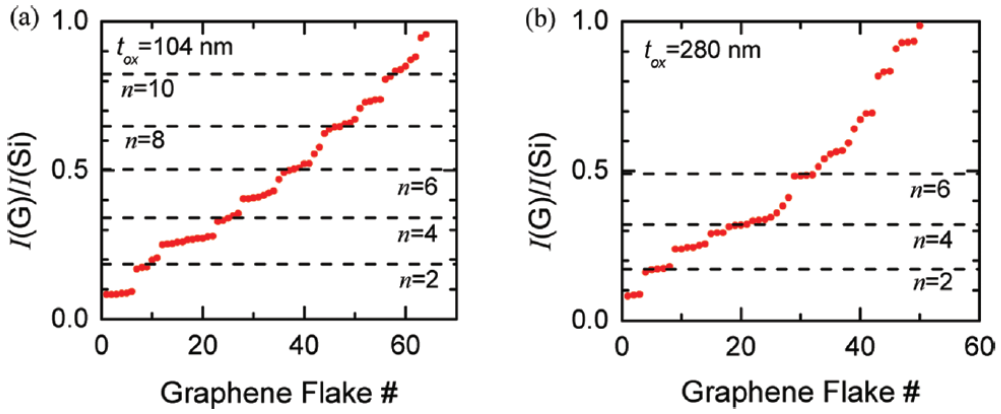

Figure 3.4: (a) Ratio of the integrated intensity of the G to the Si peak in multi-layer graphene for a large ensemble of flakes for t_{ox} = 104 nm and (b) for 280 nm. Adapted from [44]

3.1.2.2 Defect Level

Raman spectroscopy can be used to identify the level of disorder in a graphene flake, this is particularly important when characterizing partially fluorinated graphene. Upon fluorination we introduce a certain level of disorder or short range defects in the form of sp^3 bonded carbon, which behaves similarly to defects such as missing carbon atoms caused by ion bombardment. These defects give rise to the D-band as discussed above. The ratio of the integrated intensity of the D band to that of the G band gives information on the size of the defect radius [45].

Figure 3.5(a-d) shows the development of the Raman spectrum for mono-layer graphene irradiated to 5 different levels of ion-bombardment which correspond to 5 different inter defect distance L_D. The ratio of the integrated intensity for these samples is plotted in Figure 3.5(e) with the solid lines being fits to the following equation [45],

$$\frac{I_D}{I_G} = C_A \frac{(r_A^2 - r_S^2)}{(r_A^2 - 2r_S^2)} [e^{-\pi r_S^2/L_D^2} - e^{-\pi(r_A^2 - r_S^2)/L_D^2}] \tag{3.1}$$

Where r_A and r_S in eq 3.1 are length scales that determine the region where the D band scattering takes place. More precisely r_S determines the radius of the structurally disordered region caused by the ion bombardment and r_A is defined as the radius of the area surrounding the point defect in which the D band scattering takes place. Extracted values for r_S and r_A are 1 nm and 3.1 nm. From this information we can determine the inter defect distance and it will be used in in Chapter 4.

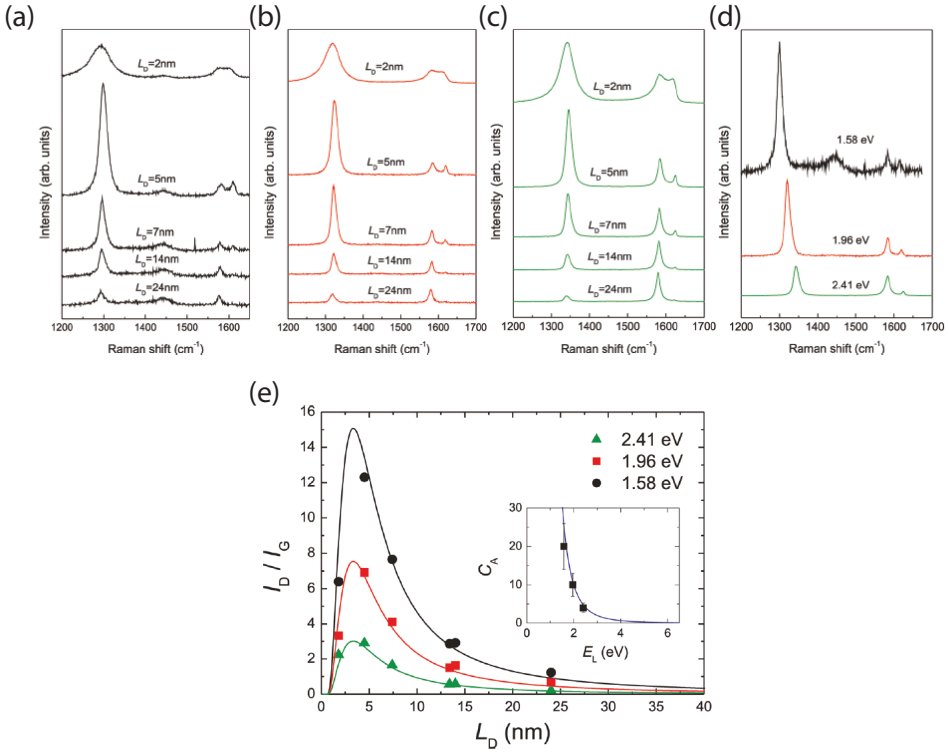

Figure 3.5: (a-c) Raman spectra for an ion-bombarded graphene flake at 3 different lase energies. (d) Raman spectra for L_D = 7 nm obtained using three different laser energies.(e) I_D/I_G vs L_D for all single layer samples. Adapted from [45]

3.1.2.3 Doping Level

Finally Raman spectroscopy is also valuable when identifying the doping level in graphene materials. This can be done by monitoring the position of the G-peak in graphene. In the undoped state the G-peak lies at 1585 cm^{-1} wavenumber. Upon doping its energy up shifts -this is also known as 'stiffening' of the Raman mode [46]. Figure 3.6 shows the shift of the G-mode for varying degrees of doping achieved by means of a gate in this system. It can be seen that both electron and hole doping lead to an energy up shift of the Raman G-peak. However for electron doping levels $> 10^{14}$ cm^{-2} strong non-adiabatic effects become important and a strong softening of the Raman G - peak is seen [47].

The stiffening of the G-peak is a useful tool to characterize few-layer intercalated graphene as it will be shown in Chapter 8.

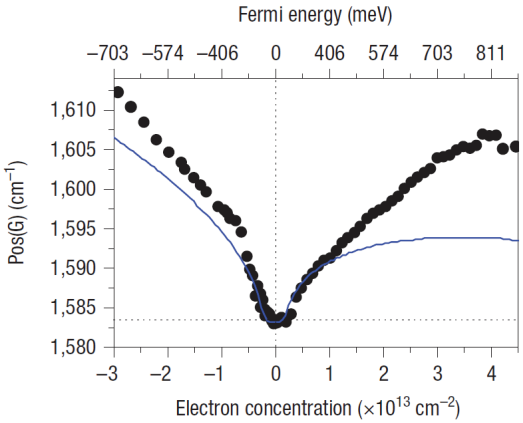

Figure 3.6: Shows the position of the G-peak in graphene as a function of doping level. Adapted from [46]

3.2 Graphene transistor

The chemical potential in graphene can be shifted by the application of an electric field, which allows for the possibility of varying the carrier concentration in graphene. This electric field is experimentally easy to control when embedding graphene in a transistor structure with graphene placed on a thin dielectric (e.g. native SiO_2) separating a metallic plate (See Appendix for detailed description of graphene device preparation).

Typically the silicon wafers that are used in our experiments are heavily p-doped silicon coated by a 300nm thick SiO2 layer. We have then a plane plate capacitor, with the capacitance being, $C = Q/V_g$ where $Q = Ne$ (N is the total electrons in the graphene sheet and V_g is the voltage applied to the p-doped silicon with respect to the graphene flake.

This gives,

$$n[cm^{-2}] = c_g V_g. \tag{3.2}$$

Using the parallel plate capacitance relation $c_g = C/A = \epsilon_r \epsilon_0 / de$ where d is the oxide thickness, ϵ_r is the relative permittivity of the SiO_2 ($\epsilon_r = 3.9$) and ϵ_0 is the permittivity of free space. From this it can be shown that the carrier concentration on the flake is related to the gate voltage V_g by,

$$n[cm^{-2}] = 7.19 \times 10^{10} \cdot V_g. \tag{3.3}$$

The density of states for graphene is $dN/dE = g(E) = 2E/\pi\hbar^2 v_F^2$ where $v_F \approx 10^6$ ms^{-1} is the Fermi velocity. This relation can be integrated up to the Fermi level and rearranged for E_F to give,

$$E_F = 31 \cdot \sqrt{(V_g)}[meV]. \tag{3.4}$$

For accurate carrier concentration determination the gate voltage must be correlated with Shubnikov de Haas measurements as discussed in Section 2.6.2.

Chapter 4

Electron properties of fluorinated graphene transistors.

4.1 Abstract

We have fabricated transistor structures using fluorinated single-layer graphene flakes and studied their electronic properties at different temperatures. Compared with pristine graphene, fluorinated graphene has a very large and strongly temperature dependent resistance in the electro-neutrality region. We show that fluorination creates a mobility gap in graphene's spectrum where electron transport takes place via localized electron states, furthermore by tuning the fluorine coverage it was found that there is a transition from Mott variable range hopping (VRH) to Efros-Sklovskii (VRH) where electron - electron interaction creates a Coulomb gap in the density of states.

4.2 Introduction

In this first experimental chapter we have succeeded in fabricating transistor structures with fluorinated graphene mono-layers and studied their transport properties at temperatures from 4.2 to 300 K. Fluorinated graphene flakes were separated by mechanical exfoliation [26] from fluorinated graphite with fluorine contents between 24% and 100%. They are then processed into transistor structures which have shown a strong increase

The results in this Chapter have been published as F. Withers, M. Dubois and A. K. Savchenko, *Phys. Rev. B* **82**, 073403 (2010) and F. Withers, S. Russo, M. Dubois and M. F. Craciun, *Nanoscale Res. Lett.* **6**, 526 (2011).

of the resistance in the electro-neutrality region, caused by the opening of a mobility gap in the graphene spectrum.

4.3 Experimental details

4.3.1 Device fabrication

There are two main ways to produce fluorinated graphite [20, 48–50]. In the first graphite is heated in the presence of F_2 to temperatures in excess of 300°C, so that covalent C-F bonds are formed and modify the carbon hybridisation. The layered structure of graphite is then transformed into a three-dimensional arrangement of carbon atoms. In the second, graphite is exposed to a fluorinating agent, XeF_2, and the process is performed at a temperature lower than 120°C as XeF_2 easily decomposes on the graphite surface into atomic fluorine. Due to its reactivity and diffusion, the fluorination results in a homogeneous dispersion of fluorine atoms that become covalently bonded to carbon atoms [49, 51]. At low fluorine content (F/C atomic ratio ≤ 0.4), conjugated C-C double bonds in the non-fluorinated parts and covalent C-F bonds in corrugated fluorocarbon regions coexist [50, 52], with the concentration of the covalent bonds increasing with concentration of fluorine.

In this work we use both methods of fluorination of the original graphite material. We first considered fully fluorinated HOPG graphite $(CF)_n$ as a starting material. The flakes are mechanically exfoliated from the fluorinated graphite onto conventional Si/SiO_2(275nm) substrates. The produced flakes are noticeably smaller ($\sim 1\mu$m in size) than the flakes fabricated by the same method from non-fluorinated graphite. They contain more than 10 mono-layers. After optical identification the flakes are electrically contacted into transistor structures by electron beam lithography followed by the evaporation of 5 nm Crome (Cr) followed by 50 nm of Gold (Au).

4.3.2 Raman spectroscopy

The many-layer exfoliated flakes were first characterised by Raman spectroscopy using excitation light with a wavelength of 532 nm and a spot size of 1.5 μm in diameter. An incident power of $\sim$5 mW was used. We ensured that this power does not damage the graphene by performing Raman measurements on a similarly sized pristine graphene flake which shows the common spectra of mechanically exfoliated graphene: the G and 2D bands at 1580 cm^{-1} and 2700 cm^{-1}, see Figure 4.1(a).

In fully fluorinated graphene, a D-peak appears at 1350 cm^{-1} and its intensity is

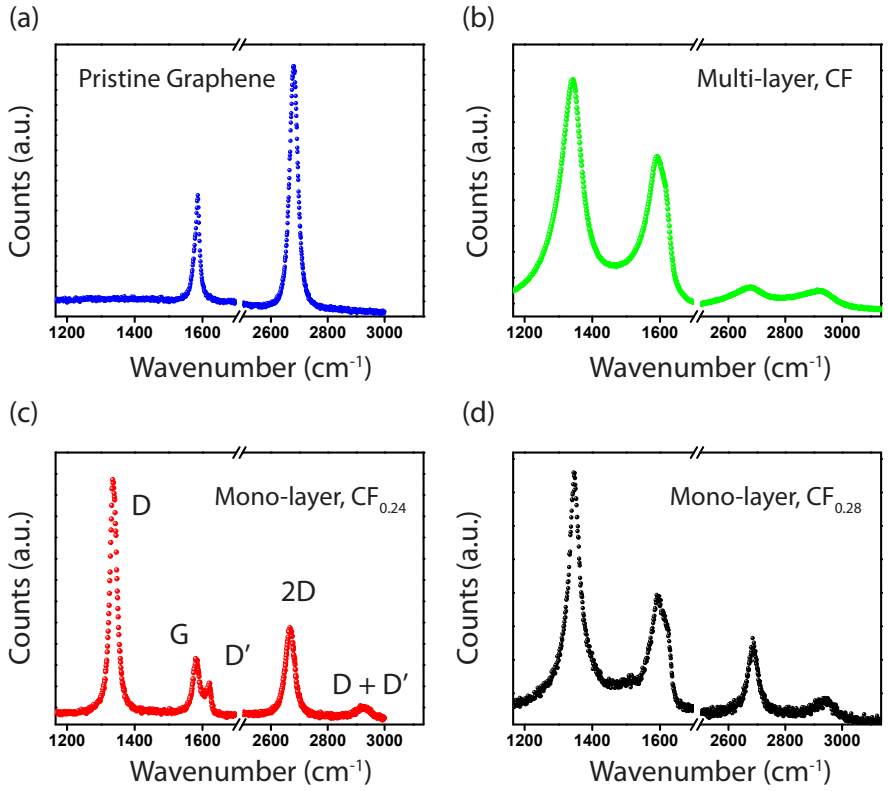

Figure 4.1: Raman spectra for (a) pristine graphene, (b) multi-layer fully fluorinated multi-layer graphene, (c) fluorinated graphene mono-layer exfoliated from $CF_{0.24}$ and (d) fluorinated graphene mono-layer exfoliated from $CF_{0.28}$.

larger than that of the G and 2D peaks, see Figure 4.1(b). As the D resonance requires a defect for its activation, its presence is associated with an increased degree of disorder [53–55]. Various defects can contribute to the D-peak, such as bond dislocations, missing atoms at the edges of the sample and sp^3 hybridized carbon atoms. Previous studies demonstrated that the intensity of the D-peak produced from the edges of a graphene flake is relatively small compared to the G peak [56]. Our experiments consistently show that the D-peak of pristine graphene flakes with similar size as fully fluorinated graphene is below the resolution of the measurement, see Figure 4.1(a). This suggests that the edges of the fully fluorinated flakes give minimal contribution to the D-peak in Figure 4.1(b). Furthermore, structural studies [20] of the bulk fully fluorinated graphite material show that the defects are sp^3 bonded carbon atoms and not bond dislocations. Therefore, we expect the main contribution to the D-peak of

fully fluorinated graphene to come from sp^3 bonded carbon atoms. Electrical transport measurements were taken in either 2 - terminal or 4 - terminal configuration in either constant voltage or constant current regime. The voltage drop across the sample was carefully varied in order to prevent electron overheating - i.e. $V_b < k_B T/e$.

4.4 Results

4.4.1 Properties of flakes exfoliated from (CF)

Several transistor structures have been fabricated (See section 3.2 and Appendix). All the studied devices show very large resistance (more that 1 TΩ) and no gate-voltage control of the resistance, typical of a wide band gap semiconductor material. Recent works [27, 57] have shown that the I/V characteristics of fully fluorinated graphene are strongly non-linear with a nearly gate independent resistance value higher than 1 GΩ, suggesting the presence of a band gap. The purpose of this work is to produce transistor structures with a large on/off ratio of the current. To this end, we reduced the fluorine content by annealing the samples at $\sim$ 300°C in a 10% atmosphere of H_2/Ar for 2 hrs. The resistance is decreased and a partial gate-voltage control is achieved, Figure 4.2(a). The annealing, however, has not noticeably changed the Raman spectrum in Figure 4.1(b).

Resistance measurements of the fully fluorinated flakes after annealing show a strong temperature dependence, Figure 4.2(a). To examine the presence of the energy gap, we analyzed $\rho(T)$ at the highest gate voltage V_g =50 V, (which is still far from the Dirac point) by an exponential law describing thermal activation of carriers across the energy gap $\Delta\epsilon$: $\rho = \rho_0 \exp(\Delta\epsilon/2k_B T)$, Figure 4.2(b). The resulting value of $\Delta\epsilon$ found at high temperatures is only ∼25 meV, which is significantly smaller than the expected energy gap for fully fluorinated graphene. It is also seen that the slope of $\ln \rho(1/T)$ dependence decreases with decreasing T, which is a signature of hopping conduction via localized states [28]. The fact that in the whole range of studied temperatures electron transport is not due to thermal activation across the gap but due to hopping, has been confirmed by re-analyzing the temperature dependence in terms of two-dimensional hopping: $\rho(T) = \rho_0 \exp\left((T_0/T)^{1/3}\right)$, where $k_B T_0 = 13.6/a^2 g(\mu)$, g is the density of localized states at the Fermi level μ and a is the localization length [28]. The results are found to be in good agreement with this expression, Figure 4.2(b), with the value of T_0 =20000 K. This confirms that the previously found activation energy of 25 meV is not the activation energy $\Delta\epsilon$ that separates the localized states from extended states

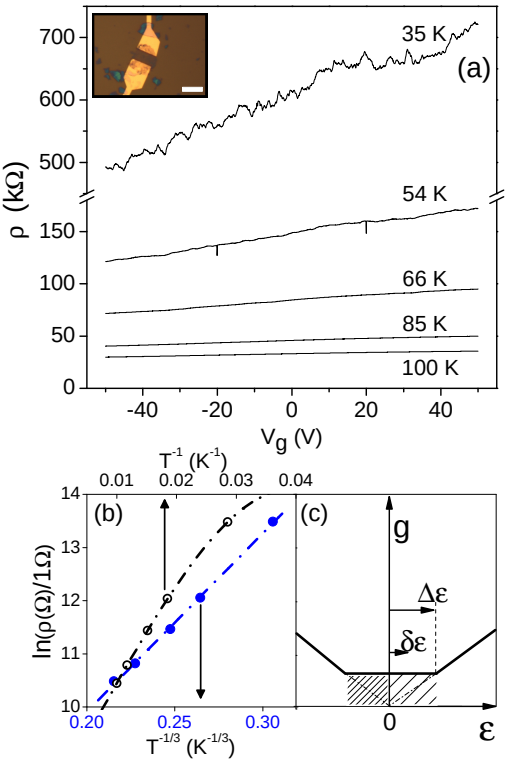

Figure 4.2: (a) Resistivity as a function of gate voltage for a fully fluorinated device. Inset: Optical image of the device (scale bar is 1 μm). (b) Resistivity plotted against T^{-1} and $T^{-1/3}$ at V$_g$=+50 V. (c) A diagram of the energy dependence of the density of electron states, with the Fermi level at zero energy and localized states shown by the shaded area. (Dense shading shows occupied localized states.)

at the mobility edge, but is an activation energy $\delta\epsilon$ of hopping between localized states within the mobility gap, Figure 4.2(c). Although not measured, the value of $\Delta\epsilon$ in these samples seems to be larger than that in hydrogenated graphene, as the obtained value of T_0 is ∼100 times larger than in [19], indicating a smaller density of localized states and smaller localization length.

4.4.2 Properties of flakes exfoliated from ($CF_{0.24}$)

To achieve good V_g-control of fluorinated graphene transistors, one needs to fabricate mono-layer flakes. To do this, we have used the second method of fluorination, by gaseous XeF_2. The mixture of natural graphite and XeF_2 was prepared in a glove box in

an Ar atmosphere. The reactor was then kept at 120°C for 48 hrs, which gave a fluorine content of 24% as measured by mass uptake. Mechanical exfoliation of the partially fluorinated graphite is carried out under ambient conditions. Flakes are located using an optical microscope and mono-layer flakes with an optical contrast of $\sim 5-7\%$ in green light were selected for processing into transistor structures. (We noticed that the contrast of fluorinated mono-layers is $\sim 2\%$ lower than that of pristine graphene on Si/SiO_2(275nm) substrates). The flakes were confirmed to be mono-layer by Raman spectroscopy. The 2D peak which is well fitted by a single Lorentzian function, and has a FWHM in the region of 20-30 cm^{-1} is typical for pristine mono-layer graphene [53].

The Raman spectrum of partially fluorinated mono-layer graphene, Figure 4.1(c), shows much narrower D, G and 2D peaks compared with thicker layers made from fully fluorinated graphite, Figure 4.1(b). This made it possible to detect additional features in the Raman spectrum that also arise in hydrogenated graphene [19]: the D' peak at ≈ 1620 cm^{-1}, which also requires a defect for its activation, and a combination mode $(D + D')$ at ≈ 2950 cm^{-1}. It is interesting to note that in our fluorinated graphene the ratio of the integrated intensities $I_D/I_G = 3.8$ by using eq. 3.1 [45] we estimate the inter-defect distance of $L_D \approx 5.3$ nm, which we note is larger than that found in partially (on one side) hydrogenated sample, and is comparable to that in the samples hydrogenated on both sides [19]. This can be the result of the fact that in the mono-layer flakes fabricated by exfoliation from fluorinated (intercalated) graphite the probability of fluorination is equal for both sides of the plane.

Figure 4.3(a) shows the resistance as a function of gate voltage measured for a range of temperatures. Due to the small size of the samples, $\sim 4\mu m^2$ in area, the resistance shows strong mesoscopic fluctuations [58], and thus the $R(V_g)$ dependences were smoothed for the subsequent analysis using a moving average filter.

The curves in Figure 4.3(a) have been offset along the V_g-axis to account for doping, which is detected as a shift of the maximum resistance (the Dirac point) from $V_g = 0$. The partially fluorinated samples were found to be doped to $V_g = +10$ V ($n = 0.74 \times 10^{12}$ cm^{-2}). This level of doping is similar to that seen in conventional (pristine) graphene devices, which we attribute to doping by atmospheric water. Unlike pristine graphene devices with very weak temperature dependence of the resistance, in the range of $V_g = \pm 20$ V around the Dirac point the resistivity of fluorinated samples is seen to grow by two orders of magnitude as T decreases from 300 K to 4.2 K. Outside this region the temperature dependence remains weak, with the mobility of carriers ~ 150 $cm^2V^{-1}s^{-1}$.

We analyze the temperature dependence of the resistance in terms of the activation law described in section 2.3, $\rho = \rho_0 \exp(\Delta\epsilon/2k_BT)$, showing that it is not applicable

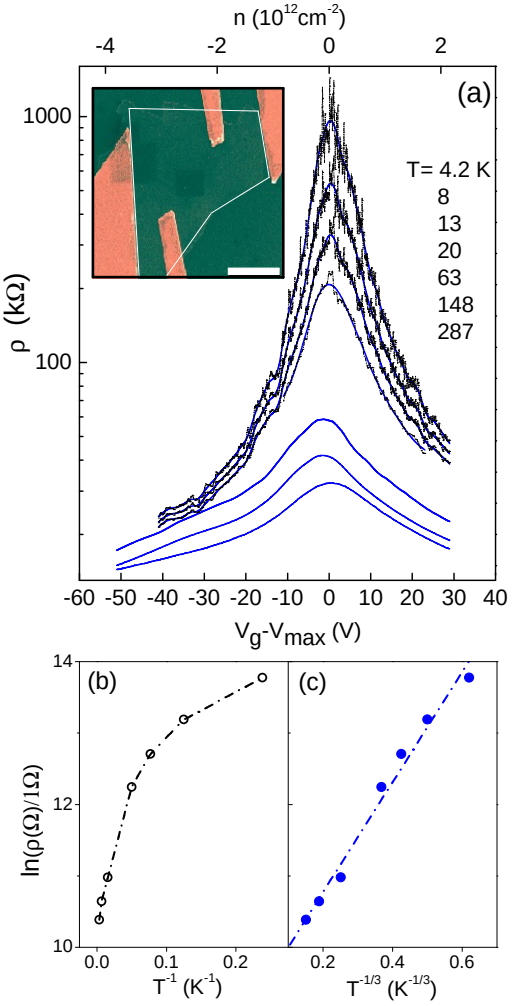

Figure 4.3: (a) Resistivity of fluorinated mono-layer graphene as a function of gate voltage. Inset: false color SEM image of the mono-layer device (scale bar is 1 μm). Resistivity in the Dirac region plotted as a function of (b) T^{-1} and (c) $T^{-1/3}$.

for the whole temperature range and at high temperatures gives an activation energy of $\sim$ 7 meV at the neutrality point. Similarly to the fully fluorinated layers, the resistivity $\rho(T)$ is fitted well by variable range hopping theory described in section 2.4, $\rho(T) = \rho_0 \exp\left((T_0/T)^{1/3}\right)$, Figure 4.3(c). Figure 1.4 shows the hopping parameter T_0 as a function of carrier concentration. The value of T_0 approaches zero at a carrier concentration of $\pm 1.2 \times 10^{12}$ cm^{-2}. This value gives the concentration of the localized electron states in the energy range from $\epsilon = 0$ to the mobility edge. The mobility edge

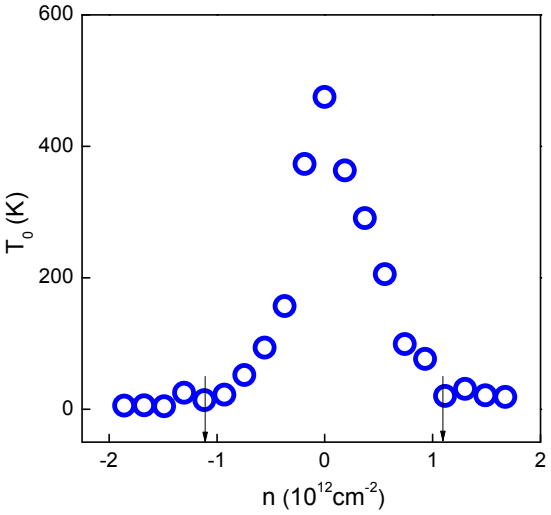

Figure 4.4: The value of the hopping parameter T_0 as a function of the carrier density. Arrows indicate the concentration at which T_0 approaches zero and the conduction becomes metallic.

occurs at $V_g \simeq \pm 20$ V and indicates the transition from hopping to metallic conduction, Figure 4.2(c).

In order to relate the obtained concentration of the localized states to the energy gap $\Delta\epsilon$, one needs to know the exact energy dependence of the density of states in the gap. For estimations, we will use the linear relation for the density of extended states above the mobility edge, $g(\epsilon) = 2\varepsilon/\pi\hbar^2 v^2$ ($v = 10^6$ ms^{-1} is the Fermi velocity) and a constant value for the density of localized states below the mobility edge, Figure 4.2(c). This gives an estimation $\Delta\epsilon \sim 60$ meV and twice this value for the full mobility gap. In this approximation the density of the localized states in the gap is estimated as 10^{36} J^{-1}m^{-2}. Using the obtained value of the hopping parameter T_0 ~500 K in the Dirac point, one can then estimate the localization length at $\epsilon = 0$ as $a \sim 40$ nm.

The presence of localized states in the electro-neutrality region is clearly the result of disorder, due to the random positions of F atoms on graphene in the partial fluorination. The current experiment does not allow us to establish whether these states exist in the band gap produced by fluorination, or are simply the result of a 'smearing' of the linear density of states of graphene (as sketched in Figure 4.2(c)). Taking into account the relatively small value of the parameter T_0 and large localization radius a, it seems that

the latter case is most probable and there is no large band gap created in the spectrum. For future applications, however, it is only an increase of the resistance in the electro-neutrality region which matters, and this is achieved in both scenarios of creation of the mobility gap. Our results show that in order to achieve large resistances in graphene transistors at room temperature, future efforts should be aimed at decreasing the density of localized states in the mobility gap and decreasing the localization length, which can be done by partial fluorination with the fluorine content in the range between our studied values of 24% and 100%.

4.4.3 Properties of flakes exfoliated from ($CF_{0.28}$)

To this end we exfoliated mono-layer flakes from $CF_{0.28}$ material which is produced via the same method at the $CF_{0.24}$ flakes. Figure 4.5 shows the electron transport data for a typical sample fabricated from this material.

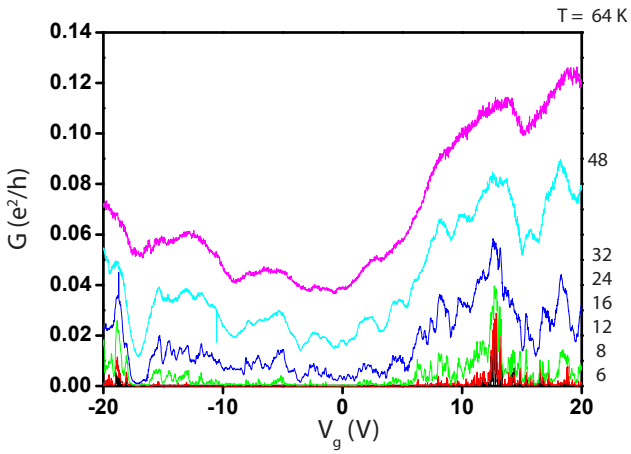

Figure 4.5: Back gate dependence of the conductance for several different temperatures, a clear transport gap at low temperatures can be seen where conductance resonances can be seen. This is an indication of charging behaviour within the flakes.

Figure 4.6 shows a high resolution measurement of the temperature dependence used for further analysis. Unlike partially fluorinated flakes which exhibit Mott (VRH), a good agreement with Efros-Sklovskii variable range hopping (ES-VRH) is seen. In this scenario a coulomb gap is opened in the density of states due to coulomb repusion. The conductance follows the relation $G \propto exp(-(T_0/T)^{1/2})$ which can be seen by the linear fit shown in Figure 4.6(b). The value of T_0 can be extracted and is found to be 410 K. T_0 is related to the localization radius through the following relation

$T_0 = 6.5e^2/4\pi\epsilon_0\epsilon_r\xi k_B$. The value for the localization is then $\xi \approx 106\pm7$ nm using and $\epsilon_r \approx (\epsilon_{SiO_2} + 1)/2 \approx 2.5$ - i.e. the average of the local dielectrics above and below the flake. The Raman spectrum for the flake is shown in Figure 4.1(d) and exhibits the same features as seen in the $CF_{0.24}$ flakes. The inter-defect size can again be extracted and is found to be $L_D \approx 2$ nm (See [45]). The flake has spacial dimensions of L ≈ 2 μm and width W ≈ 1 μ m which is much larger than the localization size, thus the flake can be thought of as consisting of an array of charging islands - ie. sp^2 regions isolated by insulating fluorinated sp^3 hybridized carbon.

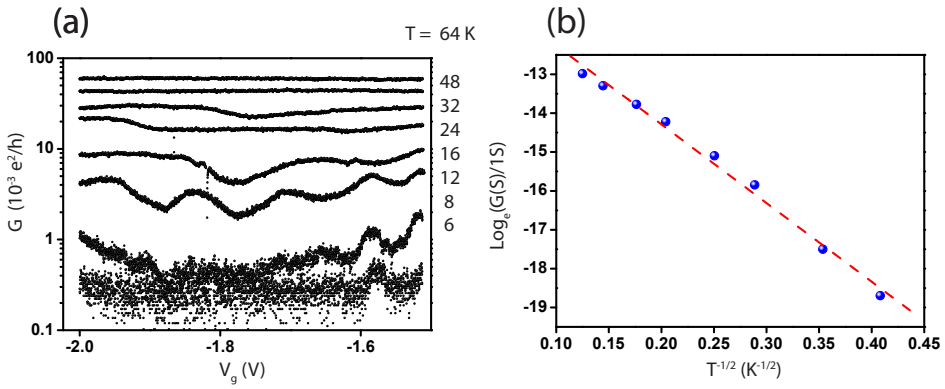

Figure 4.6: (a) Shows a higher resolution measurement of the conductance for the same sample shown in Figure 4.5 (b) The average conductance over this gate voltage range plotted in terms of Efros sklovskii Variable range hopping (ES-VRH)

4.5 Conclusion

In conclusion, the possibility of fabricating a transistor structure using fluorinated mono-layer graphene has been demonstrated. Fluorination has been shown to cause a significant increase of the resistance in the electro-neutrality region, which is a consequence of the creation of the mobility gap in the electron spectrum where electron transport is through localized states. For flakes exfoliated from $CF_{0.24}$ fluorinated using a fluorinating agent XeF_2 the electron transport can be described by Mott variable range hopping while when one increases the fluorine coverage to 28 % the electron transport is best described by ES-VRH, where the flake can be thought of as consisting of an array of charging islands. For a correlation between defects probed by Raman spectroscopy and electrical transport a greater ensemble of devices is required to draw

any conclusions. This is due to the variation of the fluorine coverage of micron sized flakes exfoliated from bulk fluorinated graphite. The following chapter will be dedicated to the isolation of smaller partially fluorinated flakes exfoliated from natural graphite fluorinated to 28 % with fluorinating agent XeF_2, with the hope to probe a single charging island.

Chapter 5

Level spacing statistics of a graphene quantum dot enclosed within fluorinated graphene.

5.1 Introduction

As described in section 2.5 due to the nature of these relativistic Dirac electrons and the absence of a band gap in graphene one cannot switch off the current and confine electrons by means of an electrostatic gate [59]. A promising route to open up a band gap in graphene and confine electrons is through chemical functionalization with fluorine, and this indeed leads to a stable wide band semiconductor [57, 60–63]. Alternatively one may etch nanostructures such as graphene nanoribbons and quantum dots in graphene using a plasma. These systems have an energy gap due to spacial localization of the electron wave function and may be used in future integrated electronics [64–68]. Interestingly graphene nanostructures are promising for use as components in future quantum computing devices, due to the large quantum level spacing $\delta\epsilon \approx h v_F/2D$ [64].

This experimental chapter is dedicated to the investigation of the spectral statistics of the nearest neighbour conductance peak separations (NNS) of a graphene quantum dot enclosed within insulating fluorinated graphene and compare this with predictions of Random Matrix theory (RMT)[31] and with recent numerical calculations for graphene quantum dots[69, 70]. Our quantum dot device differs from conventional graphene quantum dots in that the boundaries or edges are terminated by fluorinated graphene instead of etched graphene. Interestingly, unlike in conventionally etched graphene quantum dots, here we show an impressive number of conductance resonances (> 1000)

which constitutes the largest statistical ensemble of NNS for a quantum dot in the quantum chaotic regime [31].

5.2 Methods

Graphene quantum dots insulated by fluorinated graphene are prepared by micromechanical cleavage of partially fluorinated graphite (28 %) onto SiO_2 (275 nm) / Si^{++} substrates. The heavily doped silicon acts as a gate which is modulated to change the occupancy on the dot. In Chapter 4 it was shown that charging effects play an important role in the electron transport through partially fluorinated graphene and that the system can be thought of as an array of conductive charging islands isolated by fluorinated regions of graphene. The challenge here is to reduce the number of charging islands to one and to study Coulomb blockade effects. To this end we select small flakes (0.5 - 1 μm). This enables us to probe only a few quantum dots or even a single quantum dot which can be confirmed by the stability diagram (see section 2.5).

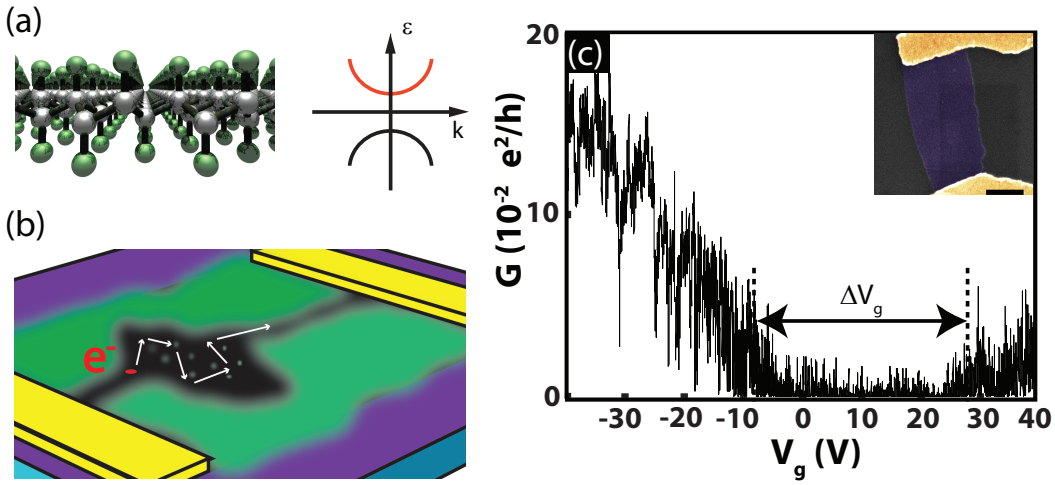

Figure 5.1: (a) Crystal structure of fluorinated graphene (green = fluorine, black = carbon) along with a band diagram for a wide band semiconductor typical for fluorinated graphene. (b) Possible configuration of the graphene dot enclosed within fluorinated graphene. (c) differential conductance vs back gate voltage taken at T = 2 K with an excitation voltage of 125 μV (Inset : false color SEM image of the device. scale bar is 500 nm).

Figure 5.1(a) and (b) shows the crystalline structure for fluorinated graphene and how the graphene quantum dot is realized within the fluorinated graphene. Given the random nature of the fluorination process we still expect the interior of the graphene dot to be 'peppered' with fluorine ad-atoms [16, 17, 20].

Figure 5.1(c) shows the 2 terminal differential conductance measured at 2 K at B = 0 T with an excitation voltage of 125 μV. The dependence is typical for graphene quantum dot and nanoribbon devices where localized resonances within a transport gap are seen [65, 66]. The transport gap exists in the back gate range from -10 to 25 V, within this gap exists a large number of conductance resonances are clearly visible.

5.3 Results

The observed conductance peaks are due to the Coulomb blockade effect discussed in Chapter 2.5 and occur when the ladder of discrete energy levels are shifted by the gate voltage, with respect to the chemical potential of the source electrode. When these levels pass between the chemical potential of the source and drain contacts the resonant transport occurs [31]. The energy difference between adjacent peaks is known as the nearest neighbour level spacing (NNS) and is defined as,

$$\Delta E = E_c + \delta\epsilon.$$

Where E_c is the charging energy and is a classical term which depends on the sum of the capacitances of the system in the following way, $E_c = e^2/2C_\Sigma$ as was introduced in section 2.5. $\delta\epsilon$ is the quantum level spacing energy and is approximated to $\delta\epsilon \approx (0.2 - 1)/D$ eV $\cdot$ nm for Dirac Fermions in a disk size D [64]. This large level spacing energy enables one to resolve the quantum level spacing energy at much higher temperatures and for much larger quantum dots than any previous massive electron system, this makes graphene an ideal system for testing the predictions of Random Matrix Theory (RMT) [31].

Figure 5.2(a) shows the temperature evolution of a few conductance resonances at T = 4 K. The conductance resonances transform into Coulomb oscillations which occur when the capacitance between the source and drain becomes negligible compared to the back gate capacitance. From T = 6 K measurement shown in Figure 5.2(a) (dark blue) the separation of adjacent peaks will yield the back gate capacitance $C_g \approx e/ < \delta V_g > \approx$ 3.08 aF. Therefore, using the standard Disk-Plate capacitance relation $C_{bg} = \pi\epsilon_{SiO_2}\epsilon_0 D^2/4a$ where a is the thickness of silicon dioxide and D is the diameter of

the graphene quantum dot we obtain $D = 183$ nm. The Coulomb oscillations disappear at T $\approx$ 15 K which corresponds to the charging energy of the quantum dot $E_c \approx 1.3$ meV so the total capacitance $C_\Sigma = 62$ aF yields a back gate lever arm $\alpha_{bg} = 0.05$ [64, 71].

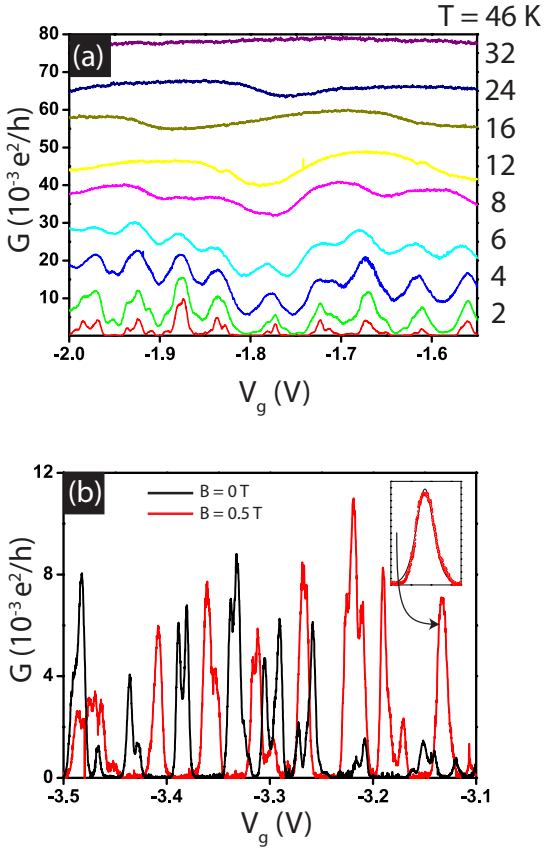

Figure 5.2: (a) Temperature dependence of the conductance peaks for a region of V_g (b) Conductance resonances for a region of gate voltage for B = 0 T and B = 0.5 T, note the double peak structure of the resonances).

Figure 5.2(b) shows a close-up of some conductance resonances for B = 0 T and B = 0.5 T. In general, we find that the conductance resonance fits well to the well known line shape [33],

$$G = G_0 cosh^{-2}(e\alpha_{bg}\delta V_{bg}/2.5k_B T_e),$$

using $\alpha_{bg} = 0.05$ we obtain an electron temperature of $T_e = 2.2$ K, which is close to the bath temperature $T_b = 2$ K.

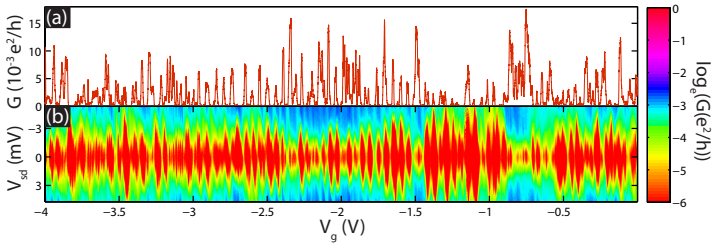

Figure 5.3: (a) Conductance resonances for a region of V_g measured at T = 2 K with an excitation voltage of 125 μV (b) Stability diagram for the same region of V_g

Figure 5.3(a) shows Coulomb blockade resonances for a wide range V_g and Figure 5.3(b) shows a color plot of the differential conductance as a function of V_g and excitation voltage V_{sd}, the height in V_{sd} of the Coulomb diamonds yields the charging energy for the quantum dot. We find the mean peak height is consistent with the estimate from the temperature dependence of the conductance resonances. The Coulomb diamonds are shown to be symmetric which implies that the capacitance of the source and drain are equivalent [30].

Inside the transport gap exists a large number of conductance resonances, we focus on the hole side of the transport gap between -9 V and 8 V. Conductance resonances were analyzed by fitting each peak to ascertain the position of the mid-point. In this region we obtain 1400, 1425, 1260, 1080 resonances for B = 0, 0.5, 2 and 6 T. The shifts were converted to energy scale using [30],

$$\Delta E = \alpha_g \Delta V_g [eV].$$

Random matrix theory (see section 2.5) predicts that the level spacing fluctuations should follow one of the following distributions, which are based on the symmetries of the system [31],

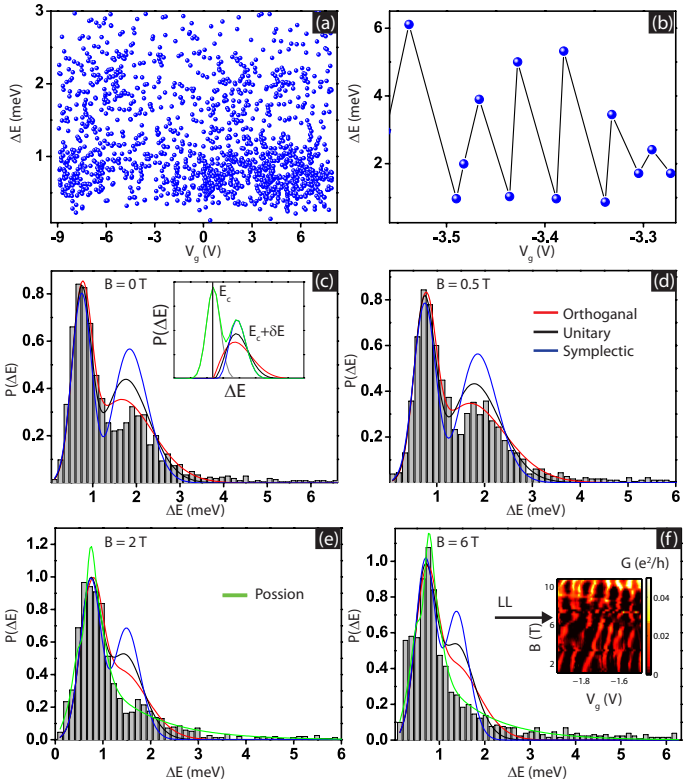

Figure 5.4: (a) Raw level separation data extracted from B = 0 T by fitting all peaks. (b) Oscillatory behavior of the level spacing separations. (c-f) Level spacing histograms for B = 0...6 T (Inset: magnetoconductance of the Coulomb peaks as a function of magnetic field. Note at B > 6 T Fock-Darwin like patterns develop due to the quantization of the electron orbits within the dot.)

$$P(S)^{GOE} = (\pi/2)Sexp(-\pi/4S^2),$$

$$P(S)^{GUE} = (32/pi^2)S^2exp(-4/\pi S^2),$$

$$P(S)^{GSE} = (2^{18}/3^6\pi^3)S^4 exp(-64/9\pi S^2).$$

GOE has time inversion, internal spin and spacial rotation symmetry, GUE has no time inversion symmetry and GSE has only time inversion symmetry, see Chapter 2.5. It has been shown numerically that as the level of disorder (either edge or internal) is increased from zero the spectral statistics transform from Poissonian (where there is no level repulsion) to orthogonal and ensembles with additional symmetries are not required [69, 70]. So for a clean graphene dot the statistics should follow,

$$P(S)^P = exp(-S)$$

where $S = (\Delta E - E_c)/ < \delta\epsilon >$. Figure 5.4(a) shows the scatter of level spacing plotted against the investigated back gate range. It is apparent that there are two regions of high density of points *region 1*, $0.2 < \Delta E < 1.0$ meV and *region 2*, $1.2 < \Delta E < 6$ meV. A fit of the scatter with a straight line gives information about the change in capacitance and therefore the shape deformation of the island with changing gate voltage [72], we find that $d(\Delta V_{bg})/dV_{bg} \approx 10^{-4}$ which is a change of 1 mV over a 10 V range. This value is small when compared to the average level spacing in gate voltage $< V_g > \approx 20$ mV.

Figure 5.4(b) highlights the observed oscillatory fluctuations. Finally, Figure 5.4(c-d) show the bi-modal level spacing. The data can be understood in terms of the bi-modal Wigner Dyson distributions predicted by random matrix theory (RMT) [31, 36, 37] in the spin resolved case. The first peak represents the thermally broadened E_c and is represented by a Gaussian function, while the second peak represents the fluctuating level spacings described by one of the above equations which depend on the symmetry of the system. Another interpretation of the double peak could be assigned to a double quantum dot, where transport can pass through each of the two dots leading to smaller spacings which are an artifact of the double dot structure. Although this is unlikely as it would require two dots of the same charging energy with their levels shifted by $\delta\epsilon$ for this to occur, we cannot rule this out currently. The data in Figure 5.4(c-f) are fitted by the following equation,

$$P(S) = 1/2(\delta(S) + P^i(S)))$$

this is then convoluted with a Gaussian function of variance σ to take into account the fluctuations of the charging energy and also errors which exist in determining

the exact midpoint of each fitted peak. The data is normalized so that $< S >=< SP(S) >= 1$. The only fitting parameters remaining are E_c, $\delta\epsilon$ and σ [35, 36].

For B = 0 T and 0.5 T a best fit for the distribution is achieved for the orthogonal distribution with $E_c = 0.8$ meV for B = 0 T and 0.5 T, while $\sigma = 0.22$ and $\delta\epsilon = 1.15$ meV for B = 0 T and $\delta\epsilon = 1.19$ meV for B = 0.5 T so between 0 T and 0.5 T no significant change in the level spacing statistics has occurred. This is surprising as the flux required to break time reversal symmetry $B^* = h/(2e\pi D^2) = 20$ mT so one would expect a transition from the orthogonal distribution to the unitary distribution which has no time inversion symmetry.

It is observed that as the magnetic field is increased from 0 T to 6 T a transition of the quantum level spacing distribution from (GOE) to a Poisson distribution occurs. For instance the B = 2 T best fit is achieved for a (P) although a small shoulder at 2 meV is still visible. This shoulder cannot be accurately fit with (GOE) assuming that half the probability is assigned to the fluctuating level spacings. The best fit parameters for the Poissonian are $E_c = 0.75$ meV $\sigma = 0.26$ and $< \delta\epsilon > = 1.10$ meV for B = 2 T. For the case of B = 6 T the best fit is achieved again for a Poissonian distribution with best fit parameters $E_c = 0.75$ meV $\sigma = 0.26$ and $< \delta\epsilon > = 1.07$ meV.

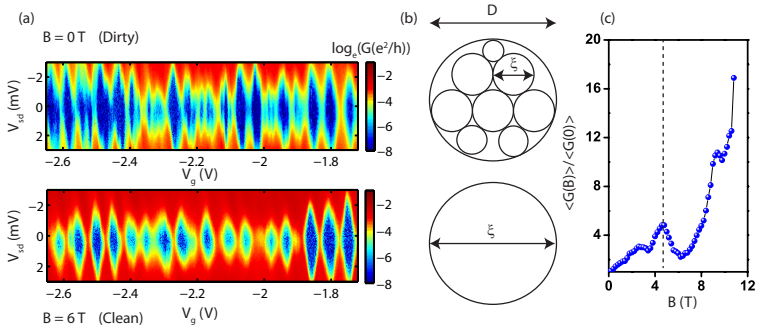

Figure 5.5: (a) Stability diagrams for a zoomed in region of V_g for B = 0 T and B = 6 T. (b) Cartoon of how the electron wavefunction is localized in each case. (c) The average magneto conductance of the Coulomb oscillations.

The fact that we see only a small change in the value of the charging energy leads us to conclude that the capacitance of the system does not change with magnetic field up to 6 T.

In summary we observe a clear bimodal shape of the distribution at zero magnetic

field which gradually evolves into a Poissonian distribution. A bimodal distribution is expected for systems with a small interaction parameter $r_s < 1$ [37], where the gas parameter is defined as the ratio of the Coulomb interaction of two electrons separated by an average distance to its Fermi energy -i.e. $r_s = E_{e-e}/E_F$ [31, 36, 72–74]. For a graphene quantum dot one expects a density independent interaction parameter of $r_s \approx 0.88$ which is less than unity. Therefore under these conditions theory predicts that a parity effect should be observed [37].

The second main observation is the transition of the best fit of the distribution from (GOE) at zero magnetic field to Poissonian at strong magnetic fields (6 T). We explain this as a change of the localization length ξ in the dot with magnetic field. Adatoms on graphene cause localized electrons and this can lead to an effect known as strong localisation, where two paths of an electron interfere destructively [28]. This interference condition can be destroyed by the application of a magnetic field. This effect is seen in much larger graphene flakes with disorder due to adatoms, and this destructive interference condition can be destroyed by application of a magnetic field. This is seen as a strong positive magneto-conductance which saturates when ϕ_0 passes through ξ. Lightly fluorinated graphene flakes have been shown to have localization radii of a few tens of nm, which is much smaller than our dot size [57, 60].

At B = 0 T the electrons are fully localized. The effect of the magnetic field is to increase the localization length until the electron wavefunction is delocalized across the size of the dot. To investigate this further we study the mean magnetoconductance of the Coulomb peaks and we find the positive magnetoconductance to saturate at 4.5 T which corresponds to a localization radius of $\xi \approx 20$ nm consistent with the value obtained in larger partially fluorinated graphene samples [57, 60]. Figure 5.5(a) shows a zoomed in region of the stability diagram for B = 0 T and B = 6 T. It can be seen that diamonds are much sharper at B = 6 T consistent with a reduction in the level of disorder felt by the electrons.

Numerical simulations of the spectral statistics reveal that in a perfectly clean graphene quantum dot one should expect a Poissonian distribution while for increased edge or internal disorder one expects a transition to (GOE). At magnetic fields larger than 6 T we see patterns in the conductance peaks which have recently been argued to be due to LL formation inside the dot [71]. Figure 5.5(c) also shows a marked increase in the magnetoconductance above B = 6 T. This can be explained by a change in capacitance of the leads to the quantum dot which is seen as a reduction of the charging energy and an increase of the conductance peak height due to less scattering of the electrons within the dot at the on resonance positions. This is confirmed from

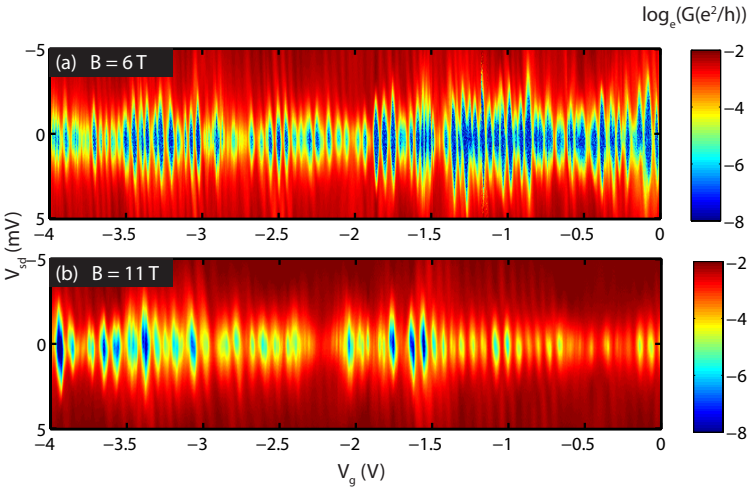

Figure 5.6: (a) Stability diagrams for a zoomed in region of V_g for B = 6 T and (b) B = 11 T

stability diagram measurements at 11 T shown in Figure 5.6 which confirms the height in V_{sd} is clearly lower than for B = 6 T and B = 0 T.

5.4 Conclusion

In conclusion we study the electron transport through a graphene quantum dot structure enclosed within fluorinated graphene. These quantum dots show Coulomb blockade over a large range of V_g with over 1000 resonances observed. The nearest neighbour level spacing distribution is clearly bi-modal which can be explained in terms of the spin resolved constant interaction model. The statistics of the quantum level spacings are best fit with the (GOE) distribution at B = 0 T and this distribution gradually changes into a Poissonian distribution at B = 6 T, which we argue is due to a tuning of the localization radius with magnetic field. More samples need to be measured before arriving at a final conclusion on these results, effects such as internal disorder on the level spacing as well as studies on parallel double dots need to be ruled out before finalizing this project.

Chapter 6

Nanopatterning of fluorinated graphene.

6.1 Introduction

As discussed in Chapter 1 the development of flexible and transparent electronic devices relies on the availability of two types of material systems: semiconducting materials for the fabrication of active areas and highly conducting materials for use in electrical wirings [75, 76]. Although organic molecules are promising semiconducting systems [77, 78], their intrinsic low carrier mobility and the large voltages usually required to operate organic devices severely limit their utility for high-speed and low-power applications [79]. Flexible conductors have been developed using metallic microwires [80] and carbon nanotubes [81], however these materials have usually limited optical transparency. Therefore, the demands for greater miniaturization, higher speed, lower power use, all embedded in a transparent device truly require novel materials.

In this experimental chapter we demonstrate a promising way towards all-graphene-electronics by using fluorinated graphene as an insulating host material. We show that we can selectively reduce fluorinated-graphene by electron beam irradiation and create conducting and semiconducting structures, which can be used as future electrical wirings and active device elements respectively. We find experimentally that the relative decrease in resistance per square upon electron-irradiation of micro-structures is at

The results in this Chapter have been published as F. Withers, T. H. Bointon, M. Dubois, S. Russo and M. F. Craciun, *Nano Lett.,* **11**, 3912 (2011)

least seven orders of magnitude (from $1T\Omega$ to $100K\Omega$) -3 orders of magnitude more conductive than what was previously reported in reduced graphene oxide patterning experiments [82]. Further we demonstrate the nano-patterning of ribbons as narrow as 40nm which exhibit a transport gap in the source-drain bias voltage whose size is inversely proportional to the ribbon width. In this gap, electrons are localized, and charge transport is dominated by variable range hopping in the presence of Coulomb-interactions. The demonstrated electron beam irradiation technology that we use to pattern nano-channels is easily scaled up to wafer size and it constitutes a step forward to all-graphene-electronics.

6.2 Experimental details

The fluorination process of graphene is conducted prior to nanofabrication, by exposing natural graphite to F_2 atmosphere at 450°C, resulting in a fluorine content of 28% as measured by mass uptake [20]. Subsequently, as detailed in section 4.3.1 few-layer fluorinated graphene flakes are obtained by mechanical cleavage of fluorinated graphite onto SiO_2 (300nm)/p-doped Si substrate which acts as a back gate. The flakes are then identified by their low optical contrast, typically $2\% - 4\%$. Electrical contacts are fabricated by standard electron beam lithography, evaporation of Cr/Au (5 nm/70 nm) and subsequent lift-off process (see the insets of Figure 6.1).

To investigate the effects of electron beam irradiation on the resistivity of fluorinated graphene we conducted an *in situ* electrical characterization in the scanning electron microscope vacuum chamber ($<10^{-5}$ mbar) by means of an electrical feedthrough. This set-up preserves the flakes from any contamination by uncontrolled atmospheric dopant which can further modify the resistivity of our devices. An incident electron energy of 10 keV and current of 0.13 nA was selected as it does not affect significantly the electronic transport properties of pristine few-layer graphene. Figure 6.2 shows the electrical transport and Raman spectroscopy for irradiated pristine few layer graphene, the disorder effects from e-beam irradiation saturate around a few mC, this is thought to be due to chemical functionalisation of the graphene with hydrogen and hydrocarbons [83]. During the electron beam irradiation, all the electrical contacts and the back gate were connected to ground.

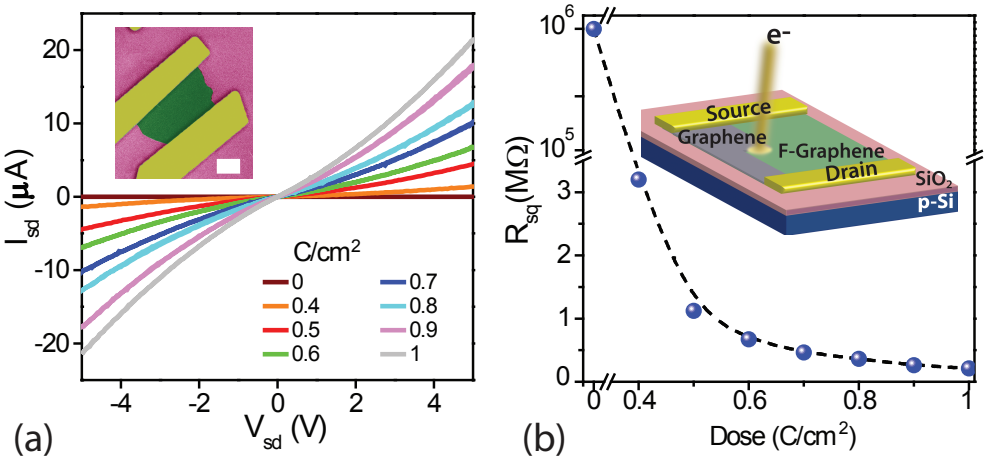

Figure 6.1: The plot in (a) shows IV characteristics for the fluorinated graphene device reported in the inset after different electron beam irradiation doses. Inset: false color SEM image of a typical fluorinated graphene device, the white bar corresponds to $1\mu m$. The green area corresponds to the fluorinated graphene flake, whereas the yellow parts are the Au/Cr electrodes. (b) shows the measured sample resistance per square plotted against the electron irradiation dose (the dashed black lines is a guideline for the eyes). The inset shows an illustration of the device configuration under irradiation with a beam of electrons.

6.3 Results

Figure 6.1(a) shows the evolution of the DC source-drain current *versus* voltage characteristics for a fluorinated graphene device after a uniform electron beam irradiation of all the flake area up to a dose of 1 Ccm^{-2}. It is apparent that for low doses the source-drain IV characteristics are largely non-linear with decreasing non-linearity for higher doses. A plot of the resistance per square (R_{sq}) as a function of dose (see 6.1b) summarizes the experimental finding that electron beam irradiation decreases monotonically the resistivity of fluorinated graphene, up to 7 orders of magnitude from $1T\Omega$ down to 100 kΩ.

To test the suitability of electron beam irradiation for patterning applications, we have performed a scaling experiment of the resistance versus width (W) of the conductive channel. We irradiate in subsequent steps neighbouring strips of 100 nm width

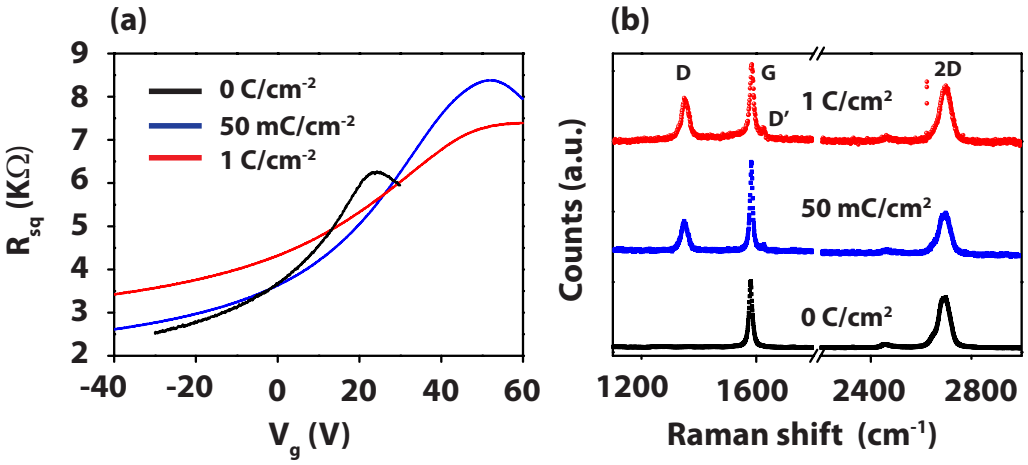

Figure 6.2: (a) Shows the gate dependence of the resistivity for a bi-layer graphene device irradiated up to 1 Ccm^{-2}. (b) shows the Raman spectrum for the same bi-layer graphene device irradiated up to 1 Ccm^{-2}.

(device type a) or 500 nm width (device type b) and 1 μm length, with a dose of 1Ccm^{-2}. 6.3(a) shows representative IV characteristics measured *in situ* after the progressive increase of the channel width for device (a). The resistance of the fluorinated graphene clearly decreases with increasing the number of exposed strips following a $1/W$ dependence, for both devices type (a) and (b) (see 6.3(b)). These experimental findings demonstrate that irradiation opens up a conductive channel in the otherwise insulating fluorinated graphene host. Therefore, electron-irradiation is well suited for patterning conductive structures on both submicron and micron scale.

Figure 6.5 shows a topographical atomic force microscopy measurement of neighbouring irradiated and non-irradiated fluorinated graphene regions. It is apparent that the electron irradiation does not cause any structural damage to the graphene material (see Figure 6.5 (b)). However, we find a significant change in height between the irradiated and non-irradiated regions. The height of the exposed region is 0.7nm lower than the height of the unexposed region, with the latter equal to 2.4 nm measured from the SiO_2 (see Figure 6.5(a)). The experimentally observed reduction in height has to be expected for electron irradiation assisted defluorination process. Indeed, previous experiments based on temperature-assisted defluorination [57], demonstrated that the interatomic layer spacing between atomically flat sp_2 graphene layers is smaller than the spacing between the three-dimensional atomic layers of sp_3 hybridized fluorinated

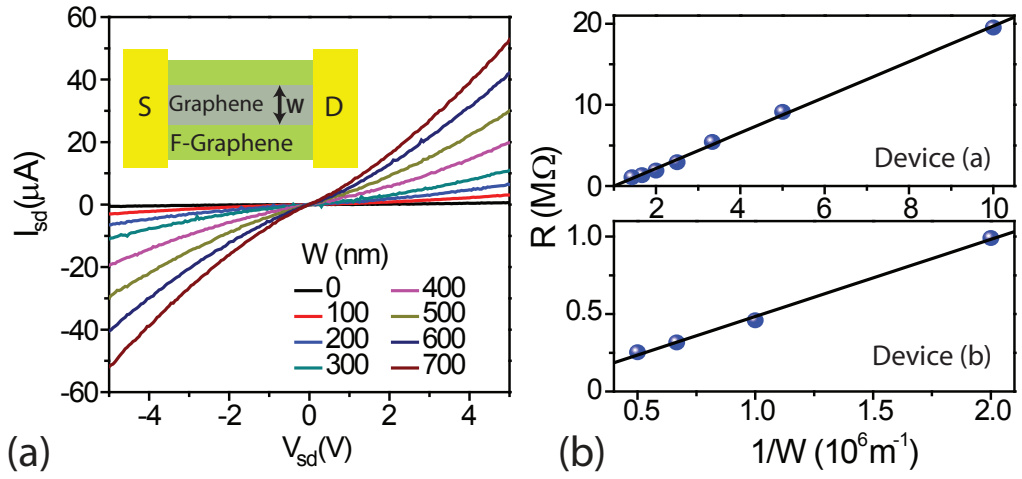

Figure 6.3: (a) IV characteristics for channels of different widths W patterned in fluorinated graphene. Graphs in (b) show the sample resistance plotted against inverse width W for 2 devices types (see main text). The solid lines represent linear fits to the experimental data points (blue).

graphene [20]. The defluorination process is also consistent with the increase in the optical contrast that we observed on all the electron irradiated fluorinated graphene samples. Indeed, the closing of the large energy gap of fluorinated graphene is expected to increase the optical absorption transitions between conduction and valence bands. Figure 6.4 shows white light opical images of a fluorinated graphene flake before and after irradiation, a clear enhancement of the contrast is seen after the irradiation procedure.

The experimental observation of a significant decrease of R_{sq}, a reduction of the height and the increase in the optical contrast of fluorinated graphene upon electron irradiation suggests that irradiation dissociates the C-F bonds, consistent with previous experimental reports on electron irradiation of graphite fluoride [84]. Indeed, the ionization cross section for fluorocarbons has a maximum at an electron energy of 80 eV, with higher electron energies leading to progressively smaller cross sections [85]. Therefore, both backscattered and secondary electrons [86] -the latter produced by primary and back-scattered electrons- have low enough energy to break the C-F bonds. However, the secondary electrons produced by back-scattered electrons are unlikely to

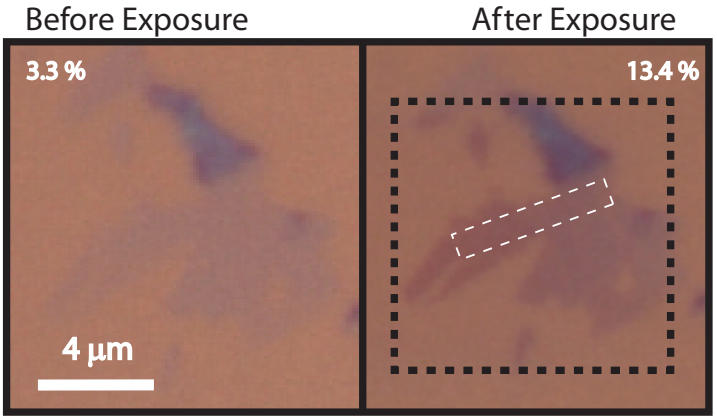

Figure 6.4: (left) An optical photograph taken at 50 X magnification for a freshly exfoliated fluorinated graphene flake (right) Optical photograth taken after irradiation to 1 Ccm^{-2}. A clear enhancement of the optical contrast is observed.

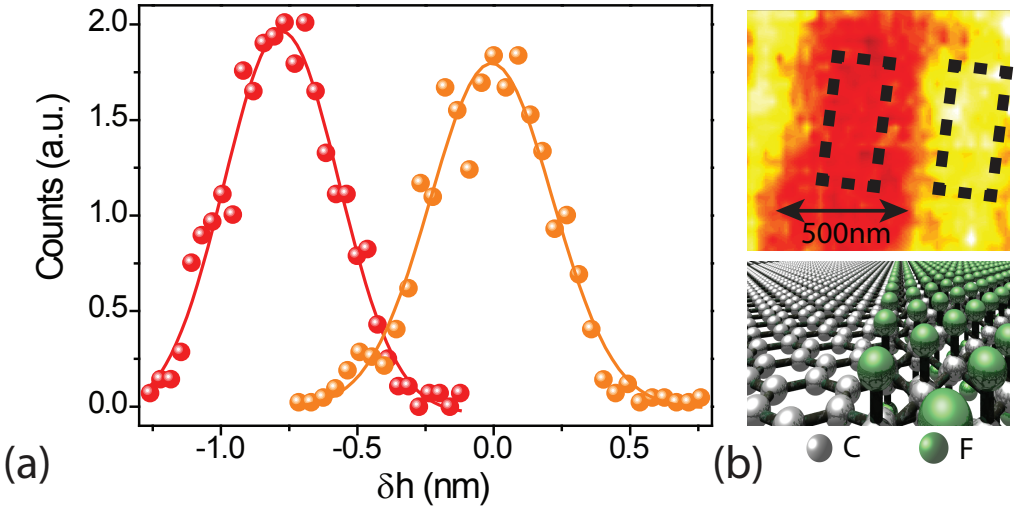

Figure 6.5: (a) shows an AFM histogram data for the unexposed (orange) and exposed (red) fluorinated graphene extracted from the topographical AFM image shown in (b) -yellow corresponds to 2.4 nm measured from the SiO_2 substrate. The bottom panel in (b) illustrates the crystal structure of pristine graphene (grey) and fluorinated graphene (green).

play a role in our experiments since the mean free path of backscattered electrons is larger than the typical size of the studied flakes and much larger than the mean free path of secondary electrons -just a few tens of nm. The electron irradiation dose of 1 Ccm^{-2} used in our experiments corresponds to 6.24×10^{18} electrons/cm^2. Since the concentration of the C-F bonds in our flakes is $\sim 3 \times 10^{14}$ cm^{-2} ($CF_{0.28}$) with a carbon atom density of 10^{15} cm^{-2}, we can estimate the probability of the electron irradiation assisted defluorination to be 5×10^{-5}.

In order to probe the electronic properties of the nanostructures patterned by electron irradiation-assisted defluorination, we have conducted electronic transport measurements over a wide temperature range (from room temperature down to 4.2K) for nanoribbons with 1μm length and 4 different widths (300, 200, 100 and 40nm). The devices were exposed to 1 Ccm^{-2} and after exposure were annealed at a temperature of 200°C (much lower than the 450°C characteristic of the fluorination process) in 10 % H_2/Ar gas for 2 hours. This annealing process removes contaminants due to the electron beam irradiation while leaving the fluorinated graphene insulating. Consequently, the resistance of the electron irradiated regions approaches the typical values for pristine graphene whereas the fluorinated graphene remains insulating. Figure 6.6 shows the I/V characteristics before and after annealing for both cases when the flakes are pristine and when irradiated for two devices in each case. Annealing ultimately restores the resistivity of irradiated graphene to that of graphene while for the unexposed case the material remains insulating.

Figure 6.7(a) shows a typical plot of the zero source-drain bias ($V_{sd} = 0$) differential conductance ($G = dI_{sd}/dV_{sd}$) for a 300nm wide ribbon as a function of gate voltage V_g at T=4.2K. It is apparent that the electrical transport is suppressed for $V_g > 30V$, suggesting the formation of a transport gap as previously reported in etched graphene nanoribbons [65, 87–89]. We observe a transport gap for all the studied ribbons whose value depends on the ribbon width. The temperature and bias dependence of the differential conductance in the transport gap can shed light on the origin of this gap and its relation to the level of disorder, to Coulomb interactions and to electron confinement.

A colour plot of the measured differential conductance in the transport gap region as a function of V_g and V_{sd} shows that the low bias electrical transport is suppressed (see Figure 6.7(b) for $W = 300nm$ and Figure 6.8 for measurements on ribbons with different W). The differential conductance exhibits diamond-like structures characteristic of Coulomb blockade, indicating that electrons are confined in small regions of the nanoribbon with significant charging energy. Consistently, the I_{sd} *versus* V_{sd} curves measured in the transport gap are strongly non-linear, see Figure 6.7(c). In particular,

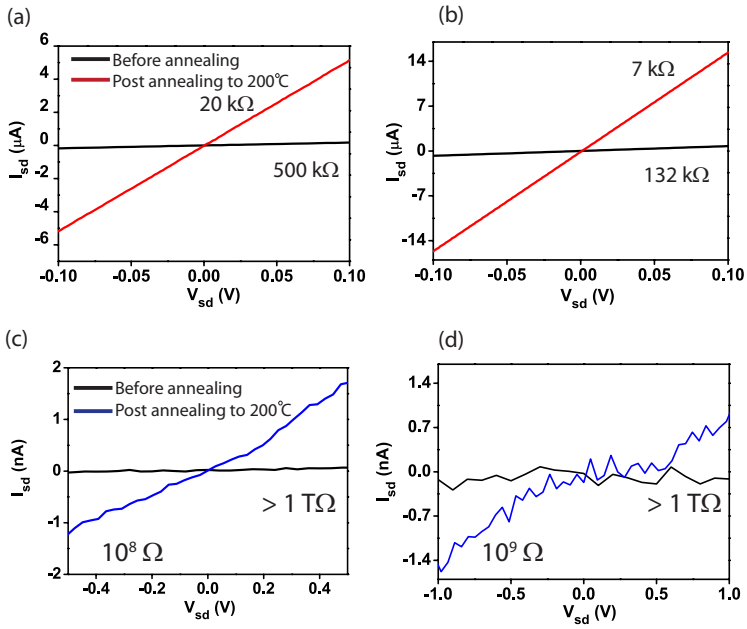

Figure 6.6: (Top left) and (top right) I/V characteristics for fluorinated graphene flakes after being irradiated to 1 Ccm^{-2} and after being annealed to 200 degrees for 2 hours the ultimate resistance is similar to that of graphene. (bottom left) and (bottom right) I/V characteristics for fluorinated graphene before and after anealing to 200 degrees for 2 hours. Note that if there is no irradiation step then the material remains insulating.

a logarithmic scale plot of the IV characteristics highlights more clearly the presence of a source-drain bias voltage transport gap ΔV_{sd} associated with a steep decrease of current for $|V_{sd}| < |\Delta V_{sd}|$ (see Figure 6.7(c)). The corresponding critical electric field which has to be applied in order to activate the conduction in the disordered ribbon is therefore $E_{CR} = \Delta V_{sd}/L$, with L being the ribbon length.

A comparison between the conductance plots for different W reveals that the narrower the nanoribbon is, the wider is ΔV_{sd} and the larger is E_{CR}, see Figure 6.7(d). These observations, combined with the fact that the Coulomb diamonds are irregular and largely overlapping, indicate that the charging regions vary in size. The dependence of ΔV_{sd} and E_{CR} on the nanoribbon width suggests that roughness at the edges of the defluorinated ribbons contributes substantially to create localised states responsible for the transport gap.

In Chapter 5 we show that graphene quantum dots can be realised within partially

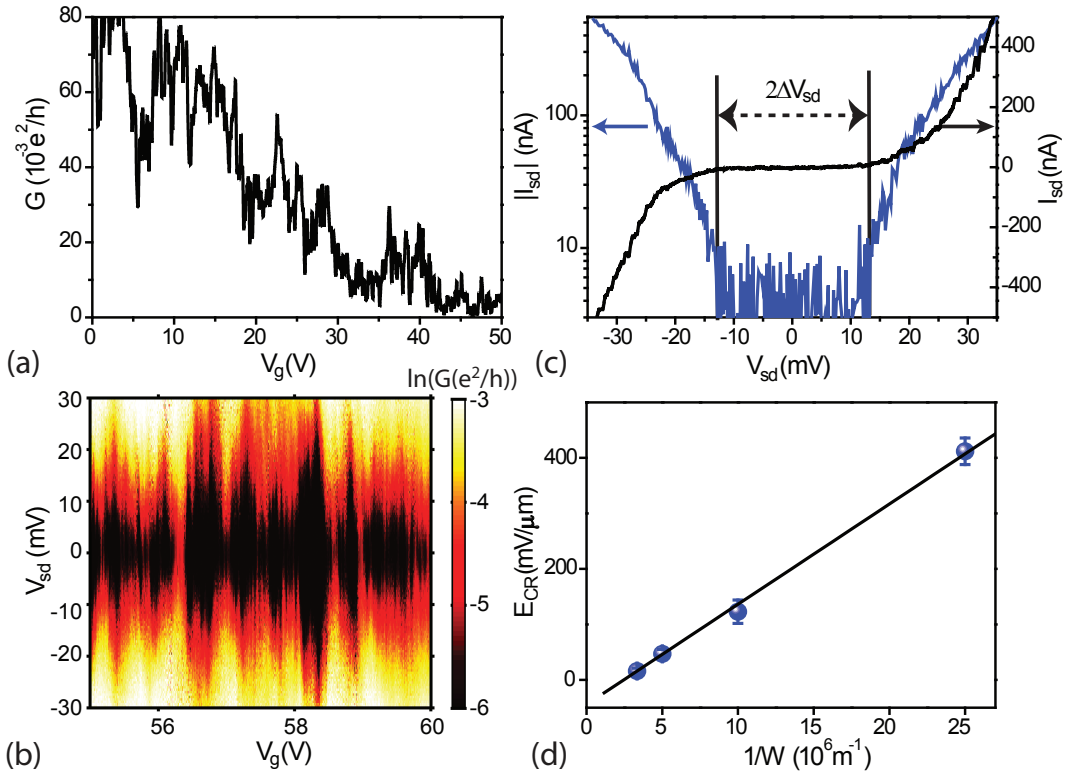

Figure 6.7: (a) shows the differential conductance (G) measured with $V_{ac} = 300\mu V$ excitation voltage as a function of gate voltage (V_g) for zero source-drain bias (V_{sd}) for an electron beam irradiated nanoribbon of fluorinated graphene with width $W = 300nm$ and length $L = 1\mu m$. The colour plot in (b) shows the evolution of G as a function of V_g and V_{sd}. (c) is a plot of the source-drain current -I_{sd} (black)- and the absolute value of I_{sd} (blue) as a function of V_{sd} measured at V_g=55.5V, with the transport gap ΔV_{sd} highlighted by the vertical lines. The plot in (d) summarizes the critical electric field E_{CR} versus the width of the studied nanoribbons. The solid line is a linear fit to the experimental data points (blue).

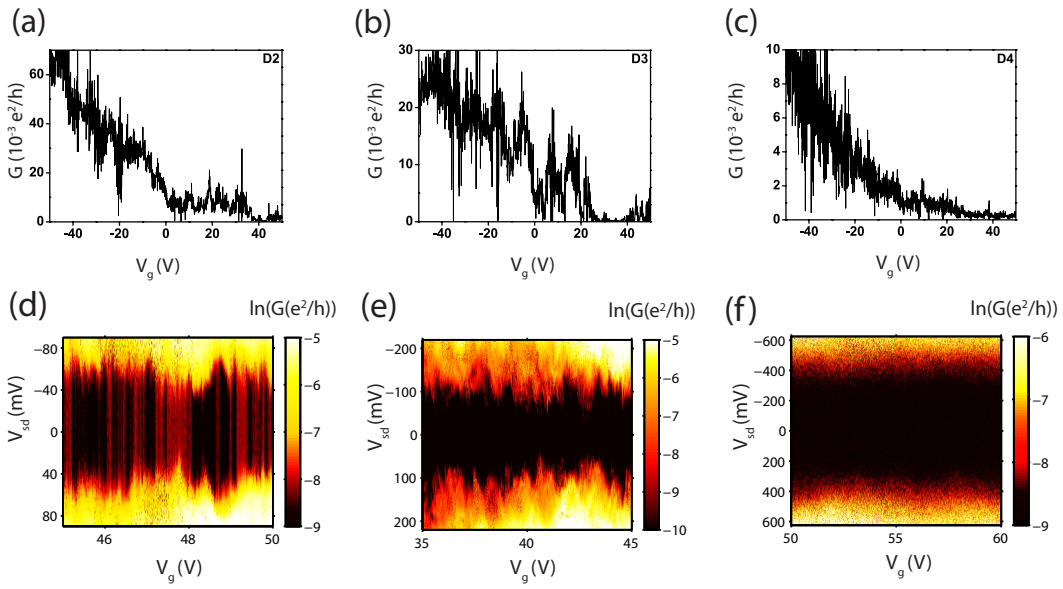

Figure 6.8: (a,b,c) differential conductance plotted against back gate voltage for the lithographically defined ribbons of width W = 200, 100 and 40 nm measured with V_{dc} = 50, 50 and 400 mV respectively. (d,e,f) Color plots of differential conductance as a function of back gate voltage V_g and V_{sd} for ribbons of lithographically defined widths of W = 200, 100 and 40 nm.

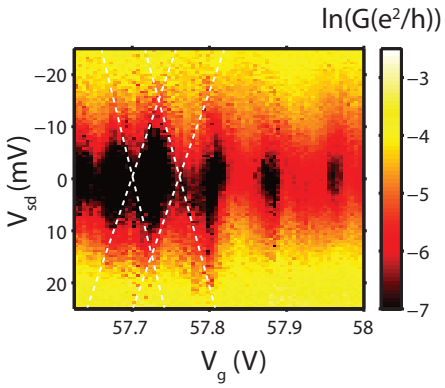

Figure 6.9: A close up of Figure 4(a) showing single electron charging behaviour.

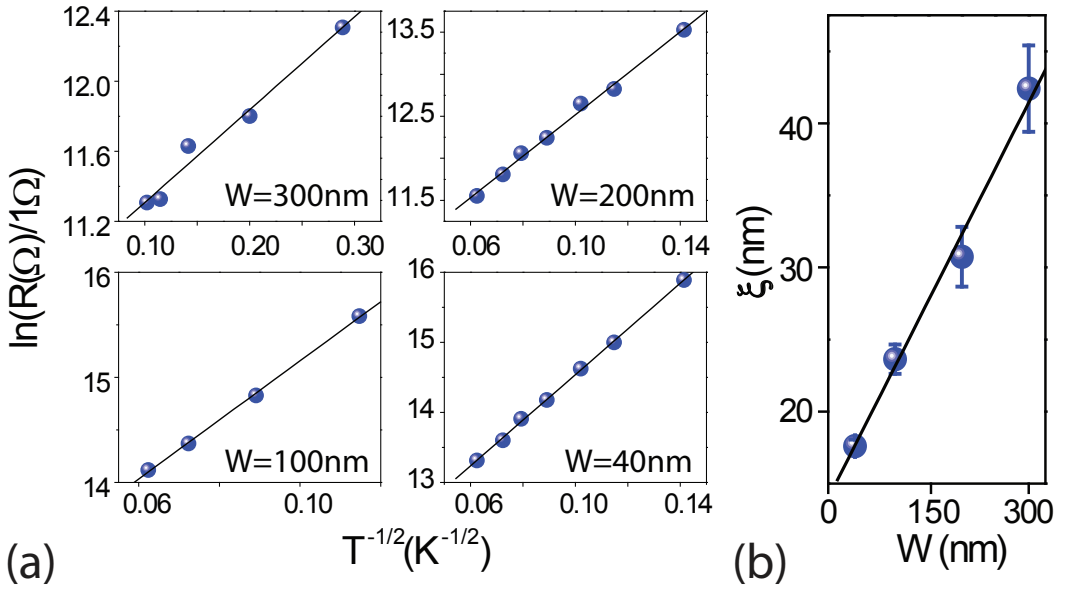

Figure 6.10: Panels in (a) show the resistance of defluorinated nanoribbons in the transport gap region plotted as a function of $T^{-1/2}$ for different ribbons widths. The solid lines are fits to the experimental data (blue dots) to the Efros-Shklovskii variable range hopping. Panel (b) is a plot of the localisation length ξ as a function of the nanoribbon width. The solid line represents a linear fit to the experimental data points (blue).

fluorinated graphene, Figure 6.9 shows a close up of the 300 nm ribbon. One can make out diamond like structures which are typical of Coulomb blockade through a single island. This shows that it may be possible to pattern single quantum dots within insulating fluorinated graphene. The role of Coulomb interactions on the electrical transport in these defluorinated nanoribbons is revealed by the temperature dependence of the conductance in the transport gap. Indeed, the logarithm of the zero bias resistivity fits well to a $T^{-1/2}$ dependence for all the four nanoribbon widths (see Figure 6.10(a)). This functional dependence could either correspond to 1D variable range hopping (VRH) or to 2D VRH in the presence of a Coulomb gap [28, 90]. However, for all the studied devices, the estimated diameter of the smallest charging island is always smaller than the width of the nanoribbon, indicating that electrical transport is through 2D VRH in the presence of Coulomb interactions.

The temperature dependence in the studied defluorinated nanoribbons is therefore described by the Efros-Shklovski VRH relation: $G = G_0 exp(\frac{T_0}{T})^{\frac{-1}{2}}$, where $T_0 = \frac{\beta e^2}{4\pi\epsilon_0\epsilon_r k_B \xi}$. Figure 6.10(b) shows the estimated localization length ξ as a function of the nanoribbon width, using $\epsilon_r = (1+4)/2$. The fact that in all cases we find $\xi < W$ confirms that charge transport in these defluorinated ribbons is diffusive and 2D. Furthermore, we find that ξ scales linearly with the width of the nanoribbon, which is in contrast to the width independent ξ reported in etched graphene nanoribbons [89]. This experimental observation suggests that, contrary to the case of etched nanoribbons, in the defluorinated ribbons both roughness at the edges and disorder in the ribbon play an equally crucial role on the electrons' localization. However, more theoretical studies are required to fully understand the origin of the experimentally observed linear scaling of $\xi(W)$.

6.4 Conclusion

In conclusion we show that the resistivity of insulating fluorinated graphene can be progressively decreased by several orders of magnitude simply by electron beam irradiation. The electron irradiated fluorinated graphene ultimately exhibits the resistance per square of pristine graphene. We attribute the decrease in resistivity to breaking of C-F bonds induced by electron irradiation. Our results show that standard electron beam patterning processes can be used to engineer conductive and semiconductive structures with sizes ranging from few micrometres down to a few tens of nanometres. This opens up new avenues for the fabrication of graphene-based transparent and flexible electronic devices, with defluorinated graphene channels that can be used as metallic interconnects or elements of device structures. Furthermore, patterning channels with different conductivities may lead to novel resistive memory and data storage applications with multiple byte-levels associated to different resistivities.

Chapter 7

Tuning the transport gap of fluorinated graphene via electron beam irradiation.

7.1 Introduction

In the previous chapter results from the electron beam irradiation effects of fluorinated graphene are presented. From this work a open question still remained, -i.e. what happens to the electron transport properties of uniformly irradiated fluorinated graphene flake for different electron beam doses corresponding to a different fluorine coverage ?

In this chapter it is shown that the energy gap in partially fluorinated graphene (PFG) can be tuned by changing the coverage of fluorine adatoms simply via electron-beam irradiation. From a detailed study of the temperature dependence of the resistance (from 4.2K up to room temperature), we find that the electrical conduction in PFG takes place via thermally activated carriers over the energy gap between the localized states and the mobility edge of the conduction band. We show that in $CF_{0.28}$ this energy gap decreases monotonically from $\approx$ 90 meV (after electron irradiation to 0.02 C/cm^{-2}) to $\approx$ 30 meV (after electron irradiation to 0.08 C/cm^{-2}). At the same time we find that PFG displays an insulator to metal transition upon reducing the fluorine coverage. In particular, for small doses (< 0.08 Ccm^{-2}) the electrical conduction in this material is described well by the lightly doped semiconductor model [28] characteristic of standard semiconductors such as germanium and silicon. On the other hand, for high doses (> 0.1 Ccm^{-2}) the electrical conduction takes place via Mott variable range hopping.

7.2 Methods

Partially fluorinated graphene flakes are identified via their low optical contrast, typically 2-4% for few layers with white light. Electrical contacts are fabricated using standard electron beam lithography and thermal evaporation of Cr/Au contacts (5/70nm) followed by a lift-off process in acetone, the final device schematic is shown in Figure 7.1(a). The zero-bias resistance of the devices was measured in a constant voltage configuration with a lock-in amplifier, whereas the excitation voltage was varied to ensure that the energy range where electrical transport takes place is smaller than the energy range associated with the temperature of the electrons. This prevents heating of the electrons and the occurrence of nonequilibrium effects.

The chemical functionalization of graphene with fluorine adatoms is obtained by exposing natural graphite to F_2 atmosphere at 450 °C as described in chapters 4 and 6. In these studies we employ two terminal electrical measurements in transistor devices with a negligible contact resistance at the metal/fluorinated graphene interface as compared to the sample resistance. Figure 7.4(b) shows the extracted energy gap in 2-terminal and 4-terminal configuration, the extracted gap is shown to be the same in both cases.

We change *in-situ* the level of fluorine coverage by irradiating the samples with an incident electron beam of 10keV energy and a current of 0.13 nA as described in chapter 6. Interestingly although the partially reduced fluorinated graphene is disordered and the mobility of the elctrons is low gate dependence of the resistivity is still observed (see Figure 7.1(b)).

7.3 Results and discussion

Figure. 7.2a shows a plot of the zero-bias square resistance (R_{sq}) measured at room temperature after different steps of electron irradiation which correspond to different fluorine coverages. The starting material is the electrically insulating PFG with 28% coverage ($CF_{0.28}$) and $R_{sq} \approx 1T\Omega$. Upon reducing the fluorine coverage we find that R_{sq} decreases monotonically down to $\approx$ 10 kΩ after exposure to $1C/cm^2$. Such low values of R_{sq} are typical of pristine graphene samples and suggest that electron irradiation has reduced PFG to the pristine form.

At the same time, the temperature dependence of R_{sq} measured after different dose exposures shows that PFG undergoes an insulator to metal transition driven by the decrease of fluorine coverage (see Figure. 7.2b). In particular, for $CF_{0.28}$ the R_{sq}

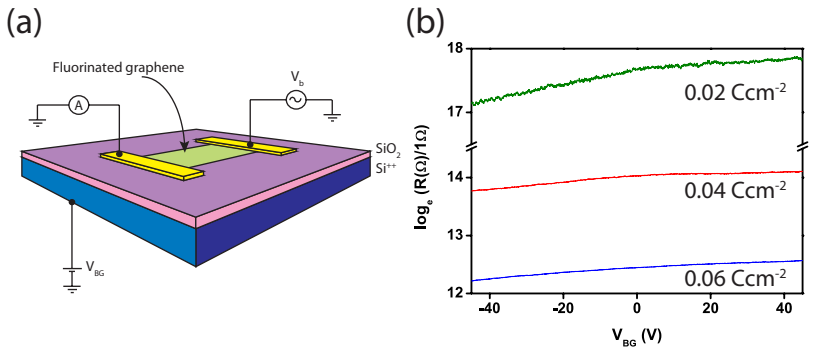

Figure 7.1: (a) Shows the experimental setup (b) shows the back gate dependence of the resistance for three different doses measured at 275 K

diverges when lowering the temperature, as expected for insulating materials. After irradiating to $1C/cm^2$ and after conducting a mild annealing to remove contaminants from the surface [18], the samples exhibit a very weakly temperature dependent R_{sq} which is typical of pristine graphene [91].

7.3.1 Low dose regime

We first present the experimental characterization of PFG exposed to low electron beam irradiation corresponding to doses ranging from 0 up to $0.1C/cm^2$ in steps of $0.02C/cm^2$ (see Figure. 7.2(a)). To understand the nature of the electrical conduction in these materials we consider a semilog plot of the inverse temperature dependence of R_{sq} (see Figure. 7.3(a) and (b)). In all cases we find that $\ln(R_{sq})$ has a similar functional dependence on T^{-1} characterized by four regions with distinct slopes (regions A, B, C and D, see Figure. 7.3(a)). We note that this particular temperature dependence is identical to the well established temperature dependence of lightly doped semiconductors [28]. This similarity suggests that PFG is a semiconductor with impurity states in the energy gap. Previous studies in standard semiconductors [28] have established that region A corresponds to intrinsic electrical conduction due to thermally activated carriers across the energy gap. At sufficiently low temperatures the intrinsic charge carriers become less than the concentration contributed by the impurities. In these regions, i.e. B to D, the conduction is entirely determined by the nature and concentration of impurities. In what follows we adopt the lightly doped semiconductor model

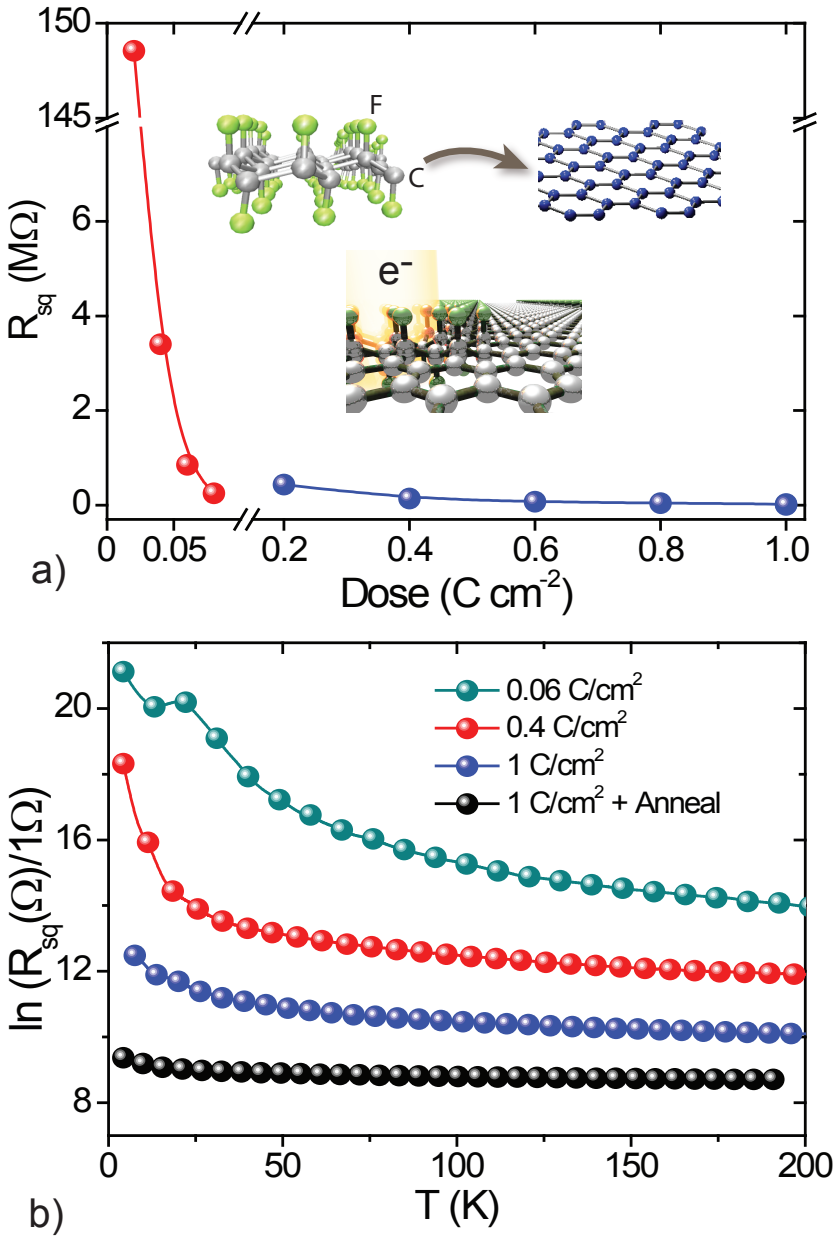

Figure 7.2: (a) Plot of the zero-bias square resistance (R_{sq}) measured at room temperature after different steps of electron beam irradiation. The inset shows a cartoon of the electron-irradiation induced defluorination process. (b) Plot of the temperature dependence of the ln(R_{sq}) after subsequent electron irradiation steps. A transition from an insulating state in $CF_{0.28}$ to a metallic state is observed after complete defluorination by exposure to a dose of $1C/cm^2$.

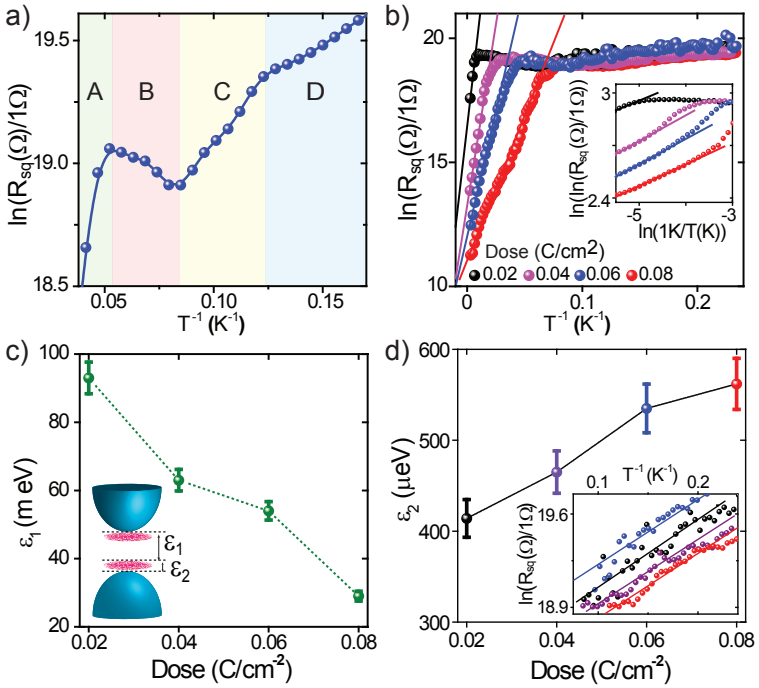

Figure 7.3: (a) Semilog plot of the inverse temperature dependence of R_{sq} for a $CF_{0.28}$ sample irradiated to 0.06 Ccm^{-2} in the temperature range < 30 K. The four regions (A, B, C and D) with distinct slopes of $\ln(R_{sq})$ *vs.* T^{-1} characteristic of lightly doped semiconductors are highlighted on the graph. (b) Semilog plot of the inverse temperature dependence of R_{sq} for samples irradiated to different electron doses and measured up to room temperature. The continuous lines are linear fits to the exponential dependence of the resistance in region A due to thermally activated carriers across the energy gap. The plot in the inset highlights the exponential dependence of the resistance in A by presenting a double-log scale plot. (c) Shows a plot of the energy gap ϵ_1 between the impurity states and the conduction band edge (sketch in the inset) as a function of electron dose irradiation. (d) Plot of the hopping conduction activation energy extracted from the linear fit of the semilog inverse temperature dependence of R for different doses of electron irradiation shown in the inset.

to explain the evolution of the energy dispersion in fluorinated graphene as a function of F-coverage.

The intrinsic carrier concentrations of electrons and holes in region A gives an exponential dependence of the resistance on temperature: $R(T) = R_0 e^{\frac{\epsilon_1}{2k_B T}}$ where ϵ_1 is an energy gap between the impurity states and the conduction band edge. Due to the impurity and/or defect induced states, ϵ_1 in these PFG is smaller than the true energy gap corresponding to the difference between the top and bottom of the valence and

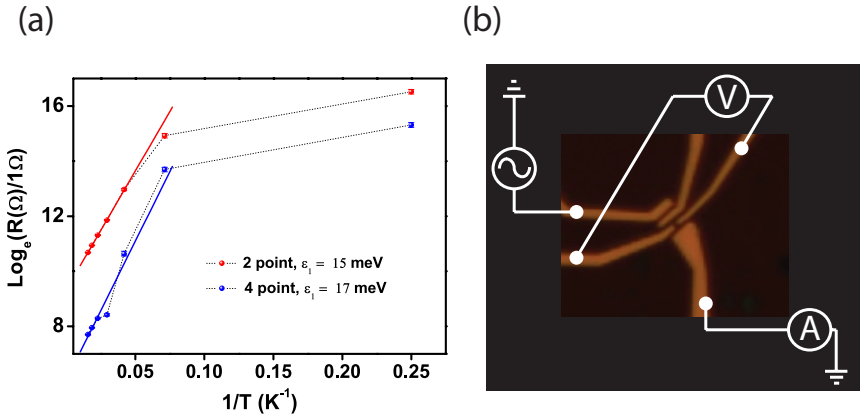

Figure 7.4: (a) Comparson of the temperature dependence of the resistivity for 2 and 4 probe measurements, note a similar ϵ_1 is extracted in both cases (b) shows the experimental setup for the measurement.

conduction bands (see inset in Figure 7.3(c)). The value of ϵ_1 and its dependence on the electron irradiation are readily determined from a linear fit to the plot of $\ln(R_{sq})$ *vs.* T^{-1} for region A after different low dose irradiation (up to 0.08 C/cm^2), see Figure 7.3(c). We find that ϵ_1 decreases monotonically from $\approx$ 90 meV (after irradiation to 0.02 C/cm^2) to $\approx$ 30 meV (after irradiation to 0.08 C/cm^2). The narrowing of the energy gap due to electron irradiation-assisted defluorination is also consistent with the observed increase in optical contrast of PFG when increasing the electron dose irradiation. In this case, when the energy gap ϵ_1 is reduced more optical transitions can occur in PFG causing an increase of the optical contrast [27].

Similarly to lightly doped semiconductors [28], upon lowering the temperature the R_{sq} of PFG crosses over to region B which is the so-called saturation range. In B all impurities are ionized and the carrier concentration in the band is nearly temperature independent. At the same time, upon lowering the temperature the weakening of the phonon scattering affects the charge carrier mobility ultimately resulting in a weak R_{sq} dependence on T commonly observed in lightly doped semiconductors [28]. Region C is known as the freezing-out range, where the extrinsic charge carriers are recaptured by the defects and/or impurities. In this region the temperature dependence of the sample resistance is commonly described by $R_T = R_3 e^{\frac{\epsilon_2}{2k_B T}}$ with an activation energy ϵ_2 which is much smaller than ϵ_1 [28]. In particular, we find that ϵ_2 is enhanced from $\approx$ 0.4 meV after an electron irradiation of 0.02 C/cm^2 to $\approx$ 0.55 meV after exposure to a dose of 0.08 C/cm^2 , see Figure 7.3(d). The observed increase of ϵ_2

upon electron irradiation is possibly due to an increase of random Coulomb potential associated with the dangling bonds created by the irradiation-assisted defluorination process [92]. Finally, at the lowest temperatures in region D the main contribution to the electrical conductivity comes from electrons hopping directly between localized states at sub-gap energies. To exclude barriers at the contacts we compare 2 and 4 probe measurements. Figure 7.4 shows the temperature dependence of the resistivity, we find that a similar ϵ_1 is extracted in both configurations indicating that the probed gap is intrinsic to the partially fluorinated graphene flake and has nothing to do with the effect of the contacts.

At lower temperatures we are probing transport in the hopping regime and a greater understanding of the transport through these sub - gap states can be revealed by looking at the I/V characteristics. Figure 7.5(a) shows the I/V curves measured at 4.2 K, numerical simulations show that the I/V curves can be explained by the following equation [93],

$$I \propto ((V - V_t)/V_t)^{\alpha} \tag{7.1}$$

where V_t is the threshold voltage where transport is first detected and $\alpha = 1$, 1.67 for 1D and 2D electron transport [93] through conductive particles enclosed within an insulating material, while for quasi 2D arrays have been shown to have critical exponents of $\alpha \approx 4$ [94]. Experimental studies of reduced graphene oxide have revealed an exponent of ≈ 3.2 [95] which is larger than 1.67. This is attributed to the fact that this system is quasi 2D and is closer to the expected value of 4.

Figure 7.5(b) shows the fits of our experimental I-V data measured at 4.2K to the relation in Eq. 7.1 for different electron doses as indicated in the graph. The extracted values for α as a function of dose are reported in Figure 7.6. We find that in PFG materials α is 1.3 ± 0.5 which is in good agreement with the theoretically expected value of 1.6 expected for hopping conduction through small 2 dimensional metallic islands.

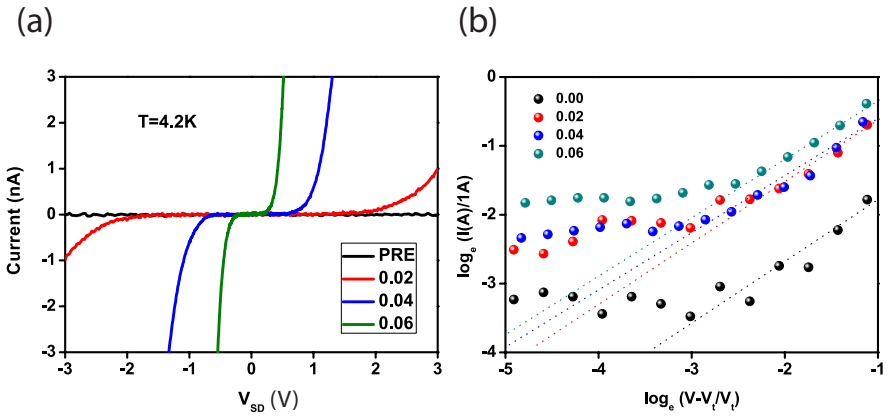

Figure 7.5: (a) I-V curves at T = 4.2 K for different fluorine coverages after different electron irradiation doses from 0.02 to 0.06 Ccm^{-}2 (b) Fits of the I-V curves to the logarithm of Eq. 2.7 in order to extract α.

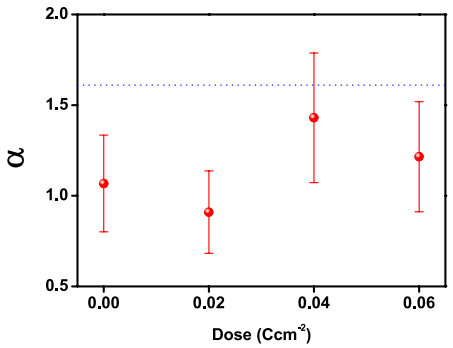

Figure 7.6: Plot of α determined from the fits shown in 1.4(b) for different doses. The dashed line indicates the theoretically expected $\alpha = 1.6$ for transport through 2D metallic islands.

7.3.2 High dose regime

We now turn our attention to the higher dose regime, which corresponds to a lower coverage of fluorine adatoms. Figure 7.7(a) shows a semilog plot of the temperature dependence of the resitance after various electron beam irradiations from a dose of $0.2C/cm^2$ up to $1C/cm^2$. In all cases we find that at high enough temperatures the conduction in these samples takes place via hopping through localised states with $R(T) \propto e^{\frac{\epsilon_a}{2k_BT}}$ and ϵ_a the hopping activation energy. This temperature range corresponds to region C and the values of ϵ_a extracted from the fits are plotted in Figure 7.7b. It is apparent that ϵ_a shows a monotonic decrease with increasing dose, consistent with the narrowing of the energy gap.

Upon lowering the temperature the $\ln(R_{sq})$ is non-linear in T^{-1}, indicating that another mechanism of conduction is at play in this D region (see Figure 7.7a). To idenfity the specific hopping mechanism of conduction dominating in D, we consider the generic expression $R(T) = R_0 e^{(T_0/T)^p}$ where p is a parameter that depends on the dimensionality of the system as well as the conduction mechanism and T_0 is the characteristic temperature of the system which correlates to the degree of localisation. For a two dimensional system -such as fluorinated graphene- p is equal to 1 for thermally activated transport, 1/2 for Efros-Shklovskii variable range hopping (ESVRH) with Coulomb interactions and 1/3 for Mott variable range hopping (MVRH) [96]. The exponent p can be determined from a linear fit to the reduced activation energy $W = -\ln R(T)/(\ln T) = p(T_0/T)^p$ in a logarithmic scale plot, see Figure 7.7(c) and 7.7(d). [97] We find that for all the studied doses the best fit gives p=1/3, demonstrating that the electrical conduction takes place by MVRH. From a fit of $R(T)$ to MVRH conduction mechanism (see Figure 7.7(e)) we can extract the values of T_0 for each different electron dose irradiation. This hopping parameter is shown in figure 7.8(a) and it is found to decrease with increasing the electron dose suggesting an increase of sub-gap states.

Theoretically, an energy gap whose value depends on the coverage of adatoms is expected in the limit that the mean free path of charge carriers is longer than the average distance between adatoms [98]. In this case, the Bragg scattering of electron waves by the adatoms opens a uniform energy gap which is immune to the positional disorder of the adatoms. Indeed, in our experiments the mean free path in this low-dose regime is always longer than the distance between fluorine adatoms. The charge carrier mobilities in PFG are typically of the order of $\approx 10cm^2/Vs$ (see Fig. 1.4(b)). The Fermi velocity in PFG is $v_F = \sqrt{\frac{2n\pi\hbar^2}{em*^2}}$ with n charge density, e the charge of the

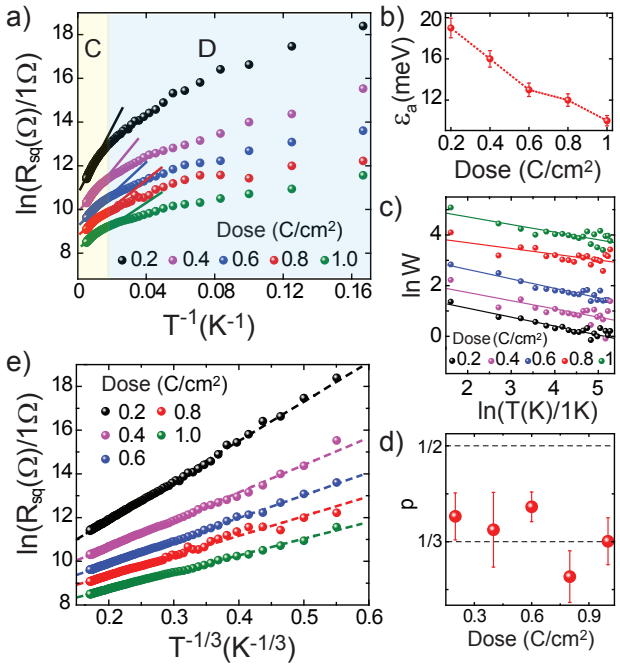

Figure 7.7: (a) Semilog plot of the inverse temperature dependence of R_{sq} after various high dose irradiation steps as indicated in the graph. The continuous lines are a fit to thermally activated transport. (b) Plot of the activation energy of the hopping conduction via localised states as a function of electron dose irradiation extracted from the linear fits in (a). (c) Logaritmic scale plot of $W = -\ln(R(T))/\ln(T)$ *vs.* temperature, the continuous lines are fit to $W = p(T_0/T)^p$ and (d) shows the best fit values for p for each given electron dose irradiation. (e) Shows a semilog plot of R_{sq} as a function of $T^{-1/3}$, the dashed lines are fit to the Mott variable range hopping.

electron and $m*$ the effective mass in fluorinated graphene [23] . Therefore, the typical mean free path for charge carriers in our devices is $l = \frac{\hbar\mu}{e}\sqrt{\frac{2n\pi}{e}} \approx 1.5$nm. Since the average distance between fluorine adatoms is smaller than l down to a F-coverage of 1.5%, we can conclude that in our PFG materials Bragg scattering of electron waves plays a primary role in opening a uniform energy gap.

Finally, Figure 7.9 shows a sketch of the low-energy energy dispersion of PFG for different fluorine coverages. For large fluorine content, PFG has a large band gap with localised states near the conduction and valence band edges. As the fluorine coverage is reduced by electron irradiation, the energy gap is reduced and at the same time the impurity band width increases [57, 63]. When a large proportion of fluorine has been removed the gap is almost closed and conduction takes place through a dense region of

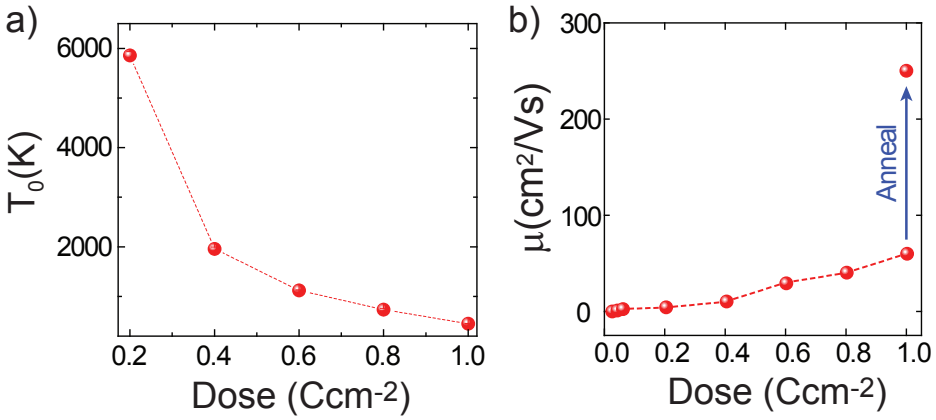

Figure 7.8: Graphs in (a) and (b) show the characteristic temperature T_0 of the Mott variable range hopping mechanism and the field effect mobility as a function of electron beam dose irradiation.

impurity states. Ultimately a metallic state is attained, and the band gap is reduced to zero.

7.4 Conclusion

In conclusion we show that the energy gap in partially fluorinated graphene can be tuned by changing the coverage of fluorine adatoms simply via electron-beam irradiation. We show that in $CF_{0.28}$ this energy gap decreases monotonically from $\approx$ 90 meV (after electron irradiation to 0.02 C/cm^{-2}) to $\approx$ 30 meV (after electron irradiation to 0.08 C/cm^{-2}). Correspondingly, we observe that these partially fluorinated graphene materials display an insulator to metal transition when decreasing the coverage of fluorine adatoms. In particular, for low doses of electron beam irradiation, PFG is a lightly doped semiconductor with an intrinsic energy gap whose value depends on the fluorine coverage. For higher doses, the transport is governed by Mott variable range hopping. These experimental findings highlight that electron beam irradiation of fluorinated graphene is a novel way to engineer the band gap in graphene materials.

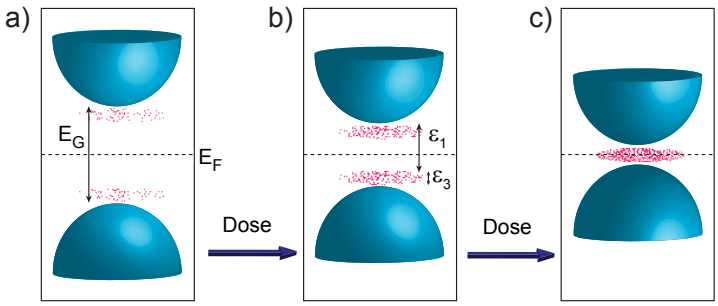

Figure 7.9: (a), (b) and (c) show a sketch of the low-energy dispersion for the partially fluorinated graphene after subsequent steps of dose irradiation. The higher the dose irradiation, the smaller is the energy gap.

Chapter 8

Novel Highly Conductive and Transparent Graphene-Based Conductors.

8.1 Introduction

As discussed in chapter 1, future wearable electronics, displays and photovoltaic devices require materials which are mechanically flexible, lightweight and low-cost, in addition to being electrically conductive and optically transparent [99–101]. Nowadays indium tin oxide (ITO) is the most wide spread transparent conductor in optoelectronic applications, however the mechanical rigidity of this material limits its use for future flexible devices. In the race to find novel transparent conductors, graphene monolayers and multilayers are the leading candidates as they have the potential to satisfy all future requirements. Graphene, one-atom-thick layer of carbon atoms, is transparent[8], conducting [4, 102], bendable [103] and yet one of the strongest known materials [6]. However, the use of graphene as a truly transparent conductor remains a great challenge because the lowest values of its sheet resistance (R_s) demonstrated so far are above the values of commercially available ITO (i.e. 10 $\Omega/\square$ at an optical transmittance Tr=85% [104]). Currently many efforts are concentrated on decreasing the R_s of graphene-based materials while maintaining a high Tr, which will allow their potential to be harnessed in optoelectronic applications. To date, the best values of sheet resistance

The results in this Chapter have been published as I. Khrapach, F. Withers, T. H. Bointon, D. K. Polyushkin, W. L. Barnes, S. Russo, M. F. Craciun, *Advanced Materials,* **24**, 2844 (2012)

and transmittance found in graphene-based materials are still far from the performances of ITO, with typical values of R_s=30 Ω/□ at Tr=90% for graphene multilayers [103, 105] and R_s=125 Ω/□ at Tr=97.7% for chemically doped graphene [103, 106, 107]

In this chapter we present results of novel graphene-based transparent conductors with a sheet resistance of 8.8 Ω/□ at Tr=84%, a carrier density as high as $8.9\times10^{14} cm^{-2}$ and a room temperature carrier mean free path as large as $\sim 0.6\mu m$. These materials are obtained by intercalating few-layer graphene (FLG) with ferric chloride ($FeCl_3$) [108, 109]. Through a combined study of electrical transport and optical transmission measurements we demonstrate that $FeCl_3$ enhances the electrical conductivity of FLG while leaving these graphene-based materials highly transparent. We also show that $FeCl_3$-FLG are stable in air up to one year, which demonstrates the potential of these materials for industrial production of transparent conductors. The unique combination of record low sheet resistance, high optical transparency and large room temperature mean free path has not been demonstrated so far in any other doped graphene system, and opens new avenues for graphene-based optoelectronics.

8.2 Experimental details

Pristine FLG ranging from two- to five-layers (2L to 5L) were obtained by micromechanical cleavage of natural graphite [4] on glass or SiO_2/Si. The number of layers composing each FLG was determined by two separate characterization methods firstly optical contrast shown in Figure 8.1(b) which increases with increasing layer number. Secondly by Raman spectroscopy where we use the method described in section 3.1.2.1 from reference [44]. To utilize this method for the glass substrates we place the graphene face down on the Si/SiO_2 substrate in order to obtain the silicon peak, this is schematically shown in Figure 8.1(c) with the ratio of the peaks shown in Figure 8.1(d).

The intercalation process with $FeCl_3$ is performed in vacuum. Both anhydrous $FeCl_3$ powder and the substrate with exfoliated FLG are positioned in different zones inside a glass tube. The tube is pumped down to $2 \times 10^{-4} mbar$ at room temperature for 1 hour to reduce the contamination by water molecules. Subsequently, the FLG and the powder are heated for 7.5 hours at 360°C and 310°C, respectively. A rate of change of temperature of 10°C/min is used during the warming and cooling of the two zones. Ohmic contacts are fabricated on $FeCl_3$-FLG by means of electron-beam lithography and lift-off of thermally evaporated chrome/gold bilayer (5/50 nm). We have fabricated $FeCl_3$-FLG on both SiO_2/Si and glass substrates and we found no significant differences

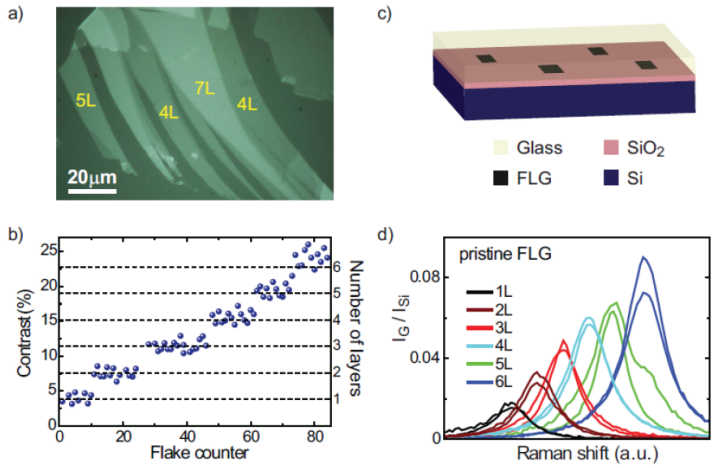

Figure 8.1: a) Optical micrograph of a FLG flake on glass taken with white light. The glass substrate was suspended in air. b) The optical contrast of FLG on glass plotted for 85 flakes. c) Schematic of the glass substrate with FLG on top of the SiO2/Si. d) The ratios of the intensities of the G peak and the Si peak (IG/ISi). The curves are shifted on the x axis for clarity.

in their transport properties.

Raman spectra are collected in ambient air and at room temperature with a Renishaw spectrometer. An excitation laser with a wavelength of 532 nm, focused to a spot size of 1.5 μm diameter and a $\times$100 objective lens are used. To avoid sample damage or laser induced heating, the incident power is kept at 5 mW.

The longitudinal and the Hall resistances are studied in a 4-probe configuration by applying an a.c. current bias and measuring the resulting longitudinal and transversal voltages with a lock-in amplifier. The excitation current is varied to ensure that the energy range where electrical transport takes place is smaller than the energy range associated to the temperature of the electrons. This prevents heating of the electrons and the occurrence of nonequilibrium effects.

The transmission of pristine FLG and $FeCl_3$-FLG is characterized by measuring the bright-field transmission spectra. A system based on an inverted optical microscope (Nikon Eclipse TE2000-U) combined with a spectrometer and CCD camera (Princeton Instruments, SpectraPro 2500i) is used to acquire data. White light from a tungsten filament lamp is used to illuminate the samples and, after passing through the sample, is collected by a dry Nikon lens (S Plan Fluor ELWD) $\times$40 of NA 0.60. A slit width of 50 μm is used for the spectrometer, yielding a spectral resolution $<$ 1 nm for the

measurements. In the spectrometer the dispersed light is projected onto the 1024 by 256 lines of the CCD camera. Data from the camera are extracted to give the transmission spectra of the flake, or part of it, the data being normalized to the signal obtained through a region of bare substrate. For the visually uniform parts of the flakes, spectra are averaged along several lines of the CCD camera to improve the signal-to-noise ratio.

8.3 Results

Figure 8.2(a) shows the Raman spectra of pristine FLG on SiO_2/Si, with the G-band at 1580 cm^{-1} and the 2D-band at 2700 cm^{-1} [43, 53]. As expected for pristine FLGs, increasing the number of layers results in an increase of the G-band intensity [44], whereas the 2D-band acquires a multi-peak structure [43, 53]. The charge transfer from $FeCl_3$ to graphene modifies the Raman spectra of FLGs in two distinctive ways [108–110]: an upshift of the G-band and a change of the 2D-band from multi- to single-peak structure, respectively (see Figure 8.2(a)). The shift of the G-band to G_1=1612 cm^{-1} is a signature of a graphene sheet with only one adjacent $FeCl_3$ layer, whereas the shift to G_2=1625 cm^{-1} characterizes a graphene sheet sandwiched between two $FeCl_3$ layers [15, 108, 109] (see Figure 8.2(b)). The frequencies, linewidths and lineshapes of the G_1 and G_2 peaks do not depend on the number of graphene layers which indicates the decoupling of the FLGs into separate monolayers due to the intercalation of $FeCl_3$ between the graphene sheets. This is consistent with the changes in the 2D-band shape and with the Raman studies of other intercalants such as Potassium [47, 111] and Rubidium [111]. These observations allow us to identify the structure of intercalated 2L samples as one $FeCl_3$ layer sandwiched between the two graphene sheets. However, the structural determination of thicker $FeCl_3$-FLG cannot rely uniquely on the Raman spectra, it requires complementary knowledge from electrical transport experiments. Direct structural determination for example by X-ray diffraction would be valuable to confirm the findings of Raman and electrical transport measurements, however the small thickness of $FeCl_3$-FLG and the substrate effects make it difficult to apply such techniques to these systems.

To characterize the structure of thicker $FeCl_3$-FLG, we study the oscillatory behaviour of the longitudinal magneto-conductance (G_{xx}) in a perpendicular magnetic field (i.e. Shubnikov-de Haas oscillations, see Figure 8.3(a)) in combination with the Hall resistance (R_{xy}). Here we discuss the representative data for an intercalated 5L sample patterned into a Hall bar geometry. Firstly the data need to be converted into

longitudinal conductivity instead of resistivity which can be done as follows: since conductances are additive, the analysis of Shubnikov-de Haas oscillations is performed on the longitudinal conductivity $\sigma_{xx} = \rho_{xx}/[\rho_{xx}^2 + \rho_{xy}^2]$ (with ρ_{xx} and ρ_{xy} the longitudinal and transversal resistivity, respectively). The low frequency magneto-conductivity oscillations shown in Figure 8.4(a) are obtained by averaging out the high frequency oscillations, whereas to obtain the high frequency oscillations shown in Figure 8.4(b) we subtract the low frequency oscillations from the longitudinal conductivity. Figure 8.3(a) shows SdHO of G_{xx} as a function of perpendicular magnetic field (B) for different temperatures. It is apparent that for T<10K G_{xx} oscillates with two distinct frequencies. For T>10K only the lower frequency oscillations are visible. These observations indicate that electrical conduction takes place through parallel gases of charge carriers with distinct densities. Indeed, the Fourier transform of $G_{xx}(1/B)$ yields peaks at frequencies $f_{SdHO_1} = 1100T$ and $f_{SdHO_2} = 55T$ (see Figure 8.3(b)), corresponding to charge carrier densities $n_1 = (1.07 \times 10^{14} \pm 5 \times 10^{11})cm^{-2}$ and $n_2 = (5.3 \times 10^{12} \pm 4 \times 10^{11})cm^{-2}$ (with $n_i = 4ef_{SdHO_i}/h$ [38, 102]).

The temperature dependence of the magneto-conductivity oscillations allows us to determine the cyclotron mass of the charge carriers in these parallel gases. Figures 8.4(a) and (b) show the low- and high-frequency magneto-conductivity oscillations for different temperatures. In all cases, the temperature decay of the amplitude is well described by $A(T) \propto T/sinh(2\pi^2 k_B T m_c/\hbar eB)$ (see Figure 8.4(c)), with cyclotron masses $m_{c_1} = (0.25 \pm 0.05)m_e$ and $m_{c_2} = (0.08 \pm 0.001)m_e$ for the high- and low-frequency oscillations, respectively. These values correspond to the expected values of cyclotron mass for massless Dirac fermions $m_c = \sqrt{h^2 n/4\pi v_F^2} = 0.21m_e$ at n_1 and for chiral massive charge carriers of bilayer graphene $m_c = \sqrt{\hbar^2 v_F^2 \pi n + (\gamma/2)^2}/v_F^2 = 0.084m_e$ at n_2 (with $v_F = 10^6$m/s the Fermi velocity [102] and γ the interlayer hopping energy [15]). Therefore, intercalation of $FeCl_3$ decouples the stacked 5L graphene into parallel gases of massless (1L) and massive (2L) charge carriers.

The charge carrier type (electrons or holes) and the number of parallel gases present in $FeCl_3$-FLG is readily identified by correlating SdHO to the Hall resistance measurements. The linear dependence of R_{xy}(B) with positive slope identifies charge carriers as holes, with a Hall carrier density $n_H = B/(eR_{xy}) = 3 \times 10^{14} cm^{-2}$ (see Figure 8.3(b)). Since the total carrier density $n_{tot} = \sum_i n_i$ should be higher than $n_H = (\sum_i n_i \mu_i)^2 / \sum_i n_i \mu_i^2$ (with n_i and μ_i the carrier density and mobility of each hole gas) [112], only a minimum of three parallel hole gases with $n_1 = 1.07 \times 10^{14} cm^{-2}$ can explain the estimated value of n_H. Therefore, the electrical transport characterization

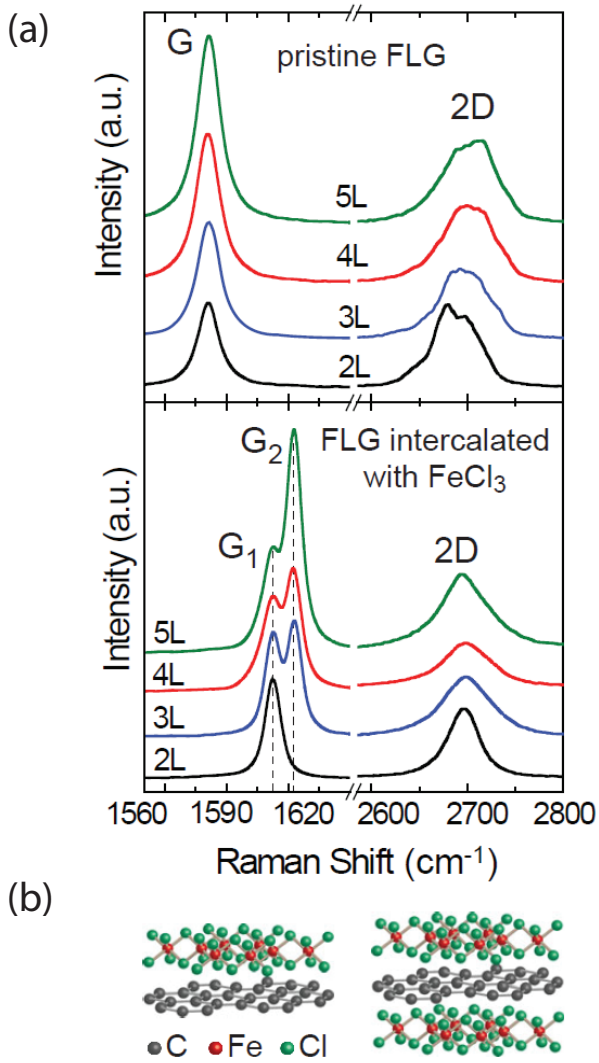

Figure 8.2: a) The G and 2D Raman bands of pristine FLG (top) and of $FeCl_3$-FLG (bottom) with different thicknesses ranging from 2L to 5L. (b) The Raman shift of G to G_1 and G_2 stem for a graphene sheet with one or two adjacent $FeCl_3$ layers as shown by the schematic crystal structure.

demonstrates the presence of four parallel hole gases, of which one with bilayer character (and density n_2) and three with monolayer character (each with density n_1). These findings are confirmed by the Raman spectra taken after the device fabrication showing the presence of pristine G, G_1 and G_2 peaks (see Figure 8.5) which also shows that the intercalation is uniform if not complete over the whole sample. A schematic of this

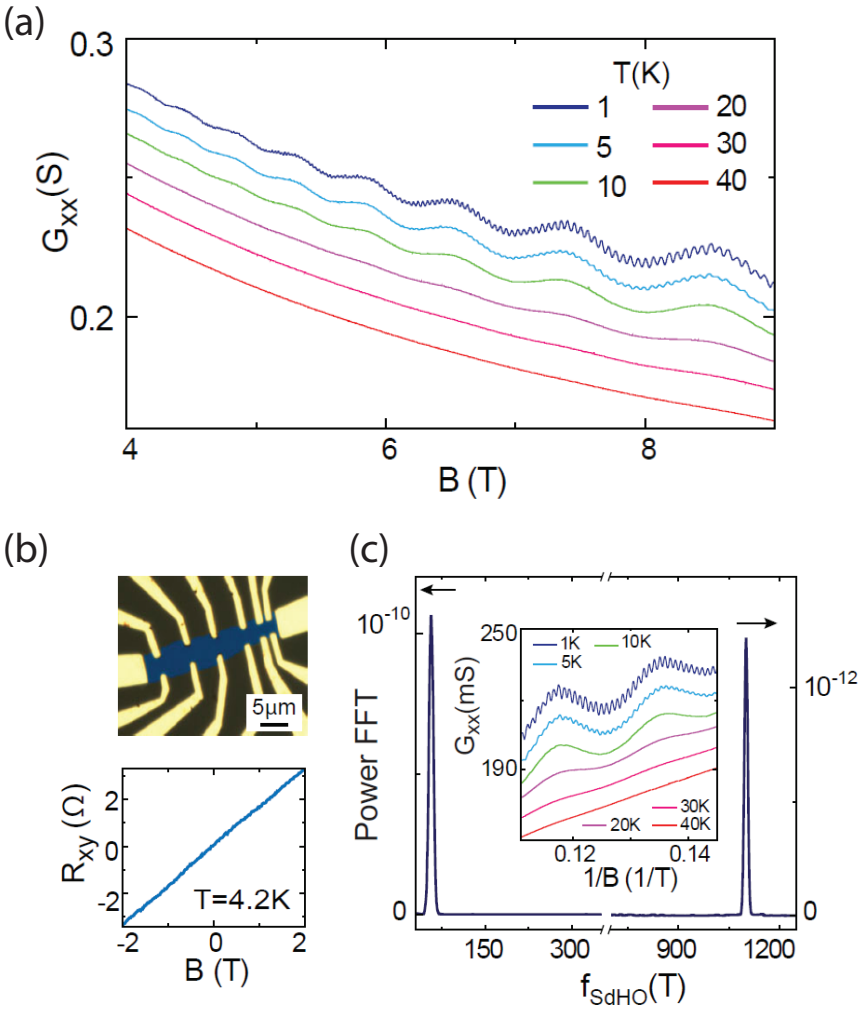

Figure 8.3: a) Longitudinal conductance (G_{xx}) as a function of magnetic field at different temperatures for a 5 L intercalated graphene flake (curves shifted for clarity). b) Top panel: optical microscope image of a Hall bar device. Bottom panel: Hall resistance (R_{xy}) as function of magnetic field. c) Fourier transform of $G_{xx}(1/B)$ with peaks at frequencies $f^{(1)}_{SdH} = 1100T$ and $f^{(2)}_{SdH} = 55T$. The inset shows G_{xx} as a function of inverse magnetic field at different temperatures (curves shifted for clarity).

crystal structure is illustrated in Figure 8.4(d). The bilayer gas is likely to be caused by the first two layers of the stacking which have been de-intercalated due to rinsing in acetone during lift-off [110]. The bottom part of the stacking has a per-layer doping

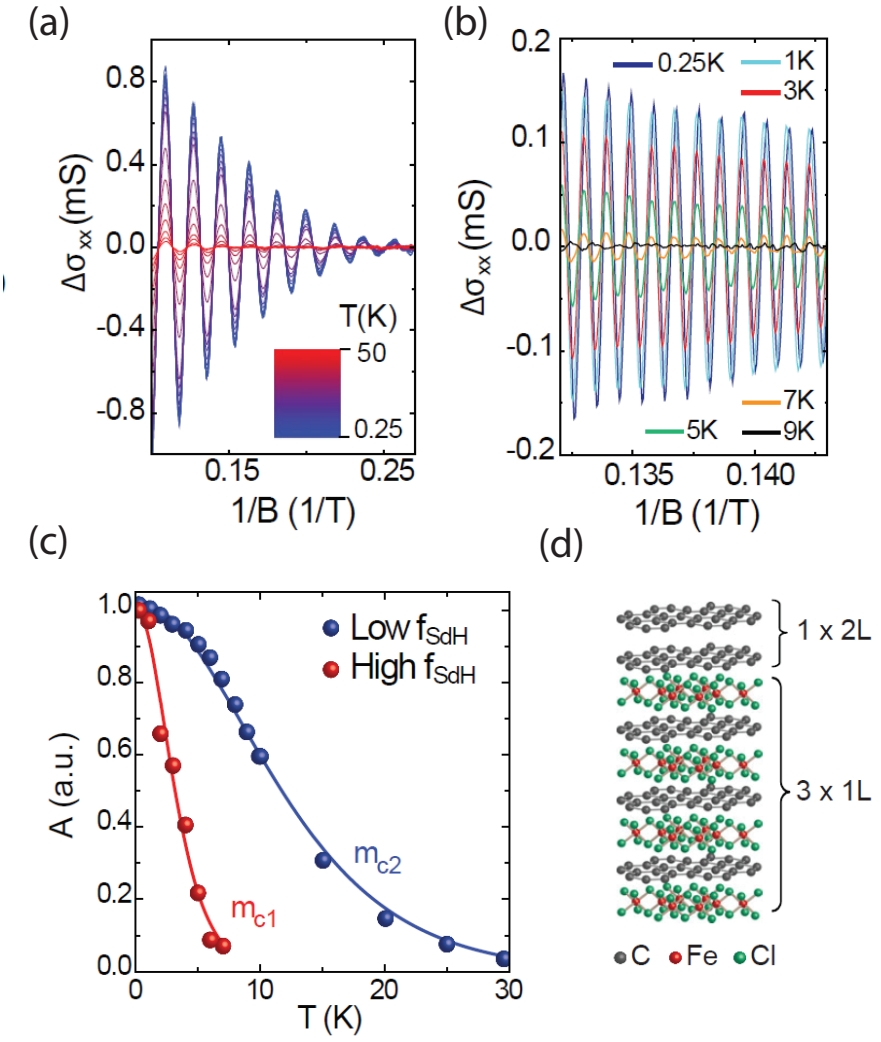

Figure 8.4: a) and b), respectively, show the low- and high- frequency magneto-conductivity oscillations vs 1/B extracted from the measurements in 8.3(a). c) Temperature decay of the amplitude (A) of $\Delta\sigma_{xx}$ oscillations at B=6.2T. The amplitudes are normalized to their values at T=0.25K. The continuous lines are fits to $A(T)/A(0.25)$ with the cyclotron mass m_c as the only fitting parameter. h) Schematic crystal structure of a 5L $FeCl_3$-FLG in which electrical transport takes place through four parallel conductive planes, one with bilayer character and three with monolayer character.

of $n_1 = 1.07 \times 10^{14} cm^{-2}$ and the stoichiometry of stage-1 $FeCl_3$ graphite intercalation compounds (i.e. where each graphene layer is sandwiched by two $FeCl_3$ layers) [15].

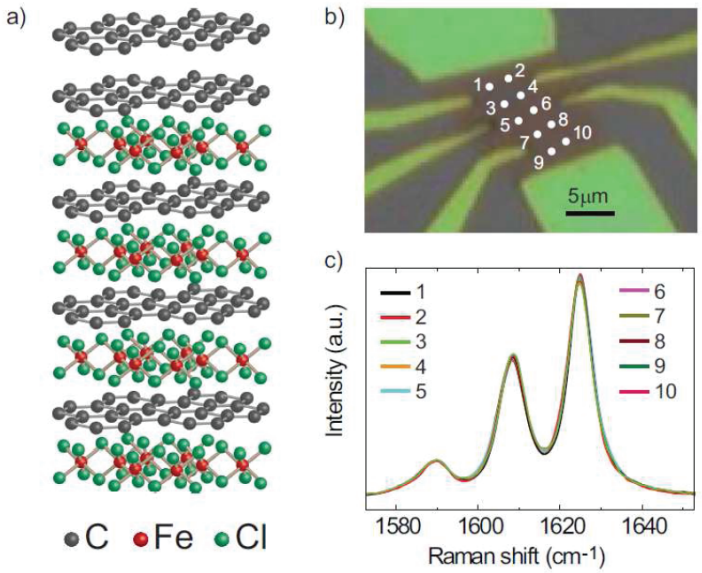

Figure 8.5: a) Schematic crystal structure of a 5L $FeCl_3$-FLG after device fabrication. b) Optical image of 5L $FeCl_3$-FLG. c) Raman spectra of 5L $FeCl_3$-FLG devices taken at different locations as indicated in b).

A remarkable property of $FeCl_3$-FLGs shown by the electrical transport characterization is that intercalated materials thicker than 3L invariably exhibit a very low-sheet resistance, which is essential for their use as electrical conductors. We find a room temperature value of $R_s = 8.8\Omega/\square$ in 5L intercalated FLGs. The 4L intercalated FLGs typically exhibit higher sheet resistance values than the 5L intercalated samples with a similar crystal structure. Furthermore, the sheet resistance of $FeCl_3$-FLGs thicker than 2L decreases when lowering the temperature as expected for metallic conduction (see Figure 8.6(a)). Contrary to intercalated samples, pristine FLGs always have a higher R_s (>120 $\Omega/\square$) and they exhibit non-metallic behaviour as a function of temperature [4, 113, 114] (see Figure 2b). This suggests that the low values of R_s and the metallic nature of the conduction are consequences of intercalation with $FeCl_3$. $FeCl_3$-FLGs thinner than 3L suffer of partial de-intercalation during the device fabrication, which results in a non-metallic behaviour similar to pristine FLGs and in higher R_s values (see Figure 8.6(a)).

The low values of R_s characterizing thick $FeCl_3$-FLG are accompanied by an extremely high charge density. Indeed, the Hall coefficient measurements reveal that n_H ranges from $3\times10^{14}cm^{-2}$ to $8.9\times10^{14}cm^{-2}$, depending on the number of layers (see

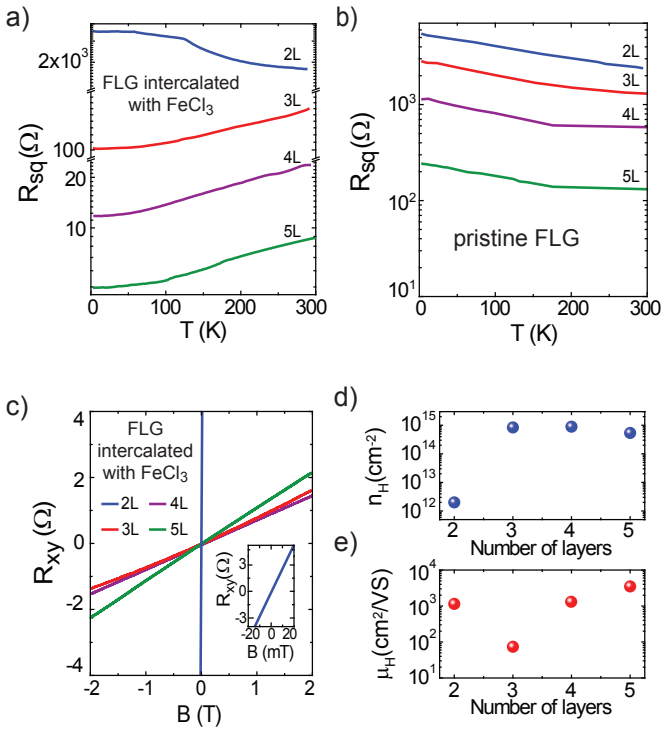

Figure 8.6: a) Temperature dependence of the square resistance for $FeCl_3$-FLG of different thicknesses. b) Square resistance for pristine FLG of different thicknesses as function of temperature. These devices are fabricated on SiO_2/Si substrates and the highly-doped Si substrate is used as a gate to adjust the Fermi level to the charge neutrality of the system. c) Hall resistance of $FeCl_3$-FLG as a function of magnetic field. The inset shows the data for the bilayer sample on a smaller B scale. Panels d) and e) show the carrier density and mobility for $FeCl_3$-FLG as a function of the number of graphene layers.

Figures 8.6(c) and (d)). These charge densities exceed even the highest values demonstrated so far by liquid electrolyte [115] or ionic [116] gating. The corresponding charge

carrier mobility for the 4L and 5L samples typically ranges from $\mu_H = 1540 cm^2/Vs$ to $\mu_H = 3650 cm^2/Vs$ ($\mu_H = 1/(n_H e \rho_{xx})$ with ρ_{xx} the longitudinal resistivity and e the electron charge). Consequently, the charge carriers in thick $FeCl_3$-FLG have a macroscopic mean free path as high as 0.6 μm in 5L at room temperature. The outstanding electrical properties, e.g. lower R_s than ITO and macroscopic mean free path, found in $FeCl_3$-FLGs thicker than 3L are of fundamental interest for the development of novel electronic applications based on highly conductive materials.

Whether $FeCl_3$-FLGs can replace ITO in optoelectronic applications strongly depends on their optical properties. Surprisingly, our detailed study of the optical transmission in the visible wavelength range shows that while $FeCl_3$ intercalation improves significantly the electrical properties of graphene, it leaves the optical transparency nearly unchanged. Figures 8.7(a) and (b) show a comparison between the transmittance spectra of pristine FLG and $FeCl_3$-FLG. The transmittance values of pristine FLG at the wavelength of 550nm are in agreement with the expected values [8], highlighted in Figure 8.7(a), and with the results reported by other groups [8, 103]. Upon intercalation, the transmittance slightly decreases at low wavelengths, but it is still above 80 %. In order to measure an accurate value of transmittance we fit it with a linear dependence on the number of layers for a statistical ensemble of flakes (Figure 8.7(d)). This results in similar extinction coefficients per layer for pristine FLG ($\approx$ 2.4$\pm$0.1%) and for $FeCl_3$-FLG ($\approx$ 2.6$\pm$0.1%), see Figure 8.7(d). For wavelengths longer than 550nm we observe an increase in the optical transparency of $FeCl_3$-FLG. This is a significant advantage of our material compared to ITO whose transparency decreases for wavelengths longer than 600nm [13]. This property will provide useful applications that require conductive electrodes which are transparent both in visible and near infrared range. For instance, $FeCl_3$-FLG transparent electrodes could be used for solar cells to harvest energy over an extended wavelength range as compared to ITO-based devices, or for electromagnetic shielding in infrared.

The high transparency observed in $FeCl_3$-FLG's complemented by their remarkable electrical properties make these materials valuable candidates for transparent conductors. However, to replace ITO in optoelectronic applications, it is generally agreed that materials must (at least) have the properties of commercially available ITO (R_s=10 $\Omega/\square$ and Tr=85% [104]). Figure 8.8 compares R_s *vs.* Tr of $FeCl_3$-FLG materials with ITO [117], and other promising carbon-based candidates to replace ITO such as carbon-nanotube films [118] and doped graphene materials [103]. It is apparent that R_s and Tr of $FeCl_3$-FLGs outperform the current limits of ITO and of the best values reported so far for doped graphene [103]. Therefore, the outstandingly high electrical conductivity

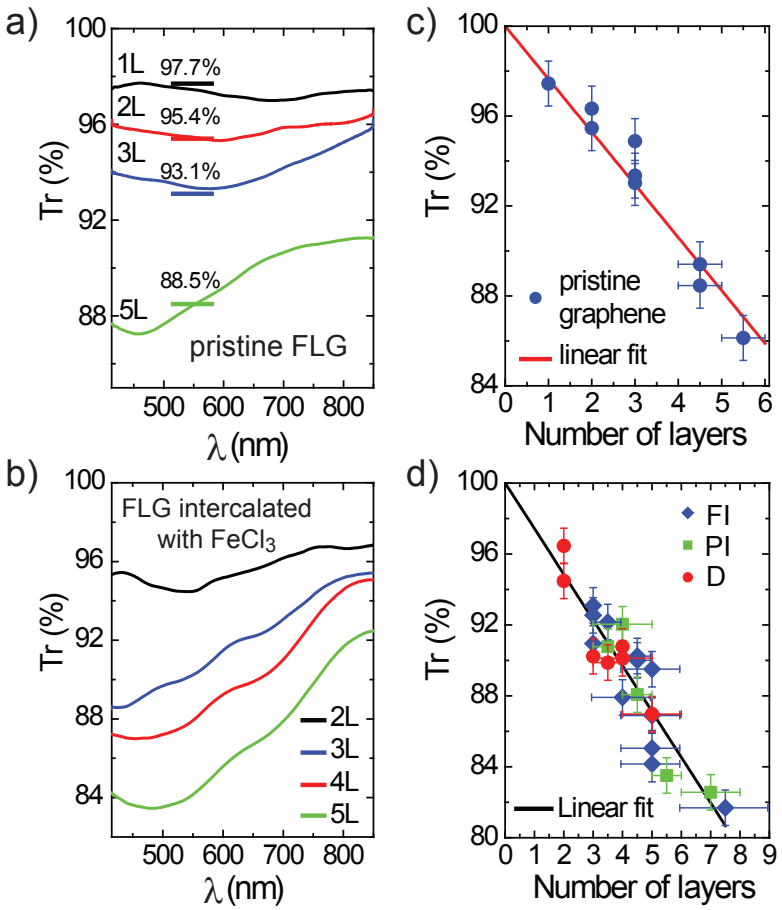

Figure 8.7: Panels a) and b) show the transmittance spectra of pristine FLG and $FeCl_3$-FLG, respectively. The horizontal lines in b) are the corresponding transmittances at the wavelength of $550nm$ reported in the literature [8, 103]. c) Transmittance at $550nm$ for pristine FLG as a function of the number of layers. The red line is a linear fit, which gives the extinction coefficient of $2.35\pm0.1\%$ per layer. d) Transmittance at $550nm$ for fully intercalated $FeCl_3$-FLG (FI), partially intercalated $FeCl_3$-FLG (PI) and doped $FeCl_3$-FLG (D) as a function of the number of layers. The black line is a linear fit with the extinction coefficient of $(2.6\pm0.1)\%$ per layer.

and optical transparency make $FeCl_3$-FLG materials the best transparent conductors

for optoelectronic devices.

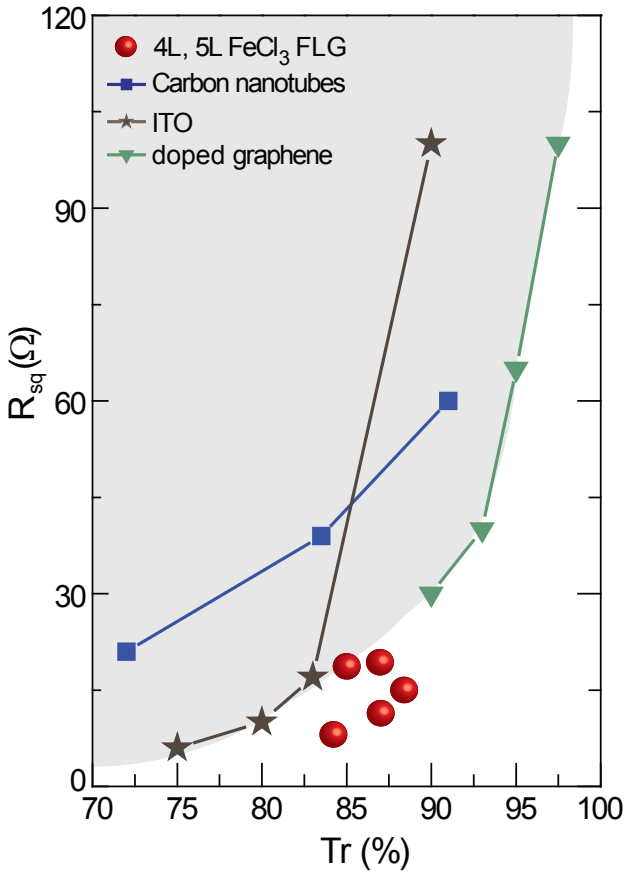

Figure 8.8: Square resistance *versus* transmittance at $550nm$ for 4L and 5L $FeCl_3$-FLG (from these experiments), ITO (from [117]), carbon-nanotube films (from ref [118]) and doped graphene materials (from ref [103]). $FeCl_3$-FLG outperform the current limit of transparent conductors, which is indicated by the grey area. (For the case of ITO and graphene it is the thickness being varied, to give the above dependence)

Finally, an important characteristic required by a transparent conductor is its stability upon exposure to air. In principle FLGs could be intercalated with a large variety of molecules, similar to the graphite intercalation compounds (GIC) [15]. However,

most of the GIC are unstable in air, with donor compounds being easily oxidized and acceptors being easily desorbed. Therefore we studied the stability in air of $FeCl_3$-FLG by performing Raman measurements as a function of time. We found that the Raman spectra of $FeCl_3$-FLG samples show no appreciable changes on a time scale of up to one year, see Figure 8.9. This property has important implications for the utilization of these materials as transparent conductors in practical applications such as displays and photovoltaic devices.

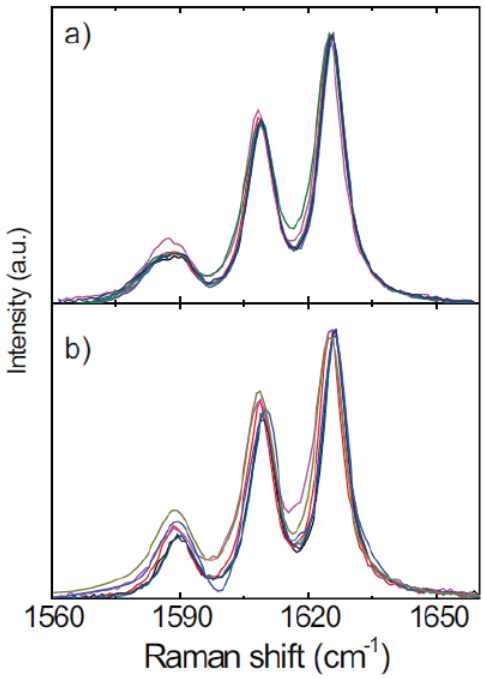

Figure 8.9: a) Schematic crystal structure of a 5L FeCl3-FLG after device fabrication. b) Optical image of 5L FeCl3-FLG. c) Raman spectra of a typical 5L FeCl3-FLG devices taken at different locations after 3 months (a) and after one year (b).

8.4 Conclusion

In conclusion, we demonstrate novel transparent conductors based on few layer graphene intercalated with ferric chloride with an outstandingly high electrical conductivity and optical transparency. We show that upon intercalation a record low sheet resistance of 8.8 $\Omega/\square$ is attained together with an optical transmittance higher than 84% in the visible range. These parameters outperform the best values of ITO and of other carbon-

based materials. The $FeCl_3$-FLGs materials are relatively inexpensive to make and they are easily scalable to industrial production of large area electrodes. Contrary to the numerous chemical species that can be intercalated into graphite (more than hundred [15]), many of which are unstable in air, we found that $FeCl_3$-FLGs are air stable on a timescale of at least one year. Other air stable graphite intercalated compounds can only by synthesized in the presence of Chlorine gas [15], which is highly toxic. On the contrary, here we demonstrate that the intercalation of FLG with $FeCl_3$ is easily achieved without the need of using Chlorine gas, which ensures an environmental friendly industrial processing. Furthermore, the low intercalation temperature (360°C) required in the processing allows the use of a wide range of transparent flexible substrates which are compatible with existing transparent electronic technologies. These technological advantages combined with the unique electro-optical properties found in $FeCl_3$-FLG make these materials a valuable alternative to ITO in optoelectronics.

Chapter 9

Conclusions

Graphene materials are a unique platform for the development of novel transparent and flexible electronics. Indeed, graphene is an ultra lightweight material -just one atom thick- able to conduct electricity and with outstanding mechanical properties such as strength and flexibility. Furthermore, the properties of graphene can be engineered by chemical functionalization to turn this semimetallic material into a semiconductor for example.

In this thesis we explore the chemical functionalization of graphene to engineer the electrical properties of this novel material. More specifically, we aimed at opening an energy gap in the energy dispersion of graphene making it of use for transistor applications, and we aimed at achieving record high electrical conductivity for replacing the expensive ITO transparent conductor in use by display industry.

Fluorinated graphene flakes are exfoliated from bulk fluorinated graphite and in Chapters 4 the electron transport data for partially flourinated graphene is presented it is found that fluorination opens a mobility gap in graphenes band spectrum where, and that at low temperatures ≈ 4 K the I_{on}/I_{off} ratio is greatly enhanced to $\approx 10^3$ but only at low temperatures due to the existance of localized stated which exist within a larger mobility gap. As electron transport is sensitive to localised states we aimed to reduce this density of localised states by increasing the fluorine coverage. However it was seen that we enter a second transport regime known as Efros Sklovskii Variable Range Hopping (ES-VRH), where Coulomb interactions open up a energy gap in the density of states. The samples exhibiting this behavior can be thought of as conductive graphene islands isolated by regions of insulating fluorinated graphene. This observation paved the way to the study of single charging behavior studies in small partially fluorinated graphene flakes shown in Chapter 5.

It is shown that quantum dots can exist within partially fluorinated graphene by selecting small flakes of order (0.5 -1) μ m, and that interestingly a large number of levels (more than 1000) are observed within the transport gap of these devices. The level spacing statistics agree well with the predictions of Random Matrix theory (RMT) discussed in Chapter 2. Only two other papers in history on quantum dots show agreement with RMT [35, 36] and our data constitutes the greatest ensemble of data confirming the application of this theory. This project remains open as reproducibility in several devices is required, a parallel double dot must also be ruled out as a possible reason for the observed bi-modal behaviour.

In an attempt to better open a band gap and reduce the density of localized states in the hope of realizing room temperature transistor action we increased the fluorine coverage. This was achieved using a second method of fluorination which allowed for a higher degree of covalent bonding of the fluorine to the carbon atoms, therefore leading to a better developed band gap. We found that as a result the carrier mobility is greatly reduced falling to ≈ 1 cm^{-2}V^{-1}s^{-1}.

Chapter 6, presents results on the nanopatterning of fluorinated graphene with electron beam irradiation. Electron beam irradiation is found to decrease the resistivity of highly fluorinated by 7 orders of magnitude from (1 TΩ to 100 KΩ) and after mild annealing the resistivity is restored to that similar to graphene. This technique offers the ability to directly write conductive circuitry in insulating fluorinated graphene and semi-conducting components on the nanoscale.

In Chapter 7 it is shown that the the transport properties of heavily fluorinated graphene can be tuned from an insulator to a metal simply by varying the electron beam dose it receives. The electron transport follows that of a lightly doped semiconductor for low doses (0 - 0.1) Ccm^{-2}, while for higher doses (0.1 - 1) Ccm^{-2} the electron transport can be best described by Mott Variable Range Hopping (M-VRH). Finally after a mild annealing treatment the material is transformed into a metallic system with a resistivity similar to that of graphene.

Finally in Chapter 8 the results for the electron transport and optical transparency of intercalated few layer graphene are shown. In an attempt to reduce the resistivity of graphene to make it useful as a transparent conductor we intercalated few-layer graphene with ferric chloride molecules, we found a huge charge transfer with hole concentrations in the graphene flake reaching 8×10^{14} cm^{-2}. We find that the mobility of the few layer graphene is preserved $\approx 3000 cm^2 V^{-1} s^{-1}$, this leads to a record low sheet resistance of $R_{sq} \approx 8\Omega$. Also the optical transparency of few layer graphene was retained post intercalation at around $\approx 85\%$ thus meeting the material requirements

for a replacement for (ITO).

References

[1] Shockley, W. and Pearson, G.L. Modulation of conductance of thin films of semi-conductors by surface charges. *Phys. Rev.*, **74**, 232 (1948). 1

[2] Moore, G.E. Cramming more components onto integrated circuits. *Electronics Magazine.*, page 4 (1965). 1

[3] Keyes, R.W. The impact of moore's law. *Solid-State Circuits Newsletter, IEEE*, **11**, 25 (2006). 1

[4] Novoselov, K.S., Geim, A.K., Morozov, S.V., Jiang, D., Zhang, Y., Dubonos, S.V., Grigorieva, I.V., and Firsov, A.A. Electric field effect in atomically thin carbon films. *Science*, **306**, 666 (2004). 1, 90, 91, 98

[5] Wu, Y., Lin, Y.m., Bol, A.A., Jenkins, K.A., Xia, F., Farmer, D.B., Zhu, Y., and Avouris, P. High-frequency, scaled graphene transistors on diamond-like carbon. *Nature*, **472**, 74 (2011). 2

[6] Lee, C., Wei, X., Kysar, J.W., and Hone, J. Measurement of the elastic properties and intrinsic strength of monolayer graphene. *Science*, **321**, 385 (2008). 3, 90

[7] Chen, C., Rosenblatt, S., Bolotin, K.I., Kalb, W., Kim, P., Kymissis, I., Stormer, H.L., Heinz, T.F., and Hone, J. Performance of monolayer graphene nanomechanical resonators with electrical readout. *Nat Nano*, **4**, 861 (2009). 3

[8] Nair, R.R., Blake, P., Grigorenko, A.N., Novoselov, K.S., Booth, T.J., Stauber, T., Peres, N.M.R., and Geim, A.K. Fine structure constant defines visual transparency of graphene. *Science*, **320**, 1308 (2008). xv, 3, 90, 100, 101

[9] Wang, X., Zhi, L., and Mullen, K. Transparent, conductive graphene electrodes for dye-sensitized solar cells. *Nano Letters*, **8**, 323 (2008). PMID: 18069877. 3

[10] Konstantatos, G., Badioli, Michela andGaudreau, L., Osmond, J., Bernechea, M., de Arquer, F.P.G., Gatti, F., and Koppens, F.H.L. Hybrid graphene-quantum dot phototransistors with ultrahigh gain. *Nat Nano*, **7**, 363 (2012). 3

[11] Wallace, P.R. The band theory of graphite. *Phys. Rev.*, **71**, 622 (1947). 3, 7

[12] Boukhvalov, D.W. and Katsnelson, M.I. Chemical functionalization of graphene with defects. *Nano Letters*, **8**, 4373 (2008). 4, 7, 13

[13] Hecht, D.S., Hu, L., and Irvin, G. Emerging transparent electrodes based on thin films of carbon nanotubes, graphene, and metallic nanostructures. *Advanced Materials*, **23**, 1482 (2011). 4, 100

[14] Khrapach, I., Withers, F., Bointon, T.H., Polyushkin, D.K., Barnes, W.L., Russo, S., and Craciun, M.F. Novel highly conductive and transparent graphene-based conductors. *Advanced Materials*, **24**, 2844 (2012). 4, 6

[15] Dresselhaus, M.S. and Dresselhaus, G. Intercalation compounds of graphite. *Advances in Physics*, **51**, 1 (2002). 4, 6, 93, 94, 97, 102, 104

[16] Withers, F., Dubois, M., and Savchenko, A.K. Electron properties of fluorinated single-layer graphene transistors. *Phys. Rev. B*, **82**, 073403 (2010). 4, 58

[17] Withers, F., Russo, S., Dubois, M., and Craciun, M. Tuning the electronic transport properties of graphene through functionalisation with fluorine. *Nanoscale Research Letters*, **6**, 1 (2011). 58

[18] Withers, F., Bointon, T.H., Dubois, M., Russo, S., and Craciun, M.F. Nanopatterning of fluorinated graphene by electron beam irradiation. *Nano letters*, **11**, 3912 (2011). 4, 80

[19] Elias, D.C., Nair, R.R., Mohiuddin, T.M.G., Morozov, S.V., Blake, P., Halsall, M.P., Ferrari, A.C., Boukhvalov, D.W., Katsnelson, M.I., Geim, A.K., and Novoselov, K.S. Control of graphene's properties by reversible hydrogenation: Evidence for graphane. *Science*, **323**, 610 (2009). 4, 49, 50

[20] Nakajima, T. (editor). *Fluorine-carbon and Fluoride-carbon Materials*. Marcel Dekker inc., New York (1995). 5, 13, 46, 47, 58, 67, 70

[21] Ebert, L.B. Intercalation compounds of graphite. *Ann. Rev. Mat. Sci.*, **6**, 181 (1976). 6, 13

[22] Castro Neto, A.H., Guinea, F., Peres, N.M.R., Novoselov, K.S., and Geim, A.K. The electronic properties of graphene. *Rev. Mod. Phys.*, **81**, 109 (2009). vii, 7, 10

[23] Leenaerts, O., Peelaers, H., Hernández-Nieves, a., Partoens, B., and Peeters, F. First-principles investigation of graphene fluoride and graphane. *Physical Review B*, **82**, 1 (2010). vii, 7, 13, 14, 87

[24] Sofo, J.O., Chaudhari, A.S., and Barber, G.D. Graphane: A two-dimensional hydrocarbon. *Phys. Rev. B*, **75**, 153401 (2007). 7

[25] Gonzlez, J., Guinea, F., and Vozmediano, M. The electronic spectrum of fullerenes from the dirac equation. *Nuclear Physics B*, **406**, 771 (1993). 7

[26] Geim, A.K. and Novoselov, K.S. The rise of graphene. *Nat Mater*, **6**, 1476 (2007). 11, 45

[27] Nair, R.R., Ren, W., Jalil, R., Riaz, I., Kravets, V.G., Britnell, L., Blake, P., Schedin, F., Mayorov, A.S., Yuan, S., Katsnelson, M.I., Cheng, H.M., Strupinski, W., Bulusheva, L.G., Okotrub, A.V., Grigorieva, I.V., Grigorenko, A.N., Novoselov, K.S., and Geim, A.K. Fluorographene: A two-dimensional counterpart of teflon. *Small*, **6**, 2877 (2010). 14, 48, 83

[28] Shklovskii, B.I. and Efros, A.L. (editors). *Electronic Properties of Doped Semiconductors ACS*. Springer Series in Solid State Sciences, Vol. 45, Berlin (1984). viii, 15, 17, 18, 19, 20, 22, 48, 64, 76, 78, 80, 83

[29] Mott, N.F. The transition to the metallic state. *Philosophical Magazine*, **6**, 287 (1961). 17

[30] Hanson, R., Kouwenhoven, L.P., Petta, J.R., Tarucha, S., and Vandersypen, L.M.K. Spins in few-electron quantum dots. *Rev. Mod. Phys.*, **79**, 1217 (2007). viii, 22, 24, 25, 60

[31] Alhassid, Y. The statistical theory of quantum dots. *Rev. Mod. Phys.*, **72**, 895 (2000). viii, 22, 26, 27, 28, 56, 57, 58, 60, 62, 64

[32] Trauzettel, B., Bulaev, D.V., Loss, D., and Burkard, G. Spin qubits in graphene quantum dots. *Nat Phys*, **3**, 192 (2007). 22

[33] Beenakker, C.W.J. Theory of coulomb-blockade oscillations in the conductance of a quantum dot. *Phys. Rev. B*, **44**, 1646 (1991). 26, 59

[34] Bohigas, O., Giannoni, M.J., and Schmit, C. Characterization of chaotic quantum spectra and universality of level fluctuation laws. *Phys. Rev. Lett.*, **52**, 1 (1984). 27

[35] Zdrojek, M., Esplandiu, M.J., Barreiro, A., and Bachtold, A. Electron counting spectroscopy of cdse quantum dots. *Phys. Rev. Lett.*, **102**, 226804 (2009). 29, 63, 106

[36] Lüscher, S., Heinzel, T., Ensslin, K., Wegscheider, W., and Bichler, M. Signatures of spin pairing in chaotic quantum dots. *Phys. Rev. Lett.*, **86**, 2118 (2001). 29, 62, 63, 64, 106

[37] Blanter, Y.M., Mirlin, A.D., and Muzykantskii, B.A. Fluctuations of conductance peak spacings in the coulomb blockade regime: Role of electron-electron interaction. *Phys. Rev. Lett.*, **78**, 2449 (1997). 29, 62, 64

[38] Zhang, Y., Tan, Y.W., Stormer, H.L., and Kim, P. Experimental observation of the quantum hall effect and berry's phase in graphene. *Nature*, **438**, 201 (2005). viii, 31, 34, 94

[39] Ando, T., Fowler, A.B., and Stern, F. Electronic properties of two-dimensional systems. *Rev. Mod. Phys.*, **54**, 437 (1982). 34

[40] Mak, K.F., Sfeir, M.Y., Wu, Y., Lui, C.H., Misewich, J.A., and Heinz, T.F. Measurement of the optical conductivity of graphene. *Phys. Rev. Lett.*, **101**, 196405 (2008). viii, 36, 37

[41] Crowther, A.C., Ghassaei, A., Jung, N., and Brus, L.E. Strong charge-transfer doping of 1 to 10 layer graphene by no2. *ACS Nano*, **6**, 1865 (2012). 36

[42] Blake, P., Hill, E.W., Neto, A.H.C., Novoselov, K.S., Jiang, D., Yang, R., Booth, T.J., and Geim, A.K. Making graphene visible. *Applied Physics Letters*, **91**, 063124 (2007). 36

[43] Malard, L., Pimenta, M., Dresselhaus, G., and Dresselhaus, M. Raman spectroscopy in graphene. *Physics Reports*, **473**, 51 (2009). ix, 38, 39, 93

[44] Koh, Y.K., Bae, M.H., Cahill, D.G., and Pop, E. Reliably counting atomic planes of few-layer graphene (n > 4). *ACS Nano*, **5**, 269 (2011). ix, 40, 91, 93

[45] Cancado, L.G., Jorio, A., Ferreira, E.H.M., Stavale, F., Achete, C.A., Capaz, R.B., Moutinho, M.V.O., Lombardo, A., Kulmala, T.S., and Ferrari, A.C. Quantifying defects in graphene via raman spectroscopy at different excitation energies. *Nano Letters*, **11**, 3190 (2011). ix, 41, 42, 50, 54

[46] Das, A., Pisana, S., Chakraborty, B., Piscanec, S., Saha, S.K., Waghmare, U.V., Novoselov, K.S., Krishnamurthy, H.R., Geim, A.K., Ferrari, A.C., and Sood, A.K. Monitoring dopants by raman scattering in an electrochemically top-gated graphene transistor. *Nat Nano*, **3**, 210 (2008). ix, 42, 43

[47] Howard, C.A., Dean, M.P.M., and Withers, F. Phonons in potassium-doped graphene: The effects of electron-phonon interactions, dimensionality, and adatom ordering. *Phys. Rev. B*, **84**, 241404 (2011). 42, 93

[48] Touhara, H. and Okino, F. Property control of carbon materials by fluorination. *Carbon*, **38**, 241 (2000). 46

[49] Zhang, W., Spinelle, L., Dubois, M., Gurin, K., Kharbache, H., Masin, F., Kharitonov, A., Hamwi, A., Brunet, J., Varenne, C., Pauly, A., Thomas, P., Himmel, D., and Mansot, J. New synthesis methods for fluorinated carbon nanofibres and applications. *Journal of Fluorine Chemistry*, **131**, 676 (2010). 46

[50] Sato, Y., Itoh, K., Hagiwara, R., Fukunaga, T., and Ito, Y. On the so-called semi-ionic cf bond character in fluorinegic. *Carbon*, **42**, 3243 (2004). 46

[51] Zhang, W., Gurin, K., Dubois, M., Fawal, Z.E., Ivanov, D.A., Vidal, L., and Hamwi, A. Carbon nanofibres fluorinated using tbf4 as fluorinating agent. part i: Structural properties. *Carbon*, **46**, 1010 (2008). 46

[52] Giraudet, J., Dubois, M., Gurin, K., Delabarre, C., Hamwi, A., and Masin, F. Solid-state nmr study of the post-fluorination of (c2.5f)n fluorinegic. *The Journal of Physical Chemistry B*, **111**, 14143 (2007). PMID: 18052273. 46

[53] Ferrari, A.C., Meyer, J.C., Scardaci, V., Casiraghi, C., Lazzeri, M., Mauri, F., Piscanec, S., Jiang, D., Novoselov, K.S., Roth, S., and Geim, A.K. Raman spectrum of graphene and graphene layers. *Phys. Rev. Lett.*, **97**, 187401 (2006). 47, 50, 93

[54] Ferrari, A.C. Raman spectroscopy of graphene and graphite: Disorder, electronphonon coupling, doping and nonadiabatic effects. *Solid State Communications*, **143**, 47 (2007).

[55] Ferrari, A.C. and Robertson, J. Interpretation of raman spectra of disordered and amorphous carbon. *Phys. Rev. B*, **61**, 14095 (2000). 47

[56] Casiraghi, C., Hartschuh, A., Qian, H., Piscanec, S., Georgi, C., Fasoli, A., Novoselov, K.S., Basko, D.M., and Ferrari, A.C. Raman spectroscopy of graphene edges. *Nano Letters*, **9**, 1433 (2009). PMID: 19290608. 47

[57] Cheng, S.H., Zou, K., Okino, F., Gutierrez, H.R., Gupta, A., Shen, N., Eklund, P.C., Sofo, J.O., and Zhu, J. Reversible fluorination of graphene: Evidence of a two-dimensional wide bandgap semiconductor. *Phys. Rev. B*, **81**, 205435 (2010). 48, 56, 64, 69, 87

[58] Kechedzhi, K., Horsell, D.W., Tikhonenko, F.V., Savchenko, A.K., Gorbachev, R.V., Lerner, I.V., and Fal'ko, V.I. Quantum transport thermometry for electrons in graphene. *Phys. Rev. Lett.*, **102**, 066801 (2009). 50

[59] Gorbachev, R.V., Mayorov, A.S., Savchenko, A.K., Horsell, D.W., and Guinea, F. Conductance of p-n-p graphene structures with air-bridge top gates. *Nano Letters*, **8**, 1995 (2008). PMID: 18543979. 56

[60] Withers, F., Dubois, M., and Savchenko, A.K. Electron properties of fluorinated single-layer graphene transistors. *Phys. Rev. B*, **82**, 073403 (2010). 56, 64

[61] Withers, F., Russo, S., Dubois, M., and Craciun, M. Tuning the electronic transport properties of graphene through functionalisation with fluorine. *Nanoscale Research Letters*, **6**, 526 (2011).

[62] Nair, R.R., Ren, W., Jalil, R., Riaz, I., Kravets, V.G., Britnell, L., Blake, P., Schedin, F., Mayorov, A.S., Yuan, S., Katsnelson, M.I., Cheng, H.M., Strupinski, W., Bulusheva, L.G., Okotrub, A.V., Grigorieva, I.V., Grigorenko, A.N., Novoselov, K.S., and Geim, A.K. Fluorographene: A two-dimensional counterpart of teflon. *Small*, **6**, 2877 (2010).

[63] Robinson, J.T., Burgess, J.S., Junkermeier, C.E., Badescu, S.C., Reinecke, T.L., Perkins, F.K., Zalalutdniov, M.K., Baldwin, J.W., Culbertson, J.C., Sheehan, P.E., and Snow, E.S. Properties of fluorinated graphene films. *Nano Letters*, **10**, 3001 (2010). 56, 87

[64] Ponomarenko, L.A., Schedin, F., Katsnelson, M.I., Yang, R., Hill, E.W., Novoselov, K.S., and Geim, A.K. Chaotic dirac billiard in graphene quantum dots. *Science*, **320**, 356 (2008). 56, 58, 59

[65] Han, M.Y., Özyilmaz, B., Zhang, Y., and Kim, P. Energy band-gap engineering of graphene nanoribbons. *Phys. Rev. Lett.*, **98**, 206805 (2007). 58, 72

[66] Stampfer, C., Güttinger, J., Hellmüller, S., Molitor, F., Ensslin, K., and Ihn, T. Energy gaps in etched graphene nanoribbons. *Phys. Rev. Lett.*, **102**, 056403 (2009). 58

[67] Shimizu, T., Haruyama, J., Marcano, D.C., Kosinkin, D.V., Tour, J.M., Hirose, K., and Suenaga, K. Large intrinsic energy bandgaps in annealed nanotube-derived graphene nanoribbons. *Nat Nano*, **6**, 45 (2005).

[68] Li, X., Wang, X., Zhang, L., Lee, S., and Dai, H. Chemically derived, ultrasmooth graphene nanoribbon semiconductors. *Science*, **319**, 1229 (2008). 56

[69] Libisch, F., Stampfer, C., and Burgdörfer, J. Graphene quantum dots: Beyond a dirac billiard. *Phys. Rev. B*, **79**, 115423 (2009). 56, 62

[70] Huang, L., Lai, Y.C., and Grebogi, C. Characteristics of level-spacing statistics in chaotic graphene billiards. *Chaos*, **21**, 013102 (2011). 56, 62

[71] Guttinger, J., Stampfer, C., Frey, T., Ihn, T., and Ensslin, K. Transport through a strongly coupled graphene quantum dot in perpendicular magnetic field. *Nanoscale Research Letters*, **6**, 253 (2011). 59, 64

[72] Berkovits, R. and Altshuler, B.L. Compressibility, capacitance, and ground-state energy fluctuations in a weakly interacting quantum dot. *Phys. Rev. B*, **55**, 5297 (1997). 62, 64

[73] Walker, P.N., Gefen, Y., and Montambaux, G. Density modulations and addition spectra of interacting electrons in disordered quantum dots. *Phys. Rev. Lett.*, **82**, 5329 (1999).

[74] Ahn, K.H., Richter, K., and Lee, I.H. Addition spectra of chaotic quantum dots: Interplay between interactions and geometry. *Phys. Rev. Lett.*, **83**, 4144 (1999). 64

[75] Rogers, J.A., Someya, T., and Huang, Y. Materials and mechanics for stretchable electronics. *Science*, **327**, 1603 (2010). 66

[76] Nomura, K., Ohta, H., Takagi, A., Kamiya, T., Hirano, M., and Hosono, H. Room-temperature fabrication of transparent flexible thin-film transistors using amorphous oxide semiconductors. *Nature*, **432**, 488 (2004). 66

[77] Forrest, S.R. The path to ubiquitous and low-cost organic electronic appliances on plastic. *Nature*, **428**, 911 (2004). 66

[78] Facchetti, A. Semiconductors for organic transistors. *Materials Today*, **10**, 28 (2007). 66

[79] Klauk, H. Organic thin-film transistors. *Chemical Society Review*, **39**, 2643 (2010). 66

[80] Ahn, B.Y., Duoss, E.B., Motala, M.J., Guo, X., Park, S.I., Xiong, Y., Yoon, J., Nuzzo, R.G., Rogers, J.A., and Lewis, J.A. Omnidirectional printing of flexible, stretchable, and spanning silver microelectrodes. *Science*, **321**, 1590 (2009). 66

[81] Sekitani, T., Noguchi, Y., Hata, K., Fukushima, T., Aida, T., and Someya, T. A rubberlike stretchable active matrix using elastic conductors. *Science*, **321**, 1468 (2008). 66

[82] Zhongqing, W., Debin, W., Suenne, K., Soo-Young, K., Yike, H., Yakes, M.K., Laracuente, A.R., Zhenting, D., Marder, S.R., Claire, B., King, W.P., de Heer, W.A., Sheehan1, P.E., , and Riedo2, E. Nanoscale tunable reduction of graphene oxide for graphene electronics. *Science*, **328**, 1373 (2010). 67

[83] Jones, J., Mahajan, K., Williams, W., Ecton, P., Mo, Y., and Perez, J. Formation of graphane and partially hydrogenated graphene by electron irradiation of adsorbates on graphene. *Carbon*, **48**, 2335 (2010). 67

[84] Motoyama, M., Nakajima, T., and Watanabe, N. Electron beam-induced decomposition of graphite fluoride. *Solid State Ionics*, **13**, 221 (1984). 70

[85] Bart, M., Harland, P.W., Hudson, J.E., and Vallance, C. Absolute total electron impact ionization cross-sections for perfluorinated hydrocarbons and small halocarbons. *Phys. Chem. Chem. Phys.*, **3**, 800 (2001). 70

[86] Goldstein, J., Newbury, D.E., Joy, D.C., Lyman, C.E., Echlin, P., and Lifshin, E. (editors). *Scanning electron microscopy and X-ray microanalysis.* Springer Science, New York (2003). 70

[87] Han, M.Y., Brant, J.C., and Kim, P. Electron transport in disordered graphene nanoribbons. *Phys. Rev. Lett.*, **104**, 056801 (2010). 72

[88] Gallagher, P., Todd, K., and Goldhaber-Gordon, D. Disorder-induced gap behavior in graphene nanoribbons. *Phys. Rev. B*, **81**, 115409 (2010).

[89] Oostinga, J.B., Sacepe, B., Craciun, M.F., and Morpurgo, A.F. Magnetotransport through graphene nanoribbons. *Phys. Rev. B*, **81**, 193408 (2010). 72, 77

[90] Efros, A.L. and Shklovskii, B.I. (editors). *Electron-Electron Interactions in Disordered Systems.* North-Holland, Amsterdam (1985). 76

[91] Tan, Y.-W., Zhang, Y., Stormer, H. L., and Kim, P. Temperature dependent electron transport in graphene. *Eur. Phys. J. Special Topics*, **148**, 15 (2007). 80

[92] Abboudy, S. A quasi-universal percolation approach of hopping activation energy and metal-nonmetal transition in semiconductors. *Physica B: Condensed Matter*, **212**, 175 (1995). 84

[93] Middleton, A.A. and Wingreen, N.S. Collective transport in arrays of small metallic dots. *Phys. Rev. Lett.*, **71**, 3198 (1993). 84

[94] Blunt, M.O., uvakov, M., Pulizzi, F., Martin, C.P., Pauliac-Vaujour, E., Stannard, A., Rushforth, A.W., Tadi, B., and Moriarty, P. Charge transport in cellular nanoparticle networks: meandering through nanoscale mazes. *Nano Letters*, **7**, 855 (2007). PMID: 17335264. 84

[95] Joung, D., Zhai, L., and Khondaker, S.I. Coulomb blockade and hopping conduction in graphene quantum dots array. *Phys. Rev. B*, **83**, 115323 (2011). 84

[96] Shklovskii, A.L.E. and I., B. *Electron-Electron Interactions in Disordered Systems*. North-Holland, Amsterdam (1985). 86

[97] Zhang, Y., Dai, O., Levy, M., and Sarachik, M.P. Probind the coulomb gap in insulating n-type cdse. *Phys. Rev. Lett.*, **64**, 2687 (1990). 86

[98] Abanin, D.A., Shytov, A.V., and Levitov, L.S. Peierls-Type Instability and Tunable Band Gap in Functionalized Graphene. *Physical Review Letters*, **105**, 86802 (2010). 86

[99] Kumar, A. and Zhou, C. The race to replace tin-doped indium oxide: Which material will win? *ACS Nano*, **4**, 11 (2010). PMID: 20099909. 90

[100] Hecht, D.S., Hu, L., and Irvin, G. Emerging transparent electrodes based on thin films of carbon nanotubes, graphene, and metallic nanostructures. *Advanced Materials*, **23**, 1482 (2011).

[101] Wassei, J.K. and Kaner, R.B. Graphene, a promising transparent conductor. *Materials Today*, **13**, 52 (2010). 90

[102] Novoselov, K.S., Geim, A.K., Morozov, S.V., Jiang, D., Katsnelson, M.I., Grigorieva, I.V., Dubonos, S.V., and Firsov, A.A. Two-dimensional gas of massless dirac fermions in graphene. *Nature*, **438**, 197 (2005). 90, 94

[103] Bae, S., Kim, H., Lee, Y., Xu, Xiangfan andPark, J.S., Zheng, Y., Balakrishnan, J., Lei, T., Ri Kim, H., Song, Y.I., Kim, Y.J., Kim, K.S., Ozyilmaz, B., Ahn, J.H., Hong, B.H., and Iijima, S. Roll-to-roll production of 30-inch graphene films for transparent electrode. *Nat Nano*, **5**, 574 (2010). xv, 90, 91, 100, 101, 102

[104] De, S. and Coleman, J.N. Are there fundamental limitations on the sheet resistance and transmittance of thin graphene films? *ACS Nano*, **4**, 2713 (2010). PMID: 20384321. 90, 100

[105] Wang, Y., Tong, S.W., Xu, X.F., zyilmaz, B., and Loh, K.P. Interface engineering of layer-by-layer stacked graphene anodes for high-performance organic solar cells. *Advanced Materials*, **23**, 1514 (2011). 91

[106] Kim, K.K., Reina, A., Shi, Y., Park, H., Li, L.J., Lee, Y.H., and Kong, J. Enhancing the conductivity of transparent graphene films via doping. *Nanotechnology*, **21**, 285205 (2010). 91

[107] Kasry, A., Kuroda, M.A., Martyna, G.J., Tulevski, G.S., and Bol, A.A. Chemical doping of large-area stacked graphene films for use as transparent, conducting electrodes. *ACS Nano*, **4**, 3839 (2010). 91

[108] Zhao, W., Tan, P.H., Liu, J., and Ferrari, A.C. Intercalation of few-layer graphite flakes with fecl3: Raman determination of fermi level, layer by layer decoupling, and stability. *Journal of the American Chemical Society*, **133**, 5941 (2011). 91, 93

[109] Zhan, D., Sun, L., Ni, Z.H., Liu, L., Fan, X.F., Wang, Y., Yu, T., Lam, Y.M., Huang, W., and Shen, Z.X. Fecl3-based few-layer graphene intercalation compounds: Single linear dispersion electronic band structure and strong charge transfer doping. *Advanced Functional Materials*, **20**, 3504 (2010). 91, 93

[110] Kim, N., Kim, K.S., Jung, N., Brus, L., and Kim, P. Synthesis and electrical characterization of magnetic bilayer graphene intercalate. *Nano Letters*, **11**, 860 (2011). 93, 96

[111] Jung, N., Kim, B., Crowther, A.C., Kim, N., Nuckolls, C., and Brus, L. Optical reflectivity and raman scattering in few-layer-thick graphene highly doped by k and rb. *ACS Nano*, **5**, 5708 (2011). 93

[112] Davies, J.H. (editor). *The Physics of Low-Dimensional Semiconductors*. Cambridge University Press, Cambridge (1998). 94

[113] Craciun, M.F., Russo, S., Yamamoto, M., Oostinga, J.B., Morpurgo, A.F., and Tarucha, S. Trilayer graphene is a semimetal with a gate-tunable band overlap. *Nat Nano*, **4**, 383 (2005). 98

[114] Zhu, W., Perebeinos, V., Freitag, M., and Avouris, P. Carrier scattering, mobilities, and electrostatic potential in monolayer, bilayer, and trilayer graphene. *Phys. Rev. B*, **80**, 235402 (2009). 98

[115] Efetov, D.K. and Kim, P. Controlling electron-phonon interactions in graphene at ultrahigh carrier densities. *Phys. Rev. Lett.*, **105**, 256805 (2010). 99

[116] Ye, J., Craciun, M.F., Koshino, M., Russo, S., Inoue, S., Shimotan, Y.H., Morpurgo, A.F., and Iwasa, Y. Accessing the transport properties of graphene and its multilayers at high carrier density. *PNAS*, **108**, 13002 (2011). 99

[117] Lee, J.Y., Connor, S.T., Cui, Y., and Peumans, P. Solution-processed metal nanowire mesh transparent electrodes. *Nano Letters*, **8**, 689 (2008). PMID: 18189445. xv, 100, 102

[118] Hecht, D.S., Heintz, A.M., Lee, R., Hu, L., Moore, B., Cucksey, C., and Risser, S. High conductivity transparent carbon nanotube films deposited from superacid. *Nanotechnology*, **22**, 075201 (2011). xv, 100, 102

Appendix

Graphene and fluorinated graphene device preparation

Below summarises the basic steps for successful graphene and flourinated graphene FET device fabrication from mechanical exfoliation from high quality natural crystals (Source : Graphenium).

- Sonicate in pre cleaned beakers oxidized (275 nm) Si^{++} wafers (which have had metalized markers pre patterned, required for 80 keV electron beam system) in Acetone for 30 min.
- Transfer without breaking surface meniscus to fresh Acetone and boil substrates for further 15 min.
- Sonicate for further 5 min.
- Transfer to Isoproponol and sonicate for further 20 min.
- Remove substrates and nitrogen dry then place on the hot plate at 120 degrees.
- Plasma etch at low power and low gas pressure for short time period in Oxygen.
- Place back on hot plate at 120 degrees and leave for ten minutes.
- While substrates are on the hot plate, prepare the exfoliated graphite. To do this select a high quality natural crystal and use blue semiconductor tape to firstly remove dirty exterior graphite leaving a large highly metallic looking flake of graphite.
- Transfer this graphite to new tape and exfoliate 8 - 12 times, then removing the large graphite crystal for future use.

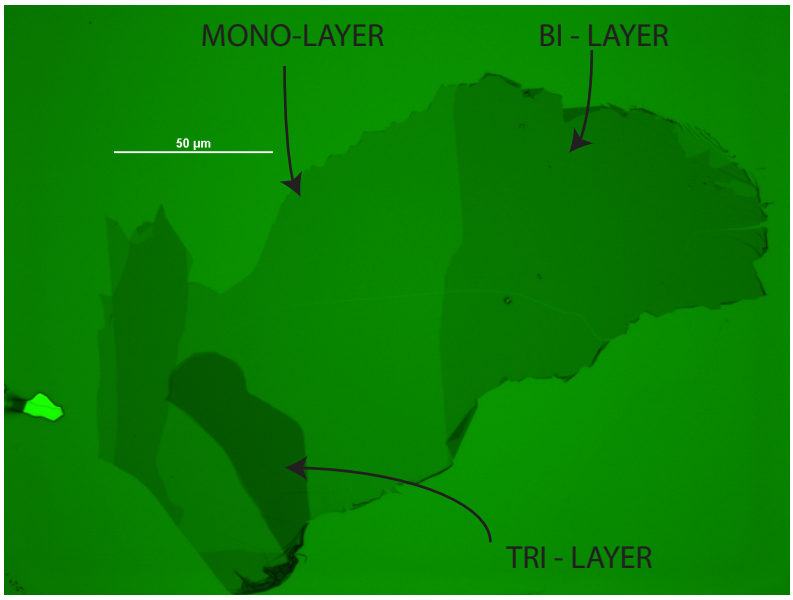

Figure 1: Shows a typical exfoliated graphene flake of size $\approx$ 400 μm^2 consisting of mono-layer, bi-layer and tri-layer material. Image taken with green light filter to maximize contrast see Chapter 3

- Lay the tape (Nitto tape (SWT-20)) close to the hot plate and directly place the oxide face of the substrates onto the freshly exfoliated graphite.
- Press firmly the tape with fingers for 30 sec.
- Very slowly remove the tape from the substrate.. . .

For every 1 cm square substrate exfoliated onto, flakes of size shown in Figure 1 can be achieved.

- After exfoliation spin a single layer of A6 495 K Polymethylmethacrylate (electron beam resist) and bake at 170 degrees for 15 min.
- Once the flakes have been identified AutoCaD or equivalent software can be used to produce pattern data for the project.
- After electron beam lithography develop for 30 sec in MIBK developer then wash in IPA for 1 min, Nitrogen dry then evaporate 5 nm Cr / 70 nm Au.

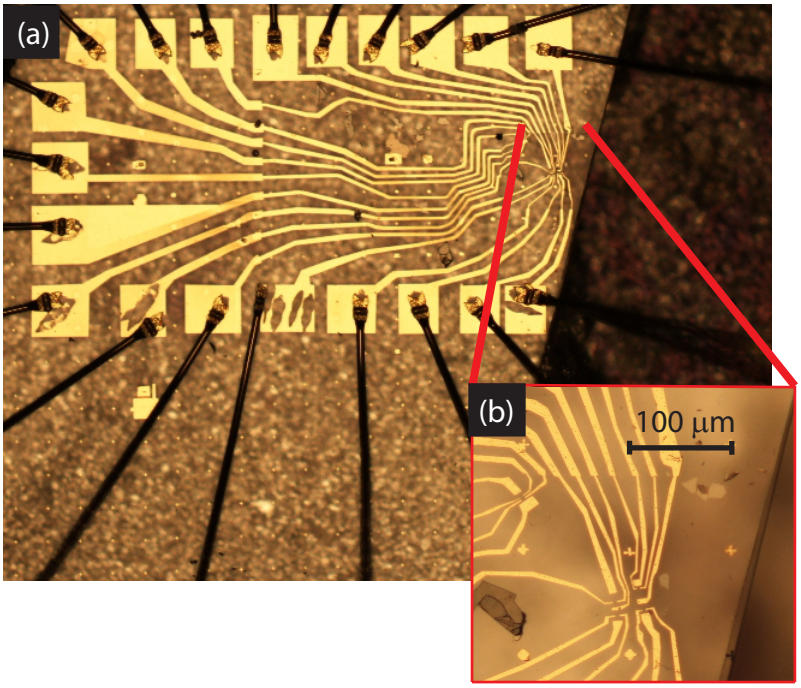

Figure 2: (a) Typical graphene device on a silica cover slip showing all electrical connections and bonding pads with Au wire bonded to the pads. (b) Zoom in of the graphene flakes showing electrical connections to the individual graphene flakes.

- Finally lift off in warm acetone, wash in IPA and nitrogen, then place into the chip carrier and Au wire bond to the contact pads...

Figure 2 shows a typical device after fabrication, this particular device was fabricated on silica cover slips and features flakes intercalated with ferric chloride. The results from this device star in Chapter 8.